

**Evaluating Small  
Molecule and Macromolecular Ligands for Tuning  
Protease Activity on QD Probes**

By  
Yow Ting Jeen

A thesis submitted in partial fulfillment of the  
requirements of the degree of  
Master of Science

The Faculty of Graduate and Postdoctoral Studies  
(Chemistry)

The University of British Columbia  
(Vancouver)

August 2018

© Yow Ting Jeen 2018

The following individuals certify that they have read, and recommend to the Faculty of Graduate and Postdoctoral Studies for acceptance, a thesis/dissertation entitled:

Evaluating Small Molecule and Macromolecular Ligands for Tuning Protease Activity on QD Probes

submitted by Yow Ting Jeen in partial fulfillment of the requirements for

the degree of Master of Science

in Chemistry

**Examining Committee:**

W. Russ Algar, Chemistry  
Supervisor

Jason Hein, Chemistry  
Supervisory Committee Member

Suzana Straus, Chemistry  
Supervisory Committee Member

Keith Mitchell, Chemistry  
Additional Examiner

## Abstract

Quantum dots (QDs) provide a promising platform for fluorescence-based assays. Their non-trivial surface area, bright photoluminescence (PL), and photostability can be coupled to Förster resonance energy transfer (FRET) to enable sensitive detection of proteolytic activities. To further develop QD probes and fine-tune the interactions between QDs and enzymes, the QD ligand library was expanded to include a zwitterionic carboxybetaine, anionic serine-appended lipoic acid, and a glucitol-functionalized lipoic acid. Ligands are a necessary part of QD probes as QDs are often synthesized with hydrophobic ligands and ligand exchange is needed to render QDs colloidally stable in aqueous solutions. Since the ligands are at the interface of the nanocrystal surface and the bulk solution, a variety of available QD surface chemistry is needed to optimize ligand selection for different analytes and matrices. The pH and ionic stability of the new ligand-coated QDs were evaluated and compared to the commonly used dihydrolipoic acid (DHLA) and glutathione-coated QDs. Three model proteases were studied to evaluate their activities on the different ligand-coated QDs. The variations in the proteolytic activities on the different QDs could be used to distinguish between the three enzymes. As the ligand library continues to expand, a combination of these QDs can be used to identify an unknown enzyme in a microarray format.

Biomolecules conjugated to QDs provide yet another strategy to manipulate proteolytic activity on QDs. As a proof-of concept, a peptide sequence based on protease-activated-receptor 1 (PAR1) was displayed on QD-substrate conjugate to mimic the display of PAR1 on cellular surface. The PAR1-displaying zwitterionic QDs were associated with enhanced relative initial rate compared to the control by as much as 15-fold. These results highlight the importance of the QD surface chemistry and that different elements can have a synergistic effect when assembled together on the QD platform. Similar to what is seen in biology, the selectivity of QD probes can be tuned through additional allosteric interactions instead of substrate recognition sites for the protease active site alone.

## **Lay Summary**

The surface chemistry of quantum dots (QDs) is of great importance as it is at the interface of the nanocrystal and the bulk solution. Different ligand coatings were developed and the various ligand-coated QDs were evaluated in terms of their stability at different pH and ionic strength conditions. Fluorescence spectroscopy was used to monitor the activity of three different proteases on the surface of the quantum dots. It was found that protease activity on the different ligand-coated, substrate-conjugated QDs showed a wide range of proteolytic activity. Nonetheless, the “fingerprint” generated by the QDs was specific to each enzyme and could be used to develop a system for enzyme identification. In addition, QDs demonstrated that the inorganic platform can be used to mimic cellular surface with the display of macromolecules and zwitterionic ligands. The results discussed herein can be used in the future as strategies to tune the interactions between QDs and other molecules in the bulk solution.

## **Preface**

This thesis is based on currently unpublished work. Tiffany Jeen co-designed and completed the experiments and analyzed the data. Dr. Algar co-designed the research and helped edit the thesis.

# Table of Contents

Abstract.....	iii
Lay Summary.....	iv
Preface.....	v
Table of Contents.....	vi
List of Tables.....	ix
List of Figures.....	x
List of Schemes.....	xii
List of Abbreviations.....	xiii
Acknowledgements.....	xv
<b>Chapter 1 : Introduction.....</b>	<b>1</b>
1.1    Quantum Dots.....	1
1.1.1    Optical Properties.....	1
1.1.2    Structure and Composition.....	3
1.1.3    QD Surface Coatings.....	4
1.1.4    QD Bioconjugation.....	7
1.2    Fluorescence.....	11
1.2.1    Fluorescence Quenching.....	13
1.2.2    Excited-state Lifetimes.....	14
1.2.3    Fluorescence Intensity and Quantum Yield.....	15
1.2.4    Förster Resonance Energy Transfer.....	16
1.3    Biosensors and Enzyme Assays.....	18
1.3.1    Proteolysis.....	19
1.3.2    Michaelis-Menten and Briggs-Haldane Kinetics.....	20
<b>Chapter 2 : Synthesis &amp; Characterization of Small Molecule Ligands.....</b>	<b>23</b>
2.1    Introduction.....	23
2.2    Experimental Methods.....	23
2.2.1    Materials.....	23
2.2.2    Instruments.....	24
2.2.3    Synthesis of QD Ligands.....	24
2.2.4    Ligand Exchange.....	31
2.2.5    Characterization of QDs.....	32
2.2.6    Enzyme Assays with QD <sub>x</sub> .....	33

2.3	Data Analysis .....	34
2.3.1	Ferguson Analysis.....	34
2.3.2	Quantum Yield Measurements of QD <sub>x</sub> .....	35
2.3.3	Spectral Overlap and Förster Distance of QD604-A680 Pair.....	35
2.4	Results and Discussion.....	36
2.4.1	Design and Synthesis of QD Ligands .....	36
2.4.2	Ligand Exchange .....	37
2.4.3	Characterizations of QD <sub>x</sub> .....	38
2.5	Enzyme Assays with QD <sub>x</sub> .....	43
2.5.1	QD-A680 FRET Pair .....	43
2.5.2	Assays with Thrombin, Trypsin, and Papain .....	44
2.5.3	Average Rate of Enzyme Digestion on QD <sub>x</sub> .....	46
2.5.4	Relative Rate of Enzyme Digestion on QD <sub>x</sub> .....	48
2.6	Conclusion.....	49
<b>Chapter 3 : Evaluating the Effects of Small Molecule Ligands and Macromolecules on Proteolytic Activity .....</b>		<b>50</b>
3.1	Introduction .....	50
3.2	Experimental Methods .....	52
3.2.1	Materials .....	52
3.2.2	Peptide Labeling.....	54
3.2.3	Peptide Quantification and Self-Assembly.....	55
3.2.4	Characterization of QDs .....	55
3.2.5	Spectral Overlap and Förster Distance of QD604-A647 Pair.....	56
3.2.6	Proteolytic Assays.....	56
3.3	Data analysis .....	57
3.3.1	Proteolytic Assays.....	57
3.4	Results and Discussion.....	58
3.4.1	QD604–A647 FRET Pair.....	59
3.4.2	Maximum Substrate Loading on QD604 .....	60
3.4.3	Proteolytic Assays with Thrombin.....	61
3.4.4	HisPAR Enhancement vs. Thrombin Concentration .....	63
3.4.5	HisPAR Enhancement on Different Nanocrystals .....	65
3.4.6	Protease Adsorption on QDs.....	66
3.5	Conclusion.....	70
<b>Chapter 4 : Conclusions and Future Work .....</b>		<b>71</b>

4.1	Thesis Overview.....	71
4.2	Future Outlook .....	72
<b>References .....</b>		<b>74</b>
<b>Appendix.....</b>		<b>A-1</b>
1.	NMR Spectra .....	A-1
2.	ESI-MS Spectra .....	A-22
3.	Stability Tests (pH and Ionic Strength).....	A-24
4.	Enzyme Assay Progress Curves .....	A-31

## List of Tables

Table 2.1. Peptide sequence.....	24
Table 2.2. List of ligands and their abbreviations.....	31
Table 2.3. List of enzymes and concentrations.....	34
Table 2.4. The hydrodynamic diameters, zeta potential, and quantum yield of QD <sub>X</sub> .....	39
Table 2.5. Förster distances between QD <sub>X</sub> and A680.....	43
Table 3.1. Peptide sequences.....	53
Table 3.2. Förster distances between QD <sub>X</sub> and A647.....	59

## List of Figures

Figure 1.1. Properties of QDs .....	2
Figure 1.2. Different strategies to render QDs colloiddally stable .....	5
Figure 1.3. Different covalent conjugation chemistries.....	9
Figure 1.4. Various coordination chemistries to form QD bioconjugates.....	10
Figure 1.5. Jablonski diagrams depicting competing radiative and non-radiative pathways. ....	12
Figure 1.6. Changes in the relative concentrations in a single-substrate system.....	20
Figure 2.1. Structures of ligands used in this chapter.....	37
Figure 2.2. TEM image of CdSe/CdS/ZnS QD604. ....	39
Figure 2.3. Representative images of gel electrophoresis and Ferguson plots of QD <sub>X</sub> , .....	40
Figure 2.4. pH stability tests of QD <sub>X</sub> .....	42
Figure 2.5. Normalized absorption and PL emission spectra of QD604 and A680.....	44
Figure 2.6. Summary progress curves of QD <sub>X</sub> with thrombin, trypsin and papain .....	45
Figure 2.7. Summary of the proteolytic rates on QD <sub>X</sub> for thrombin, trypsin, and papain.....	47
Figure 2.8. Relative proteolytic rates of QD <sub>X</sub> compared to QD <sub>DHLA</sub> .....	48
Figure 3.1. Thrombin anion-binding exosites.....	50
Figure 3.2. Molecular basis of the allosteric communications of PAR1. ....	51
Figure 3.3. Normalized absorption and PL emission spectra of QD604 and A647.....	59
Figure 3.4. Maximum substrate loading of QD604.....	60
Figure 3.5. Progress curves of QD <sub>X</sub> -Sub(A647) <sub>8</sub> -[Y] <sub>N</sub> .....	61
Figure 3.6. Summary of relative initial rates for PAR1 enzyme assays .....	62
Figure 3.7. Progress curves of QD <sub>SB</sub> conjugates with increasing thrombin concentrations .....	64
Figure 3.8. Initial rates of QD <sub>SB</sub> conjugates with increasing thrombin concentrations .....	64
Figure 3.9. Relative initial rates of various QDs with PAR1.....	65
Figure 3.10. Thrombin adsorption on QD <sub>X</sub> and QD <sub>X</sub> -[Y] <sub>40</sub> (GSH & DHLA).....	68
Figure 3.11. Thrombin adsorption on QD <sub>X</sub> and QD <sub>X</sub> -[Y] <sub>40</sub> (SB & CB) .....	69
Figure A1. <sup>1</sup> H NMR spectrum of DHLA.....	A-1
Figure A2. <sup>13</sup> C NMR spectrum of DHLA.....	A-2
Figure A3. <sup>1</sup> H NMR spectrum of LA-NHS. ....	A-3
Figure A4. <sup>13</sup> C NMR spectrum of LA-NHS. ....	A-4

Figure A5. $^1\text{H}$ NMR spectrum of 2.....	A-5
Figure A6. $^{13}\text{C}$ NMR spectrum of 2.....	A-6
Figure A7. $^1\text{H}$ NMR spectrum of SB.....	A-7
Figure A8. $^{13}\text{C}$ NMR spectrum of SB.....	A-8
Figure A9. $^1\text{H}$ NMR spectrum of 4.....	A-9
Figure A10. $^{13}\text{C}$ NMR spectrum of 4.....	A-10
Figure A 11. HSQC spectrum of 4.....	A-11
Figure A12 $^1\text{H}$ NMR spectrum of CB.....	A-12
Figure A13 $^{13}\text{C}$ NMR spectrum of CB. ....	A-13
Figure A14. $^1\text{H}$ NMR spectrum of 6.....	A-14
Figure A15. $^{13}\text{C}$ NMR spectrum of 6.....	A-15
Figure A16. $^1\text{H}$ NMR spectrum of Glc. ....	A-16
Figure A 17. $^{13}\text{C}$ NMR spectrum of Glc. ....	A-17
Figure A18. $^1\text{H}$ NMR spectrum of Ser.....	A-18
Figure A19. $^{13}\text{C}$ NMR spectrum of Ser. ....	A-19
Figure A 20. $^1\text{H}$ NMR spectrum of API-Glc. ....	A-20
Figure A21. $^{13}\text{C}$ NMR spectrum of API-Glc. ....	A-21
Figure A22. ESI-MS spectra of LA-NHS, 2, SB, 4, and CB.....	A-22
Figure A 23. ESI-MS spectra of 6, Glc, API-Glc, and Ser. ....	A-23
Figure A24. Images of pH and ionic strength stability tests for $\text{QD}_{\text{DHLA}}$ .....	A-24
Figure A25. Images of pH and ionic strength stability tests for $\text{QD}_{\text{GSH}}$ .....	A-25
Figure A26. Images of pH and ionic strength stability tests for $\text{QD}_{\text{SB}}$ .....	A-26
Figure A27. Images of pH and ionic strength stability tests for $\text{QD}_{\text{CB}}$ .....	A-27
Figure A28. Images of pH and ionic strength stability tests for $\text{QD}_{\text{Glc}}$ .....	A-28
Figure A29. Images of pH and ionic strength stability tests for $\text{QD}_{\text{Ser}}$ .....	A-29
Figure A30. Images of pH and ionic strength stability tests for $\text{QD}_{\text{API-Glc}}$ .....	A-30
Figure A31. Progress curves of $\text{QD}_{\text{X-Sub}}(\text{A680})_8$ with thrombin.....	A-31
Figure A32. Progress curves of $\text{QD}_{\text{X-Sub}}(\text{A680})_8$ with trypsin. ....	A-32
Figure A33. Progress curves of $\text{QD}_{\text{X-Sub}}(\text{A680})_8$ with papain.....	A-33
Figure A34. Progress curves of $\text{QD}_{\text{X-Sub}}(\text{A680})_8\text{-[Y]}_N$ with thrombin and trypsin .....	A-34

## List of Schemes

Scheme 1. Synthesis of DHLA, LA-NHS, compounds 2, 3, 4, and 5. ....	26
Scheme 2. Synthetic schemes of compounds 5, 6, 7, 8, and 9.....	30
Scheme 3. Proposed synthetic scheme for phosphate-terminating zwitterionic LA. ....	72
Scheme 4. Proposed synthetic scheme for quaternary ammonium terminating cationic LA. ....	73
Scheme 5. Proposed synthetic scheme for PEGylated quaternary ammonium terminating LA. .	73

## List of Abbreviations

A647	Alexa Fluor 647
A680	Alexa Fluor 680
API	1-(3-aminopropyl)imidazole
CB	Carboxybetaine
DCM	Dichloromethane
DHLA	Dihydrolipoic acid
DIC	Diisopropylcarbodiimide
DLS	Dynamic light scattering
DMSO	Dimethylsulfoxide
EDTA	Ethylenediaminetetraacetic acid
ESI-TOF MS	Electrospray ionization time-of-flight mass spectrometry
FRET	Förster resonance energy transfer
FWHM	Full-width-at-half-maximum
Glc	Glucose
GSH	Glutathione
HOMO	Highest occupied molecular orbital
LA	Lipoic Acid
LUMO	Lowest unoccupied molecular orbital
NHS	<i>N</i> -hydroxysuccinimide
Ni-NTA	Ni <sup>2+</sup> -nitrilotriacetic acid
NMR	Nuclear magnetic resonance
PAR	Protease activated receptor
PEG	Poly(ethyleneglycol)
PL	Photoluminescence
QD	Quantum dot
SB	Sulfobetaine
Sub	Substrate
TCEP	Tris(2-carboxylethyl)phosphine
TEAA	Triethylamine acetate

TEM	Transmission electron microscopy
THF	Tetrahydrofuran
TMAH	Tetramethylammonium hydroxide

## Acknowledgements

I have been very fortunate to have encountered so many talented individuals who have inspired and supported me to become a better scientist. I am very thankful to have your help along the way.

To my supervisor, Prof. W. Russ Algar, thank you for introducing me to the field of nanomaterials and all the anomalies associated with it. I very much appreciate the freedom I had to explore and learn from my mistakes, while knowing that there was a safety net and that your door was always open for whenever I was lost or discouraged. Your mentorship both inside and outside the lab cannot be overstated. I am happy to be part of the Algar lab family.

Prof. Tim Storr and Prof. Martin Stillman, you both sparked my interest in research. I'm grateful for your continuous support and acquainting me with the chemistry community. In addition, I would like to extend my thanks to Dr. Michael Jones, Dr. Tyler Pinter, and Dr. Ryan Clarke for taking me under their wings. I learned a lot from you and I wish all the best to your future endeavours.

I have many great friends and colleagues who made these past two years so memorable and enjoyable: Kelsi Lix, Michael Tran, Kelly Rees, Ghinwa Darwish, Dr. Melissa Massey, Dr. Jérémie Asselin, and Xinying Wang. In addition, I want to thank Mo Chaudhry for all our brainstorming sessions – your wild ideas may just serve in your favour. To Dr. William Peveler, I had the pleasure of working with you for less than a year, but I have no doubt that you will go on to achieve your goals and dreams given the dedication and talent I have witnessed for this short duration. To Hyungki Kim, thank you for your encouragements and your unpredictable commentaries – they are often a source of welcoming diversion from our daily grind. Last but not least, to Hsin-Yun Tsai and Rupsa Gupta, we had fumbled through our first couple months of graduate school together, but I can't wait to see the accomplished scientists that you will become at the finish line.

To the supporting staff at UBC: Marshall Lapawa, Dr. Zhicheng Xia, and Dr. Yun Ling, thank you for your enthusiasm and being always ready to troubleshoot my problems with regards to mass spectrometry and NMR spectroscopy.

Outside of the lab, I have Andrew Guthrie to thank for being my rock and keeping me grounded throughout this journey. Despite not knowing much about my field, you put up with my rants and random bursts of ideas for experiments.

Finally, words cannot fully describe my gratitude towards my parents. You are my lifelong teachers and cheerleaders who remind me that successes in life can be defined in innumerable ways. I know that I will always have your unwavering support every step of the way for whichever path I take – and I deeply cherish it.

## Chapter 1 : Introduction

The maturation of nanotechnology has shown quantum dots (QDs) to be a promising platform for bioanalysis. Many applications have exploited the unique combination of their singular electronic, optical, and physical properties. One such application is the use of QDs for the development of model protease assays through Förster resonance energy transfer (FRET). This chapter introduces various fundamental concepts that underly the research presented in this thesis, including the structure, surface chemistries, and optical properties of QDs; fluorescence and FRET; and biosensors and protease assays.

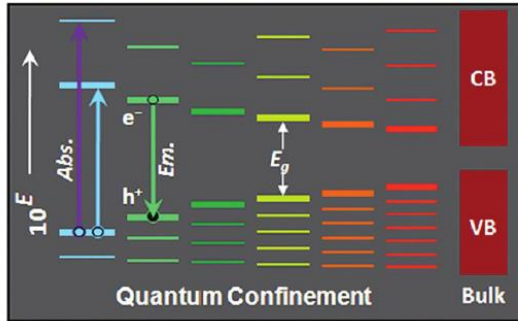
### 1.1 Quantum Dots

QDs are colloidal semiconductor nanocrystals, each consisting of  $10^2$ – $10^4$  atoms, that form a roughly spherical nanoparticle measuring about 1–10 nm in diameter. QDs are one of the most popular and promising materials in nanotechnology. Many studies have utilized the unique and tunable optical properties of QDs via bioconjugation and energy transfer processes to achieve in vitro sensing [1–3], cellular imaging [4,5], and drug delivery [6,7].

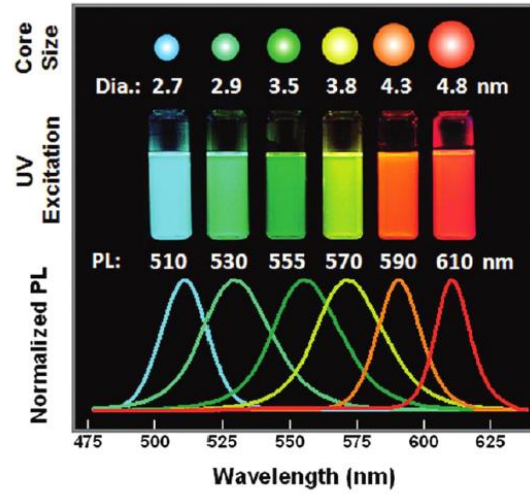
#### 1.1.1 Optical Properties

One of the most attractive features of QDs is the tunability of their electronic and optical properties through their physical size and material selection. The quantum confinement that leads to discrete energy levels at the band edge is unique to nanoparticles because the density of states decreases with decreasing size at the nanoscale, resulting in discrete electronic states [8,9]. When a QD absorbs incident light, an electron can be excited from the ground state, and overcome the bandgap, to an excited state. The loosely-bound electron-hole pair formed during this process is known as an *exciton*. The quantum confinement of the exciton, as well as the band gap, created by the highest occupied level and the lowest unoccupied level, which is analogous to that of the highest occupied molecular orbital (HOMO) and lowest unoccupied molecular orbital (LUMO) of molecular dyes, results in a size-dependent photoluminescence (PL) emission. This emission can be tuned from the visible region to the near-infrared region and beyond for CdSe QDs, as seen in Figure 1.1 (i) and (ii) [10,11]. The emission from QDs is spectrally narrow and symmetric, with an approximately

(i)



(ii)



(iii)

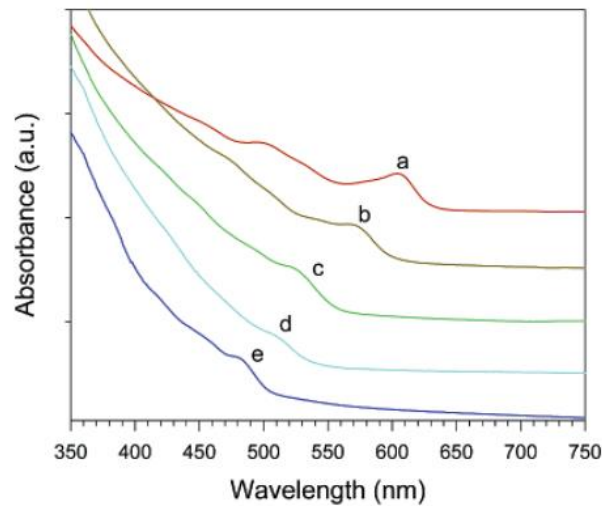


**Figure 1.1.** (i) Qualitative changes in QD quantum confinement with increasing nanocrystal size, where band gap energies,  $E_g$ , were estimated from PL spectra. (ii) Cartoon, photograph, and PL emission spectra of QDs with increasing nanocrystal size. Reproduced from reference [30], copyright 2011 American Chemical Society. (iii) Absorption spectra of  $Zn_xCd_{1-x}Se$  nanocrystals with different Zn mole fractions. Reproduced from reference [39], copyright 2003 American Chemical Society.

Gaussian profile. Typically, the full-widths-at-half-maximum (FWHM) of QDs are in the range of 25–40 nm [10–12], in contrast to that of organic dyes (35 nm–100 nm), whose emission is often

asymmetric and exhibits tailing towards the longer wavelengths [13]. The quantum yields of well-passivated QDs can reach as high as 85% for CdSe QDs emitting in the visible light range [14], and 80% for PbSe nanocrystals emitting in the NIR range ( $\geq 800$  nm) [15]. The fluorescence lifetimes of QDs are on the order of 10–100 ns and typically follow multiexponential decay kinetics [10,16]. The relatively long lifetime is another advantage of QD fluorescence since it potentially allows for temporal discrimination of the signal from possible autofluorescence of the background [17]. Sufficiently surface-passivated QDs are also superior in photostability compared to molecular dyes. The inorganic shell shields the nanocrystalline core from photooxidative bleaching processes [18] by improving the confinement of the exciton to the core [19].

QDs have broad absorption spectra which increase in magnitude towards the near-UV region from the first exciton absorption peak, as seen in Figure 1.1 (iii). The broad absorption gives rise to a large difference between the excitation and emission wavelengths,  $>100$  nm, which helps to minimize interference from spectral overlap between the QD absorption and emission. Molar absorption coefficients of QDs are on the order of  $10^4$ – $10^7$   $\text{M}^{-1} \text{cm}^{-1}$  for the first exciton peak, which are about 10–100 times that of organic dyes [11,12,20].

### 1.1.2 Structure and Composition

Besides the size-dependency of QDs, there are also other structural features that can influence the optical properties of QDs as well. Two of the most common types of QDs include (i) a single nanocrystalline core, and (ii) a nanocrystalline core with another type of semiconductor as its shell. The core-shell structure offers yet another layer of tunability to the QDs and core-shell QDs are most commonly used in applications because of their superior stability and quantum yield [21,22]. Other well-studied structures of QDs include core/shell/shell and alloyed QDs. Core/shell/shell QDs introduces a middle layer which can reduce the lattice mismatch between the core and shell. Such is the case for CdSe/ZnS QDs with a mismatch of ca. 12% compared that to the core/shell lattice mismatch of ca. 4% for CdSe/CdS/ZnS QDs [23,24]. Core/shell/shell-structured QDs often have a higher PL efficiency as well as better photostability than core/shell-structured QDs. Alloyed QDs can also add another degree of freedom in the QD emission via changes to either its core size or chemical composition. This is in contrast to the size-only tunability emission of binary QDs [25,26].

One of the advantages of a core-shell structure is the minimization of non-radiative relaxation processes. Such processes occur in the nanocrystalline core from the inevitable structural defects that arise from the different chemistry at the surface of the nanocrystal in comparison to its interior. Substantial surface reconstruction, vacancies, lattice mismatch, and interactions with impurities or adsorbates all contribute towards the surface states that act as traps for electrons and holes [9,18,27]. The addition of another material of a larger band gap passivates the surface of the crystalline core and more effectively confines the exciton to decrease the rates of non-radiative processes [9,18,27].

Popular combinations of materials include a CdSe core and a ZnS shell, which is an example of type I QD, where the band gap energy of the shell exceeds the band gap of the core and can confine both the electron and hole to the core. In contrast to type I QDs, type II QDs have cores where the conduction and valence band edges are both either lower or higher in energy than the corresponding shell band edges. The spatial separation of the charge carriers results in lower quantum yield and lower rate of radiative recombination, which translates into less favourable optical performance. However, type II QDs can be potentially advantageous where rapid charge separation and charge transfer is needed, e.g. photovoltaics applications [28].

### **1.1.3 QD Surface Coatings**

Since the traditional and best QD synthesis protocols typically use hydrophobic ligands, such as trioctylphosphine oxide (TOPO), oleic acid, and alkyl amines for surface passivation [29], further surface functionalization of QDs is needed for subsequent applications and colloidal stability in an aqueous environment. A few important considerations for the surface ligands include (i) strong binding to QDs, (ii) stability across a broad range of pH and salt concentrations, (iii) minimal non-specific interactions with biomolecules, and (iv) low toxicity [10].

Colloidal stability of QDs in aqueous environment can be achieved through various strategies. Most commonly, they can be rendered colloidally stable in aqueous solutions by (i) ligand exchange with hydrophilic ligands containing an anchoring group, (ii) encapsulation with an

amphiphilic polymer that displays hydrophilic groups on the surface, and (iii) encapsulation with a silica shell [10,12,30]. The various methods can be seen in Figure 1.2.

One of the most popular types of ligands have thiolate groups as anchors because of their high affinity, via dative bonds, for cadmium, zinc, and other commonly used metals for QDs. Examples of monodentate thiolate ligands include mercaptoacetic acid, mercaptopropionic acid, and mercaptoundecanoic acid. These ligands typically contain carboxyl groups that need to be deprotonated in aqueous environment to ensure colloidal stability, which results in instability at lower pH range ( $\text{pH} < 6$ ). The coulombic repulsion between the carboxyl groups that aids in the stable dispersion of QDs can also be shielded at high salt concentrations and the particles tend to precipitate at salt concentrations around a few hundred millimolar. Another weakness of monodentate thiolate ligands is the dynamic nature of thiolate-ZnS bonds that affords poor long-term stability (sometimes  $< 1$  week) [12,31]. Bidentate thiolate ligands, such as dihydrolipoic acid

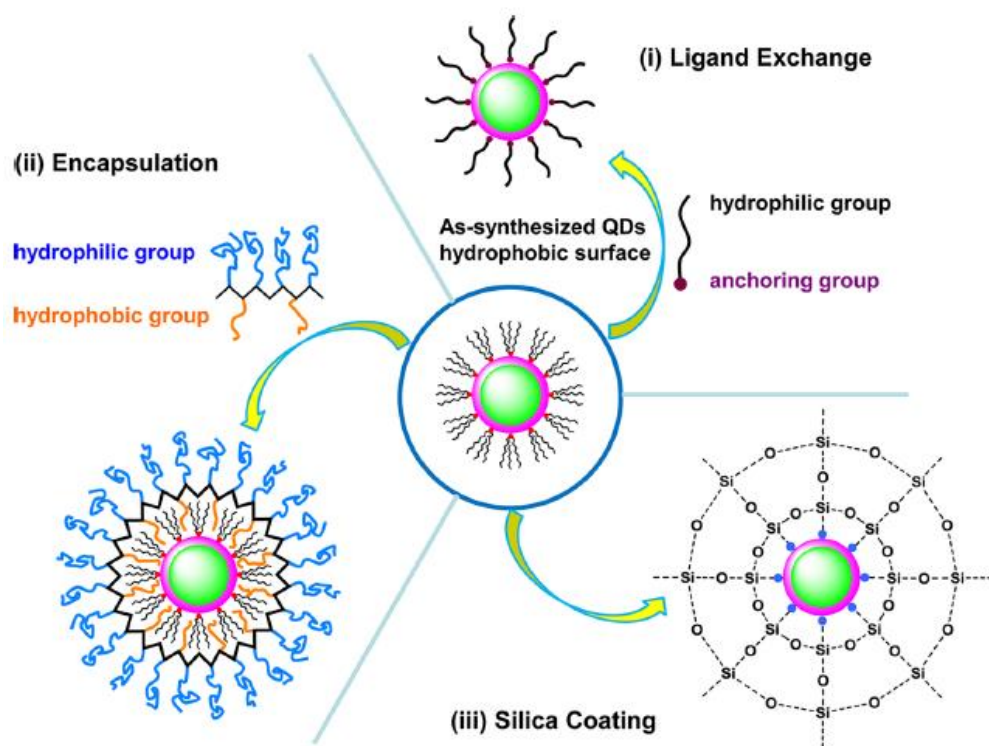


**Figure 1.2.** Different strategies to render QDs colloidal stable in aqueous environment: (i) ligand exchange, (ii) encapsulation with an amphiphilic polymer, (iii) encapsulation with a silica shell. Reproduced from reference [30], copyright 2011 American Chemical Society.

(DHLLA), have also been investigated for surface functionalization of QDs. In addition to a stronger affinity for the QD surface and better long term colloidal stability, DHLLA can be synthetically modified with poly(ethyleneglycol) (PEG) and zwitterionic moieties to achieve QDs with even better stability and biocompatibility [12,32,33]. Other DHLLA-based polydentate ligands have also been developed and various studies suggest that some may offer even better stability than the bidentate counterpart [34–36]. Ligand exchange methods typically yield QDs with small hydrodynamic size but lower quantum yield. This is likely caused by the surface defects introduced when the native ligands are stripped off [10], or in the particular case of thiolate ligands, the reduction of surface electron trap and the introduction of new hole trap states by thiolate at high concentrations [37].

Unlike the ligand exchange method, encapsulation of QDs with amphiphilic block polymers preserve the native ligands on the surface of QDs. Hydrophobic chains of amphiphilic polymers are interdigitated into the native ligands by hydrophobic interactions while the hydrophilic polymer groups/chains are displayed on the surface of QDs for colloidal stability. Various diblock and triblock copolymers have been reported, including many employing PEG, poly(acrylic acid), and polystyrene [38–41]. Encapsulation of QDs with polymers can provide further functionalizable groups and potentially better stability over a broader pH range than the ligand exchange method. However, this method tends to produce larger hydrophilic QDs (20–30 nm) [12], which can limit their applications for intracellular studies or distance-dependent energy transfer processes.

Silica shell encapsulation is another means to achieve QD colloidal stability. The electrical double layer, which is formed by a “layer” of ions that adsorb to the surface of a material followed by another layer of ions that are attracted to the first layer of ions, is thought to be responsible for the solvation of silica-coated QDs [42]. This method has the advantages of enhancing the stability of QDs over a larger range of pH and ionic strengths than the ligand-exchange method and the possibility to introduce other functionalities to the surface siloxane groups [42–45]. However, similar to the amphiphilic block polymer encapsulation, the QDs encapsulated in silica have a shell of non-negligible thickness of 3–7 nm [42–47].

### 1.1.4 QD Bioconjugation

An important property of QDs is their exceptionally large surface area-to-volume ratio which makes them an excellent scaffold for attaching biomolecules. Among others, oligonucleotides, peptides, enzymes, antibodies, and oligosaccharides are some of the previously reported targeting biomolecules used for sensing with QDs [48–54]. Bioconjugation strategies for QDs can be roughly divided into three categories: (i) covalent modifications, (ii) coordination bonding, and (iii) electrostatic interactions.

A method of covalent modification on the QD surface is the reaction between amines and activated carboxylic acids via carbodiimides, such as 1-ethyl-3-(3-dimethylaminopropyl)carbodiimide (EDC) to form an amide bond. Since carboxylic acid groups are commonly used to render QDs soluble and therefore readily available, carbodiimide coupling is a popular approach. On the down side, the loss of the carboxylic acid groups presents a potential challenge to the colloidal stability in the event of over-crosslinking [55]. In addition, the activated *o*-acylisourea intermediate is susceptible to hydrolysis and an excess of carbodiimide is often used in practice to drive the reaction forward which further exacerbates the problem of over-crosslinking. An alternative strategy is to form a more stable intermediate that is less prone to hydrolysis, such as succinimidyl ester using *N*-hydroxysuccinimide (NHS), from the reactive *o*-acylisourea intermediate.

Another modification method transforms amines on the QD surface via crosslinking with bifunctional reagents such as succinimidyl-[*N*-maleimidomethyl]cyclohexane-1-carboxylate (SMCC) to impart maleimide groups on QDs [56]. Biomolecules with free thiols, such as proteins with reduced cysteine residues, can then be conjugated to the QDs. Copper-free click reaction is yet another covalent conjugation strategy. Unlike the traditional copper-catalyzed azide-alkyne cycloaddition (CuAAC), the copper-free click chemistry does not limit the biological applications of QDs nor compromise the QD PL as a result of the required  $\text{Cu}^+$  catalyst. Copper ions can red-shift the QD emission band and precipitate ultrasmall  $\text{Cu}_x\text{S}$  particles on the surface of QDs, both of which facilitate the non-radiative recombination of the exciton [57]. Copper-free click chemistry avoids the problems associated with the copper catalyst by making use of the reactivity of a strained cycloalkyne [58]. Azide-modified biomolecules can then undergo a [3+2] cycloaddition to form a stable triazole linkage under mild aqueous conditions to obtain modified QDs with high

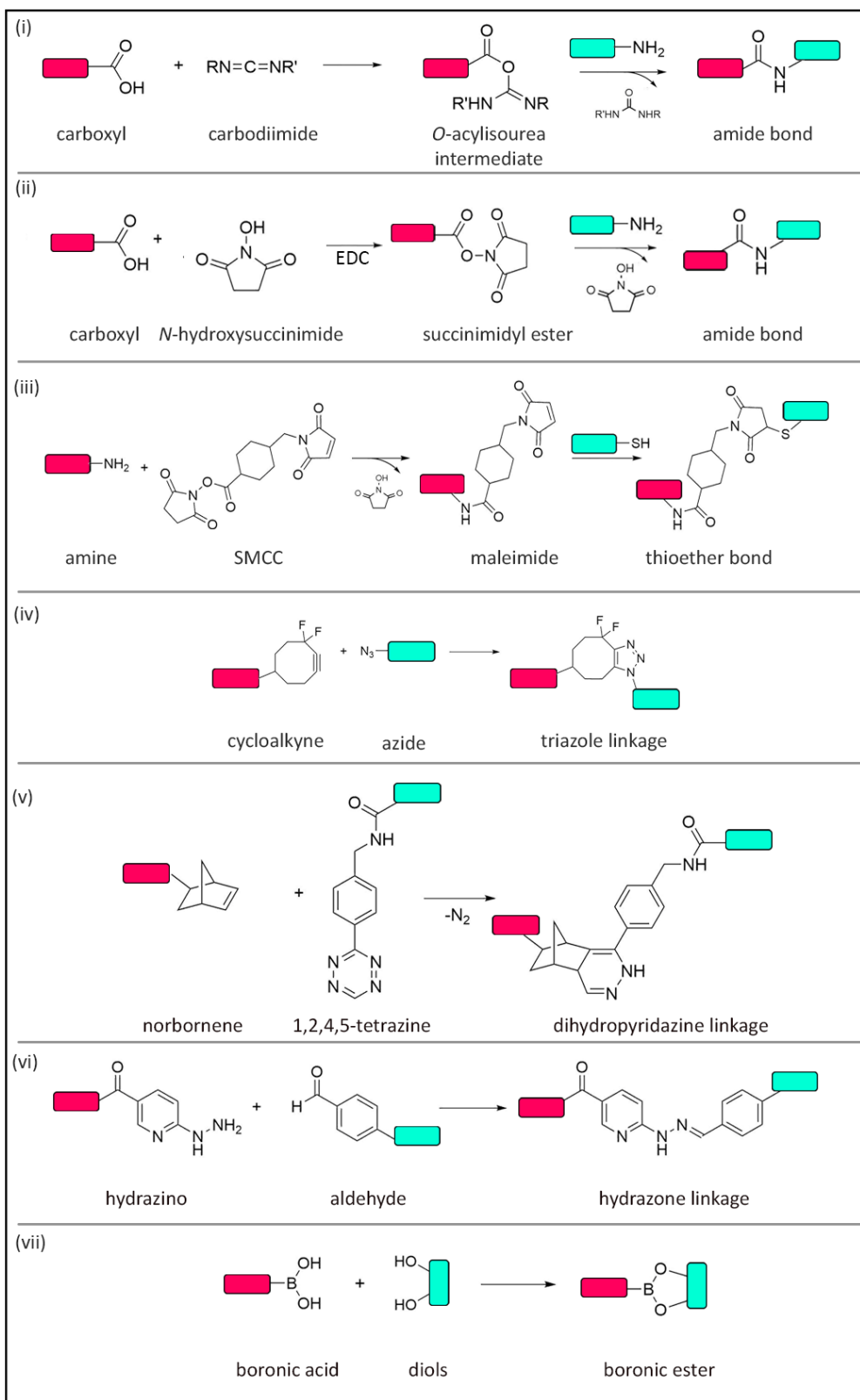


**Figure 1.3.** (Previous page) Different covalent conjugation chemistries. (i) and (ii) Carbodiimide-activated coupling between a carboxylic acid and an amine. (iii) Conjugation between a bifunctional crosslinker, sulfosuccinimidyl-4-(*N*-maleimidomethyl)cyclohexane-1-carboxylate (SMCC), which allows a second conjugation to a thiol group. (iv) Copper-free click chemistry between an azide and a strained cycloalkyne to form a triazole linkage. (v) Cycloaddition conjugation between a strained alkene (norbornene) and tetrazine. (vi) Hydrazone ligation between a hydrazine and a carbonyl group. (vii) Conjugation via condensation between boronic acid and a diol.

PL [59,60]. Other covalent modifications include, but are not limited to, dihydropyridazine [61,62], hydrazone [63,64], and boronic ester [65–67] ligations. A summary of the different covalent conjugation chemistries can be seen in Figure 1.3.

Coordination or dative bonding is also a common strategy to form bioconjugates. Unlike the relatively stable covalent bonds, coordination bonds are more sensitive to the relative concentrations of QDs and the coordinating biomolecules both during preparation and subsequent applications [55]. The stability of the bioconjugates is better described by the equilibrium dissociation constant,  $K_d$ . Coordination bonding is often preferred for its equilibrium driven self-assembly as well as its rapid bioconjugation.

Polyhistidine sequences are a popular method to introduce multidentate coordination sites to peptides and proteins. The large affinity of the polyhistidine motif towards QDs is driven by the imidazole groups coordinating to the  $Zn^{2+}$  ions in the ZnS inorganic shell. Equilibrium is reached rapidly after mixing (~100–200 s) and typical dissociation constants have been reported to be on the order of  $K_d \approx 10^{-10}$ – $10^{-7}$  M [68], which is comparable to that of antigen-antibody interactions ( $K_d > 10^{-9}$  M) [69]. The motif offers a simple way to bioconjugation without disrupting the structure of the biomolecules. However, this method is not available to QDs where the inorganic surface is inaccessible or coated with bulky ligands. Nonetheless, there is an alternate method: QDs modified with nickel(II)-nitrilotriacetic acid ( $Ni^{2+}$ -NTA) or its derivatives can also be conjugated to biomolecules with polyhistidine tags. Similar to the coordination to the  $Zn^{2+}$  ions in the inorganic shell, the conjugation of polyhistidine to  $Ni^{2+}$ -NTA complexes reaches equilibrium in ~200 s [70], and the complexes have been reported to be stable intracellularly for a few hours without signs of aggregation [71]. Similarly, QD surfaces displaying carboxylic acid groups can

also coordinate to  $\text{Ni}^{2+}$  ions and provides new scaffolds to conjugate to polyhistidine-tagged biomolecules [72]. Various coordination chemistries are summarized in Figure 1.4.

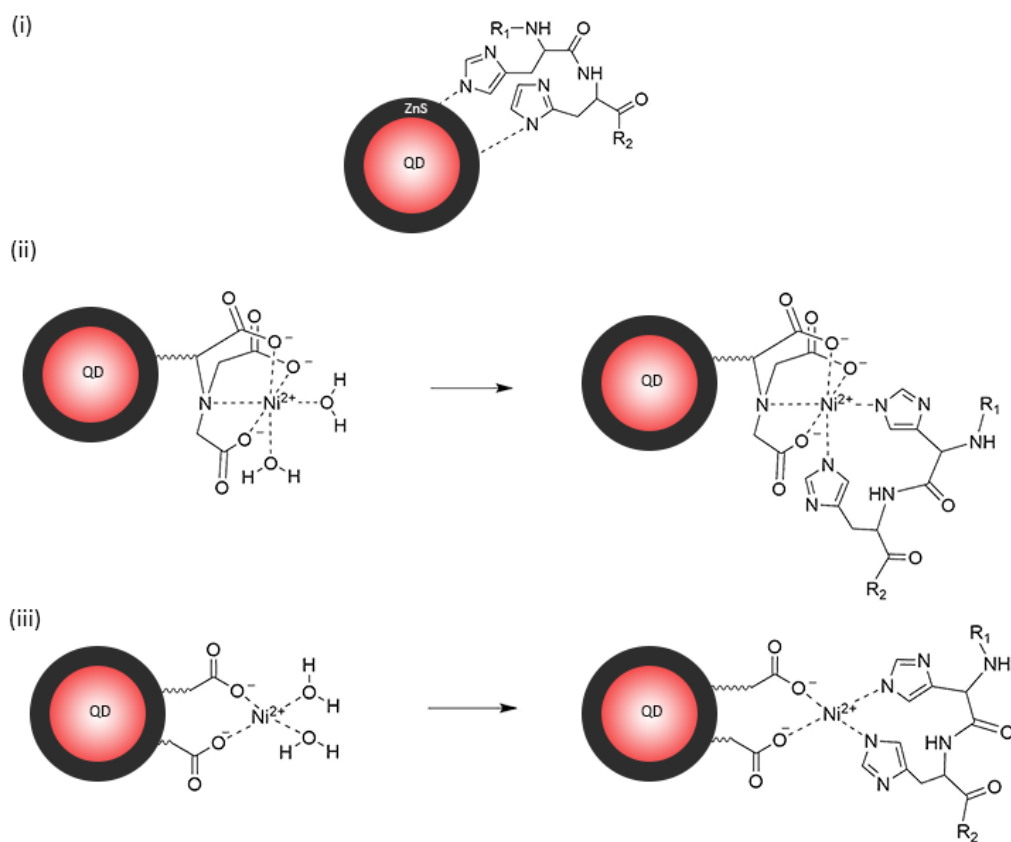


**Figure 1.4.** Various coordination chemistries to form QD bioconjugates.  $R_1$  and  $R_2$  denote the N-terminus and C-terminus of peptides, respectively. (i) Polyhistidine tag coordinating to the  $\text{Zn}^{2+}$  in the ZnS shell. (ii) and (iii) Nickel-nitrilotriacetic acid-modified and carboxylic acid-functionalized QDs forming bioconjugates via coordination by the imidazole groups of histidines.

The use of electrostatic interactions for bioconjugation is relatively straightforward because of the readily available charged functional groups on the coated ligands as well as the commercially available carboxylic acid functionalized QDs. Previous studies have reported the conjugation of proteins, single stranded DNA (ssDNA), and RNA [73–76]. However, electrostatic interactions are sensitive to changes in pH and ionic strength. The range of the bioconjugate’s stability could also be limited by the isoelectric point (pI) of the biomolecule.

Avidin-biotin ligand binding is a powerful tool for conjugation. The high specificity and affinity of this interaction ( $K_d \sim 10^{-15}$ ) [77], as well as the commercially available biotinylated antibodies, proteins, and DNAs, makes this method a popular choice in QD conjugation. Various bioconjugates, including antibodies, oligonucleotides, proteins, and peptides, have been prepared using the interactions between biotin and avidin, or variations of avidin (streptavidin or deglycosylated, neutral form of avidin) [78–82].

## 1.2 Fluorescence

Luminescence is defined as the radiative emission from an electronically or vibrationally excited species. Specific types of luminescence include *photoluminescence* (PL), *chemiluminescence*, *bioluminescence*, and *electroluminescence*, where the emission is caused by photon absorption, a chemical reaction, a biochemical process, and an electrical current, respectively. PL can be further defined as *fluorescence*, which is the relaxation of the excited species without a change in its spin multiplicity, and *phosphorescence*, which is the relaxation of the species after it undergoes transition into a higher spin multiplicity state. A *fluorophore* is a molecular entity that can emit fluorescence.

After a fluorophore absorbs a photon, it can undergo various electronic and vibrational transitions as depicted by Jablonski diagrams in Figure 1.5. The diagrams represent the molecular electronic states as potential energy wells. The singlet electronic states: ground, first, and second are labeled as  $S_0$ ,  $S_1$ , and  $S_2$ , respectively. Within each electronic state, there are multiple vibrational energy states ( $v_n$ ). When a fluorophore undergoes excitation, it is usually excited to higher vibrational and electronic states. The absorption of light is an extremely fast process ( $10^{-15}$  s) compared to that of molecular vibrations ( $10^{-10}$ – $10^{-12}$  s), and electronic transitions occur with virtually no change to the positions of the nuclei. The Franck-Condon principle describes all electronic transitions as vertical transitions from the ground state potential energy at equilibrium to the turning points of excited states, where the momentum is zero, and that the most probable transition occurs where the excited state most resembles the ground state in terms of the vibrational wavefunction [83]. The excited state then rapidly undergoes vibrational relaxation to the lowest vibrational state of  $S_1$ , generally before the occurrence of other relaxation pathways and regardless of the initial transition (Kasha's rule) [84]. The process occurs on the order of  $10^{-12}$  s [85] and results in a general property

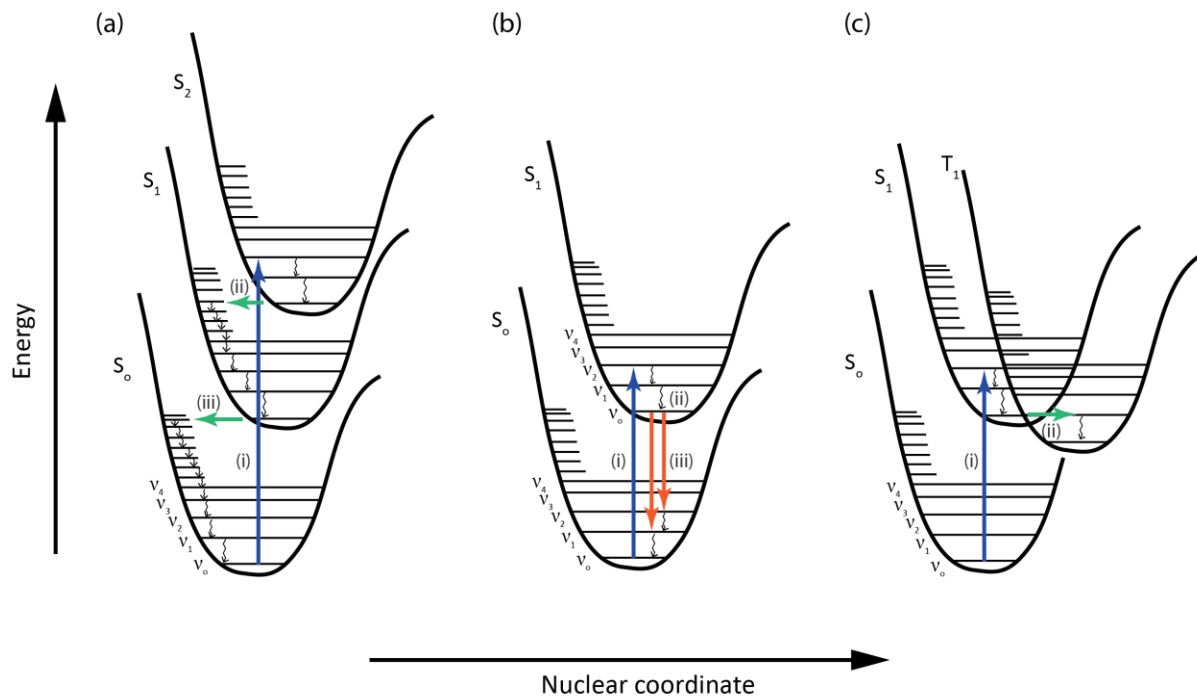


**Figure 1.5.** Jablonski diagrams depicting competing radiative and non-radiative pathways. The electronic states,  $S_n$ , are shown as potential energy wells with overlapping vibrational states,  $v_n$ . Absorbance is denoted by blue arrows, vibrational relaxation by black arrows, internal conversion by green arrows, and photoluminescence by orange arrows. (a) An example of non-radiative relaxation pathway after the absorption of a photon. After the excitation from  $S_0v_0$  to  $S_2v_2$  (i), the molecule undergoes vibrational relaxation to  $S_2v_0$ , followed by internal conversion (ii) to  $S_1v_8$  and vibrational relaxation to  $S_1v_0$ , and lastly, it undergoes internal conversion from  $S_1v_0$  to  $S_0v_{11}$  (iii), and returns to the ground state through vibrational relaxation. (b) An example of radiative relaxation pathway. After the absorption of a photon (i), the molecule undergoes vibrational relaxation to  $S_1v_0$  (ii) before it returns to the ground state by fluorescence (iii) and vibrational relaxation. (c) Another example of possible relaxation pathway. After the absorption of a photon (i), the molecule undergoes vibrational relaxation from  $S_1v_2$  to  $S_1v_0$  and intersystem crossing (ii) to  $T_1v_1$  before vibrationally relax down to  $T_1v_0$ . It can then relax back to the ground state via a radiative pathway through phosphorescence or non-radiative pathways. Due to the long phosphorescence lifetimes, the latter is generally observed.

of fluorescence: the emission spectrum is independent of the excitation wavelength. The excited electron at the lowest vibrational excited state can then relax back to the ground state,  $S_0$ , via several different pathways. One possibility is to undergo internal conversion to a higher vibrational state of  $S_0$ , followed by vibrational relaxation. In the case of fluorescence, the electron loses its

energy in the form of a photon. Fluorescence lifetimes are typically around  $10^{-10}$ – $10^{-7}$  s, which is much slower than that of internal conversion. Hence, fluorescence emission generally results from an equilibrated excited state, i.e.  $S_1v_0$  [85]. Electrons in the  $S_1$  state can also undergo intersystem crossing or spin conversion to the triplet state,  $T_1$ . Radiative relaxation from  $T_1$  to the ground state is a relatively slow process ( $10^{-4}$ – $10^2$  s) because the transition from the excited electron to the ground-state electron requires a change in the spin orientation and is therefore forbidden by the selection rule [85]. Since phosphorescence is a very slow and inefficient process, the molecule usually relaxes back to the ground state via non-radiative processes. *Quantum yield* is the efficiency at which the fluorophore undergoes fluorescence emission instead of other relaxation pathways to return to the ground state.

### 1.2.1 Fluorescence Quenching

Any process that results in decreasing fluorescence intensity can be referred to as fluorescence quenching, which is highly dependent on the local environment of the fluorophore. For intermolecular quenching, most of the processes involve transfer of an electron, a proton, or energy from a donor to acceptor. Various ions and molecules, including molecular oxygen, can act as quenchers and quenching processes can be loosely categorized as *static quenching*, *dynamic quenching*, or a combination of the two processes [83,85]. Static quenching refers to the formation of a ground-state non-fluorescent complex, or the complete quenching of a fluorophore by a quencher inside the *sphere of effective quenching*. This occurs when the positions of two molecules are fixed for the excited lifetime of the fluorophore, such as the case of a quencher-fluorophore pair in a viscous medium [83]. Dynamic quenching refers to the quenching of a fluorophore in the excited state. Intermolecular collision is often cited as a source of dynamic quenching; however, it also includes other mechanisms such as energy transfer and electron transfer. Dynamic quenching affects both the quantum yield and fluorescence lifetimes, whereas static quenching affects only the quantum yield [86]. Quenching can also occur by photoinduced reactions involving transfer of an electron, proton, or energy, or the formation of a dimer or complex in the excited state, which are referred to as *excimer* and *exciplex*, respectively [83]. It should be noted that fluorescence quenching is a photophysical process, after which the fluorophore is de-excited and returns to the ground state unaltered. In contrast, photochemical processes, which involve

photoinduced bond breaking and formation of new bonds, tend to result in the non-reversible decrease in fluorescence, as is the case in *photobleaching*.

### 1.2.2 Excited-state Lifetimes

The rate of molecular de-excitation can be probed with a delta pulse of light, whose duration is relatively short compared to the timescale of relaxation processes. When a number of molecules,  $A$ , is excited to the  $S_1$  state by the absorption of photons at time  $t = 0$ , the excited molecules can return to  $S_0$  through either radiative or non-radiative pathways, or undergo intersystem crossing [83]. In the absence of intermolecular interactions, the rate of the disappearance of the excited-state molecules can be described by eqn. 1, where  ${}^1A^*$  is the excited species,  $k_r$  the rate of radiative processes ( $S_1 \rightarrow S_0$  with the emission of fluorescence),  $k_{nr}$  the rate of non-radiative processes ( $S_1 \rightarrow S_0$ ).

$$-\frac{d[{}^1A^*]}{dt} = (k_r + k_{nr})[{}^1A^*] \quad \text{Eqn. 1}$$

Integration of eqn. 1 leads to eqn. 2, where  $[{}^1A^*]_0$  is the concentration of the excited molecules at  $t = 0$ , and  $\tau$  the lifetime of the excited state  $S_1$  as given by eqn. 3.

$$[{}^1A^*] = [{}^1A^*]_0 \exp\left(-\frac{t}{\tau}\right) \quad \text{Eqn. 2}$$

$$\tau = \frac{1}{k_r + k_{nr}} \quad \text{Eqn. 3}$$

The fluorescence intensity,  $I_F$ , observed at time  $t$  after the absorption of light is proportional to the instantaneous population of the excited-state molecules and can be described by eqn. 4, where  $I_0$  is the fluorescence intensity at  $t = 0$ . The fluorescence intensity of a fluorophore decreases following a single exponential decay model.

$$I_F = I_0 \exp\left(-\frac{t}{\tau}\right) \quad \text{Eqn. 4}$$

Experimentally, one of the most commonly used models for the decay of fluorescence is the multi-exponential model, which includes the sum of individual single exponential decays (eqn. 5) [85].

Such a model may be needed when a single or a mixture of fluorophores display a more complex decay behavior than single exponential decay. The interpretation of the decay times depends on the individual system. In the case of a fluorophore displaying a complex decay, it is likely that the fluorophore is undergoing radiative decay in different environments. Thus, in eqn. 5,  $\alpha_i$  values represent the fraction of the fluorophore in each discrete environment at  $t = 0$ . In the case of a mixture of fluorophores, the  $\alpha_i$  values reflect the concentrations, absorption, quantum yields, and intensities of each fluorophore in the sample.

$$I_F = \sum_{i=1}^n \alpha_i \exp(-t / \tau_i) \quad \text{Eqn. 5}$$

Because the fluorescence lifetimes are on the nanosecond timescale, fluorophores reach steady-state almost instantaneously. As a result, steady-state fluorescence measurements, which involve continuous illumination (i.e. with constant incident light intensity) and observation, are more common than time-resolved measurements [86].

### 1.2.3 Fluorescence Intensity and Quantum Yield

In highly diluted solutions, where absorbance of the sample is less than 0.05, the fluorescence emission intensity is given by eqn. 6, where  $\varepsilon$  denotes the molar extinction coefficient of the fluorophore (in  $\text{L mol}^{-1} \text{cm}^{-1}$ ),  $l$  the optical path in the sample (in cm),  $c$  the concentration of the sample (in  $\text{mol L}^{-1}$ ),  $F_\lambda$  the variation in the fluorescence intensity of the spectrum per unit wavelength with the normalization  $\int_0^\infty F_\lambda d\lambda = \Phi$  (see below),  $I_o$  the incident light, and  $k$  the proportionality factor [83]. The constant  $k$  depends on many factors, including the optical configuration for observation (i.e. the angle and distance between the instrument and the sample) and the bandwidth of the monochromators. Since most experiments involve manipulating only one variable in the equation that is external to the instrumental setup, the absolute values of the instrumental factors can be approximated as constants or corrected.

$$I_F = 2.3\varepsilon l c F_\lambda I_o k \quad \text{Eqn. 6}$$

The quantum yield of a fluorophore can be described as the ratio of the number of photons emitted to the number of photons absorbed. Mathematically, the quantum yield  $\Phi$  is the ratio of the radiative rate over the rate of all the processes [83]. In eqn. 7,  $k_r$  is the rate of radiative process,  $k_{nr}$  the sum of the rates of non-radiative processes, including intersystem crossing, internal conversion, and energy transfer,  $k_q$  the rate of quenching and  $Q$  the quencher of the fluorophore. The expression can be further simplified by substitution using eqn. 3. As seen from eqn. 7, in the absence of a quencher, the quantum yield of a fluorophore is the product of the rate of radiative process and the excited-state lifetime.

$$\Phi = \frac{k_r}{k_r + k_{nr} + k_q [Q]} = \frac{k_r}{\frac{1}{\tau} + k_q [Q]} \quad \text{Eqn. 7}$$

Quantum yield of a sample is usually determined by comparison to a standard. The fluorescence spectra of the unknown and the standard are recorded at low sample concentrations (absorbance < 0.05), to minimize inner filter effects, and under the same experimental conditions, including instrumental set-up and temperature. As seen in eqn. 8, where the subscript  $R$  denotes the reference fluorophore of known quantum yield and  $A$  the absorbance at the emission wavelength, quantum yield is determined by the ratio of the integral of the fluorescence spectra. Correction is introduced for the differences in optical densities and for the refractive index  $n$  of the solvents if needed.

$$\frac{\Phi}{\Phi_R} = \frac{\int_0^\infty I(\lambda) d\lambda}{\int_0^\infty I_R(\lambda) d\lambda} \times \frac{1-10^{A_R}}{1-10^A} \times \frac{n^2}{n_R^2} \quad \text{Eqn. 8}$$

#### 1.2.4 Förster Resonance Energy Transfer

One of the non-radiative processes that can occur when a fluorophore is in the excited state is resonance energy transfer (RET), which refers to the coupling of electronic transitions between a donor and an acceptor when they have virtually the same energy and there is spectral overlap between the emission spectrum of the donor and absorption of the acceptor. Such an energy transfer is not dependent on the emission of a photon from the donor but rather the non-radiative transfer of electronic energy from the donor to the acceptor. Energy transfer can be the result of long-range (80–100 Å) dipole-dipole interactions via Förster's mechanism, which is commonly

referred to as Förster Resonance Energy Transfer (FRET), or short-range ( $\leq 10 \text{ \AA}$ ) interactions through intermolecular orbital overlap, such as Dexter electron exchange [83].

For FRET, the long-range coupling is very weak and the rate of the energy transfer depends on the interaction between the rotating dipoles in solution. Thus, the rate of the energy transfer has a sixth power distance dependence instead of the third that is normally the case for dipole-dipole interactions (eqn. 9). In the following equation,  $r$  is the distance between the donor and acceptor,  $k_r$  the emission rate constant of the donor,  $\tau_D$  the lifetime of the donor in the absence of energy transfer, and  $R_0$  the Förster distance at which the donor emission is equally probable as the energy transfer ( $k_{FRET} = k_r$ ).

$$k_{FRET} = (k_r + k_{nr}) \left[ \frac{R_0}{r} \right]^6 = \frac{1}{\tau_D} \left[ \frac{R_0}{r} \right]^6 \quad \text{Eqn. 9}$$

Experimentally, the Förster distance (in  $\text{\AA}$ ) can be determined by eqn. 10 and 11 where  $\kappa^2$  is the orientational factor,  $\Phi_D$  is the fluorescence quantum yield of the donor in the absence of FRET,  $J$  the spectral overlap integral ( $\text{M}^{-1} \text{ cm}^3$ ),  $N_A$  the Avogadro's number,  $n$  the average refractive index of the medium [86]. When the molecular rotations are much faster than the de-excitation rate of the donor, the average value of  $\kappa^2$  is 2/3, whereas the value for  $\kappa^2$  is 0.476 for a system of acceptors randomly distributed about a donor in a rigid medium. Typical  $R_0$  values are generally in the range of 15–60  $\text{\AA}$  [83].

$$R_0^6 = \frac{9(\ln 10)\kappa^2\Phi_D J(\lambda)}{128\pi^5 N_A n^4} = 8.79 \times 10^{-28} (\kappa^2 n^{-4} \Phi_D J(\lambda)) \quad (\text{in cm}^6) \quad \text{Eqn. 10}$$

$$R_0 = 3.09 \times 10^{-5} (\kappa^2 n^{-4} \Phi_D J(\lambda))^{1/6} \quad (\text{in cm}) \quad \text{Eqn. 11}$$

Similar to quantum yield, where the efficiency can be calculated by the ratio of the rate of radiative processes over the sum of all processes, FRET efficiency can be defined as eqn. 12. Substitution from eqn. 9 into the left-hand side of eqn.12 yields the expression on the right.

$$E_{FRET} = \frac{k_{FRET}}{k_{FRET} + (k_r + k_{nr})} = \frac{R_0^6}{R_0^6 + r^6} \quad \text{Eqn. 12}$$

Alternatively, the FRET efficiency can be described by measurable differences in fluorescence intensity  $F$ , quantum yield  $\Phi$ , or fluorescence lifetimes  $\tau$  as the following relationship, where  $D$  denotes the donor in the absence of an acceptor and  $DA$  denotes the donor in the presence of an acceptor.

$$E_{FRET} = 1 - \frac{F_{DA}}{F_D} = 1 - \frac{\Phi_{DA}}{\Phi_D} = 1 - \frac{\tau_{DA}}{\tau_D} \quad \text{Eqn. 13}$$

Eqn. 13 shows that FRET efficiency can be determined by time-resolved measurement of fluorescence lifetimes and the fluorescence decay of the donor is expected to follow a single exponential model as previously mentioned in section 1.2.2. It should be noted that if the decay is not a single exponential in the absence of acceptor, it is likely the result of a distribution of the donor in a heterogenous microenvironment or differences in donor-acceptor distance.

If both the individual quantum yields of the donor and acceptor are known and there is negligible direct excitation of the acceptor, the relationship between FRET ratio and FRET efficiency can also be calculated using the FRET ratio, which is the ratio of the acceptor emission when coupled to the donor  $F_{AD}$  to the donor emission  $F_{DA}$ , where AD denotes acceptor in the presence of the donor, and DA denotes the donor in the presence of the acceptor.

$$\frac{F_{AD}}{F_{DA}} = \frac{\Phi_A E_{FRET}}{\Phi_D (1 - E_{FRET})} \quad \text{Eqn. 14}$$

### 1.3 Biosensors and Enzyme Assays

Biosensors can be defined as a device that quantitatively detects a biologically-relevant analyte and incorporates a physicochemical transducer component that can generate a signal proportional to the analyte concentration. Since the development of the first glucose sensor in 1962 by Lyons and Clark, many other commercially available biosensors have been created, such as human chorionic gonadotropin (hCG) for pregnancy tests,  $\beta$ -glucuronidase for the detection of *Escherichia coli*, immunoglobulin G (IgG) for *Helicobacter pylori*, and many more in clinical settings. Still others have been developed for drug discovery, food safety, biothreat and warfare. An ideal biosensor should have good sensitivity and selectivity, in addition to being either high-

throughput or portable. The former would allow for rapid screening of many samples, while the latter would allow for point-of-care diagnostics.

Selectivity in biosensors is achieved by incorporating recognition elements such as aptamers, antibodies, enzymes, nucleic acid sequence, and enzyme substrates. Enzyme/substrate pairs are popular recognition elements when designing a biosensor due to the nature of enzyme activities. Enzymes' active sites bind to substrates through non-covalent interactions and convert substrates into products with turnover numbers typically around several thousand. The catalytic residues of enzymes are generally ubiquitous and conserved across species, which make enzyme-based biosensors useful for targeting specific biochemical reactions while still being applicable to different populations.

Enzyme assays are usually incorporated into biosensors by interacting with an analyte in such a way that can be detected by optical [87], piezoelectric [88], or electrochemical transducers [89]. Likewise, many biochemical reactions can be coupled to another reaction to generate signal-producing products [90,91]. The activities of enzymes of interest can then be correlated to certain diseased states and these biomarkers are useful for monitoring or diagnosing diseases such as prostate cancer, bone metastasis, and hemolytic anemia, among others [92–94].

### **1.3.1 Proteolysis**

Enzymes can be classified into six categories: (i) oxidoreductases, which catalyze redox reactions; (ii) transferases, which transfer a functional group from one molecule to another; (iii) hydrolases, which help to break substrate's covalent bond with the aid of water; (iv) lyases, which catalyze the addition or removal of a substrate functional group without the aid of water; (v) isomerases, which catalyze isomerization; and (vi) ligases, which catalyze the joining of two substrates while coupled to the hydrolysis of nucleoside triphosphate [95].

In particular, proteases, which fall under the class of hydrolase, are of special interests because these enzymes are part of the regulatory mechanisms to ensure the balance of protein synthesis and degradation. Abnormal activities of proteases usually indicate a disturbance to cellular homeostasis and potentially lead to diseases. Examples of protease dysregulations can be seen in

calpains, which have been found to be associated with muscular dystrophy, cataract formation, Alzheimer's disease, and more [96]; caspases, which are involved in inflammatory response and mediate cytotoxicity by amyloid- $\beta$  [97,98]; and thrombin, which is associated with tumour progression [99]. The irreversible nature of proteolysis coupled to the clinical significance of proteases make them an attractive target for biosensors.

### 1.3.2 Michaelis-Menten and Briggs-Haldane Kinetics

Many proteases are involved in single-substrate reactions where an enzyme,  $E$ , binds reversibly to a substrate,  $S$ , via its active site and forms an enzyme-substrate complex,  $ES$ . The enzyme then releases the product,  $P$ , to regenerate the enzyme as shown below, where  $k_f$ ,  $k_r$ , and  $k_{cat}$  are rate constants. Changes to the relative concentrations of each species can be modelled as shown in Figure 1.6.

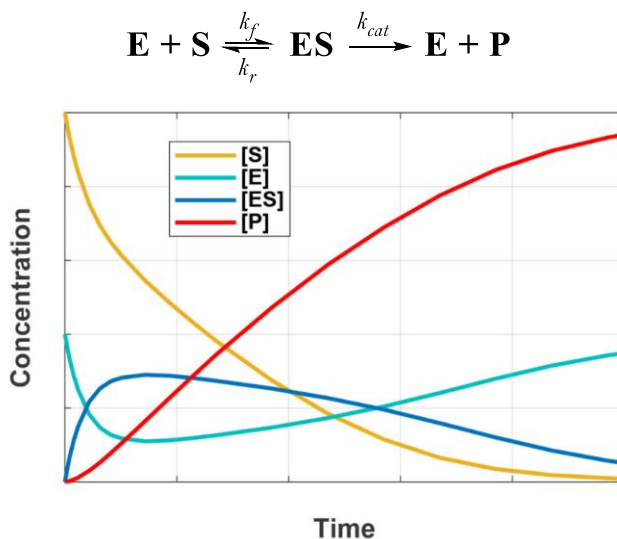


**Figure 1.6.** Changes in the relative concentrations of substrate  $S$ , enzyme  $E$ , enzyme-substrate complex  $ES$ , and product  $P$  in a single-substrate system.

The Michaelis-Menten model describes the initial rate of the product formation as shown in eqn. 15, where  $K_d$  is the dissociation constant,  $K_d = k_r/k_f$ . The classical model is often used for describing single-substrate enzyme kinetics where there is no cooperativity present. In addition, the Michaelis-Menten model contains several underlying assumptions: (i) the substrate and

enzyme quickly reach equilibrium to form substrate-enzyme complex, (ii) the substrate concentration is greater than about  $3 K_m$  (see below), (iii) the total enzyme concentration is constant, and therefore, the enzyme is not irreversibly inhibited or degraded, and (iv) the reaction is virtually non-reversible. Briggs and Haldane further developed the model to free the first assumption by applying steady-state approximation to a system where  $[E] \ll [S]$  [100]. Hence, the Michaelis-Menten kinetics is often described today as shown in eqn.16, where  $K_m = (k_r + k_{cat})/k_f$ .

$$V_0 = \frac{d[P]}{dt} = \frac{V_{\max} [S]}{K_d + [S]} \quad \text{Eqn. 15}$$

$$V_0 = \frac{d[P]}{dt} = \frac{V_{\max} [S]}{K_m + [S]} \quad \text{Eqn. 16}$$

Although the Michaelis-Menten model provides a useful framework for studying enzyme activities, the limitations, as a result of the underlying assumptions of the model, become significant as systems move away from the ideal Michaelis-Menten conditions and the species are no longer freely diffusing in solution. Particularly, in studying the design of QD enzyme probes, where substrates are immobilized onto the probe surface, the concentrations of the substrate are often too low to satisfy the restraint  $[S] > 3 K_m$ . For polyvalent substrate-conjugated QDs, higher concentrations than the typical low micromolar concentrations of QDs are needed to achieve a final concentration of substrates in the high micromolar to millimolar range that is common for  $K_m$ . At such high concentrations, not only does the noise from the background become more intense, but small changes in the PL intensities become more difficult to resolve. In addition, the colloidal stability of QDs may be compromised under such conditions. An alternative format is to measure the proteolytic rate in an excess enzyme for a given substrate concentration, where the enzyme kinetics can be analyzed using the relationship described in eqn. 17 [101,102].

$$V_0 = \frac{d[P]}{dt} = \frac{V_{\max} [E]}{K_m + [E]} \quad \text{Eqn. 17}$$

Another method of studying the enzyme kinetics includes the use of full progress curves of the enzyme digestion instead of monitoring the initial rate only. The data can be analyzed using the time-integrated version of Michaelis-Menten equation (eqn. 18), where  $k_{cat}$  is the catalytic rate,  $t$  is

time,  $E$  and  $P$  the concentrations of enzyme and product, respectively, and  $S_0$  the initial concentration of the substrate. This equation allows the determination of the  $k_{cat}/K_m$  ratio even when the concentration of the substrate does not satisfy the condition of  $[S] > 3 K_m$  [32,101,103].

$$k_{cat} \times [E]t = [P] + K_m \times \ln\left(\frac{[S_0]}{[S_0] - [P]}\right) \quad \text{Eqn. 18}$$

Alternatively, the progress curves can also be empirically modelled as biexponential decay functions (eqn. 19), where  $I$  is the signal intensity,  $k_i$  the empirical rate of the product generation with amplitude  $A_i$ , and  $I_\infty$  the residual value of  $I$ . A weighted average rate constant of the enzyme activity,  $k$ , can then be calculated using eqn. 20 [104–106].

$$I = A_1 e^{-k_1 t} + A_2 e^{-k_2 t} + I_\infty \quad \text{Eqn. 19}$$

$$k = \frac{|k_1 A_1 + k_2 A_2|}{A_1 + A_2} \quad \text{Eqn. 20}$$

## Chapter 2 : Synthesis & Characterization of Small Molecule Ligands

### 2.1 Introduction

QDs are traditionally and commonly synthesized with hydrophobic native ligands. Hence, ligand exchange with hydrophilic ligands is required post-synthesis to impart colloidal stability in aqueous environments which is often needed for biological applications. In addition, ligands can introduce different functional groups for surface modification and (bio)conjugation. More importantly, ligands are at the interface of QDs and their environment, so they can also determine the interactions between the nanocrystals and their surroundings, whether solvent or other molecules in solution. This chapter focuses on the synthesis of QD ligands and the characterization of different ligand-coated QDs. Enzyme assays were also used to study the interactions of different proteases and QD coatings. The aim was not only to expand the ligand library, but also to help design superior QD sensing systems in the future.

### 2.2 Experimental Methods

#### 2.2.1 Materials

L-glutathione reduced (GSH), tetramethylammonium hydroxide (TMAH) solution in methanol (25% w/v), ethylenediamine ( $\geq 99.5\%$ ), 1,3-propanesultone (98%),  $\beta$ -propiolactone ( $\geq 90\%$ ), sodium chloroacetate (98%), *N*-hydroxysuccinimide (98%), *N,N*-dimethylethylenediamine (95%),  $\delta$ -gluconolactone, *N,N'*-diisopropylcarbodiimide (98%), 1,3-aminopropylimidazole ( $\geq 97\%$ ), sodium borohydride ( $\geq 98\%$ ), lipoic acid (LA,  $\geq 99\%$ ), L-cysteine (97%), trypsin from bovine pancreas, and Amberchrom® CG300 were from Sigma-Aldrich (Oakville, ON, Canada).

Sodium bicarbonate (ACS grade), anhydrous potassium carbonate (ACS grade), sodium tetraborate decahydrate ( $\geq 99.5\%$ ), and anhydrous citric acid ( $\geq 99.5\%$ ) were from Amresco (Dallas, TX, USA). Decolourizing carbon, sodium phosphate dibasic heptahydrate ( $\geq 98\%$ ), triethylamine (reagent grade), chloroform (ACS grade), methanol (ACS grade), tetrahydrofuran (99.9%), glacial acetic acid, Alexa Fluor 680 C2 maleimide, ethylenediaminetetraacetic acid disodium salt dihydrate (EDTA- $\text{Na}_2$ ), and L-serine (99%) were from Fisher Scientific (Ottawa, ON, Canada).

Ni-NTA agarose was from Qiagen (Hilden, Germany). Peptide was from Bio-Synthesis Inc. (Lewisville, TX, USA) and the peptide sequence is shown in Table 2.1.

**Table 2.1.** Peptide sequence used for assays with thrombin, trypsin, and papain.

Peptide sequence (N-terminus to C-terminus) <sup>a</sup>	MW	Abbreviation
H <sub>6</sub> SP <sub>5</sub> GSDGNESGLVPR↓GSGC	3.0 kDa	Sub

<sup>a</sup> Substrate cleavage P1 site is bolded and denoted with a downward arrow.

CdSe/CdS/ZnS core/shell/shell QD with peak PL at 604 nm (QD604) was synthesized by a collaborator using a previously reported method [107,108]. Lyophilized papain was from Worthington Biochemical Corp. (Lakewood, NJ, USA). Human alpha-thrombin prepared in 50% glycerol/water (v/v) was from Haematologic Technologies, Inc. (Essex Junction, VT, USA).

### 2.2.2 Instruments

NMR spectra were acquired with a Bruker Avance III HD 400 MHz and Bruker Avance 300 MHz spectrometers (Bruker, Billerica, MA, USA). Electrospray ionization (ESI) mass spectra were obtained using a Waters ZQ mass spectrometer (Milford, MA, USA).

Dynamic light scattering (DLS) was performed on NanoBrook Omni from Brookhaven Instruments Inc. (Long Island, NY, USA).

Agarose gels were imaged with Gel Doc XR+ System (Bio-Rad Laboratories Inc., Hercules, CA, USA).

### 2.2.3 Synthesis of QD Ligands

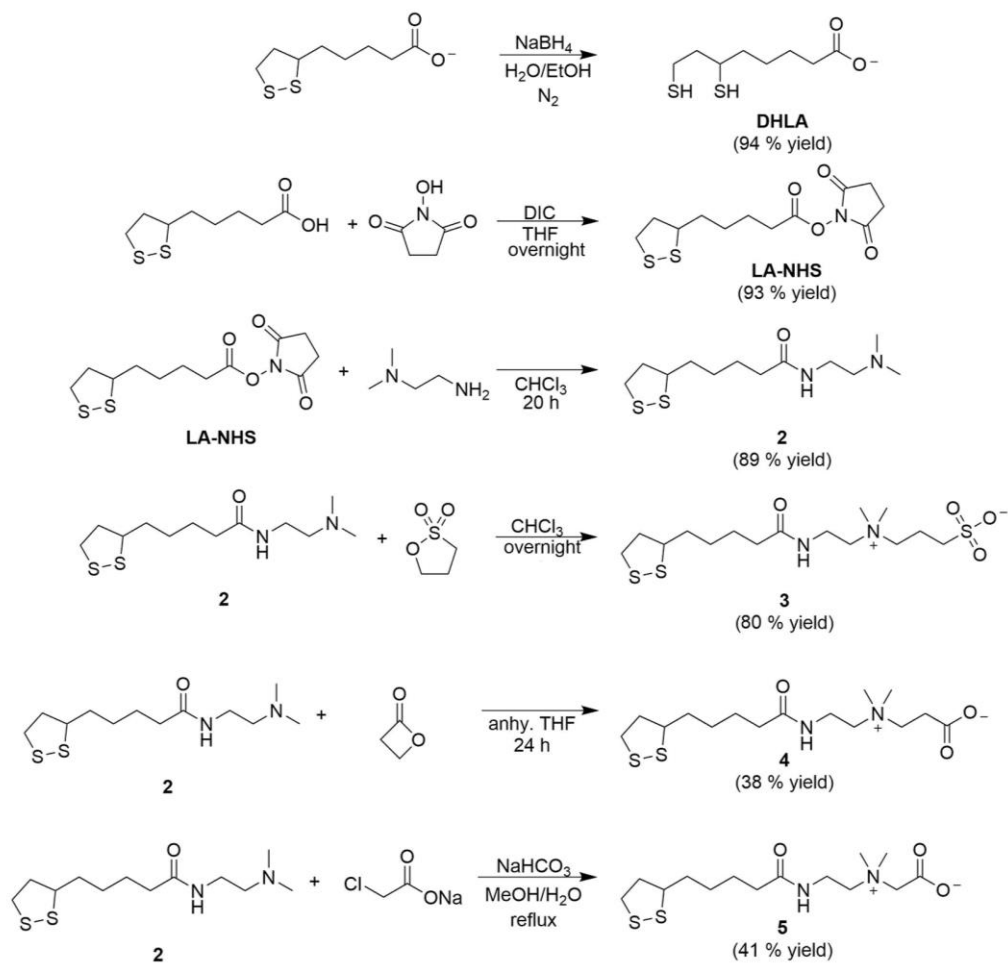
#### Dihydrolipoic acid (DHLA)

Lipoic acid (2.1 g, 10 mmol) was dissolved in 80 mL of a H<sub>2</sub>O/EtOH (1:1 v/v) mixture. Sodium borohydride (2.0 g, 53 mmol) was added to the solution portion-wise, and the reaction was stirred under nitrogen for 1 h. The solution was then heated in a water bath at 40°C for an additional 2 h.

After the reaction had cooled to room temperature, it was diluted with 50 mL of H<sub>2</sub>O and 12 M HCl (aq) was used to quench the excess sodium borohydride until the pH reached 2–3. The mixture was extracted three times with 50 mL DCM. The organic layers were combined, dried over Na<sub>2</sub>SO<sub>4</sub>, and the solvents were evaporated by a rotary evaporator and then under vacuum to give a clear oil (2.0 g, 94% yield). The product was stored in –20°C under nitrogen and was stable over several months. <sup>1</sup>H NMR (CDCl<sub>3</sub>, 400 MHz): δ 10.98 (br, s, 1H), 2.94–2.86 (m, 1H), 2.76–2.60 (m, 2H), 2.37–2.33 (m, 2H), 1.92–1.84 (m, 1H), 1.77–1.40 (m, 7H), 1.36–1.28 (m, 2H). <sup>13</sup>C NMR (CDCl<sub>3</sub>, 100 MHz): δ 180.2, 42.8, 39.3, 38.7, 34.0, 26.5, 24.3, 22.4.

#### 2,5-dioxopyrrolidin-1-yl 5-(1,2-dithiolan-3-yl)pentanoate (**LA-NHS**)

Lipoic acid (4.0 g, 19 mmol) and *N*-hydroxysuccinimide (2.9 g, 25 mmol) were dissolved in 25 mL of THF. *N,N'*-Diisopropylcarbodiimide (3.6 mL, 23 mmol) was first diluted with 5 mL of THF, then subsequently added dropwise to the reaction mixture. The reaction was stirred overnight at room temperature. A side-product, diisopropylurea, precipitated out of the solution over the course of the reaction and was removed by filtration. The filtrate was concentrated by rotary evaporation and the crude product was recrystallized with *i*-PrOH. The product was obtained as a yellow solid (5.5 g, 93% yield). <sup>1</sup>H NMR (CDCl<sub>3</sub>, 400 MHz): δ 3.5–3.62 (m, 1H), 3.09–3.22 (m, 2H), 2.84 (s, 4H), 2.63 (t, 2H), 2.44–2.51 (m, 1H), 1.89–1.97 (m, 1H), 1.69–1.83 (m, 4H), 1.48–1.61 (m, 2H). <sup>13</sup>C NMR CDCl<sub>3</sub>, 100 MHz): δ 169.3, 168.5, 67.1, 56.2, 40.3, 38.6, 34.5, 30.9, 28.4, 25.7, 24.5. ESI-TOF MS (pos, *m/z*): calcd for C<sub>12</sub>H<sub>17</sub>NO<sub>4</sub>S<sub>2</sub>Na 326.05, found 326.0 [M + Na]<sup>+</sup>.



**Scheme 1.** Synthesis of DHLA, LA-NHS, compounds 2, 3, 4, and 5.

*N*-(2-(dimethylamino)ethyl)-5-(1,2-dithiolan-3-yl)pentanamide (**2**)

LA-NHS (3.0 g, 10 mmol) was dissolved in 50 mL of chloroform. *N,N*-dimethylethylenediamine (2.0 mL, 18 mmol) was added into the LA-NHS solution dropwise. The reaction was stirred at room temperature overnight. To work-up the reaction, the crude product was first diluted with 30 mL of chloroform, followed by three washings with brine. The aqueous were combined and back-extracted with additional chloroform. The combined organic layers were dried over  $\text{Na}_2\text{SO}_4$  and the solvent was evaporated by a rotary evaporator to give a yellow oil (2.4 g, 89% yield). Because the product is unstable and has a tendency to crosslink when stored neat, the product should be used as is immediately after synthesis or stored as a diluted solution in chloroform.  $^1\text{H}$  NMR

(CDCl<sub>3</sub>, 400 MHz):  $\delta$  6.02 (br, s, 1H), 3.56 (m, 1H), 3.32 (q, 2H), 3.07–3.20 (m, 2H), 2.38–2.49 (m, 3H), 2.16–2.22 (m, 8H), 1.86–1.94 (m, 1H), 1.62–1.72 (m, 4H), 1.39–1.50 (m, 2H). <sup>13</sup>C NMR (CDCl<sub>3</sub>, 100 MHz):  $\delta$  172.9, 57.9, 56.6, 45.3, 40.4, 38.6, 36.8, 36.5, 34.8, 29.1, 25.6. ESI-TOF MS (pos; *m/z*): calcd for C<sub>12</sub>H<sub>25</sub>N<sub>2</sub>OS<sub>2</sub> 277.14, found 277.3 [M + H]<sup>+</sup>.

### *N*-(2-(5-(1,2-dithiolan-3-yl)pentanamido)ethyl)-*N,N*-dimethyl-3-sulfopropan-1-aminium (**3**)

Compound **2** (~6.4 g, ~23 mmol) was used immediately after synthesis and was dissolved in 40 mL of anhydrous chloroform. 1,3-propanesultone (8.5 g, 70 mmol) was dissolved in 10 mL of anhydrous chloroform and added to the solution. The reaction was stirred for 24 h at room temperature. The crude product, which precipitated from the solution, was isolated by vacuum filtration. The precipitate was washed with chloroform and dried under vacuum. The product was obtained as a chalky yellow solid (7.4 g, 80% yield over two steps). <sup>1</sup>H NMR (D<sub>2</sub>O, 400 MHz):  $\delta$  3.68–3.74 (m, 3H), 3.48–3.56 (m, 4H), 3.18–3.27 (m, 8H), 2.98–3.01 (t, 2H), 2.46–2.54 (m, 1H), 2.23–2.32 (m, 4H), 1.97–2.05 (m, 1H), 1.59–1.81 (m, 4H), 1.39–1.46 (m, 2H). <sup>1</sup>H NMR (DMSO-*d*<sub>6</sub>, 400 MHz):  $\delta$  8.15 (s, 1H), 3.61 (t, 1H), 3.45 (m, 4H), 3.33 (m, 3H), 3.22–3.08 (m, 2H), 3.05 (s, 6H), 2.48–2.39 (m, 2H), 2.11 (t, 2H), 1.98 (m, 2H), 1.87 (m, 1H), 1.68–1.64 (m, 1H), 1.52 (m, 3H), 1.36–1.34 (m, 2H). <sup>13</sup>C NMR (D<sub>2</sub>O, 100 MHz):  $\delta$  177.4, 62.9, 61.8, 56.6, 51.0, 47.2, 40.3, 38.1, 35.3, 33.7, 33.1, 27.9, 24.8, 18.3. ESI-TOF MS (pos, *m/z*): calcd for C<sub>15</sub>H<sub>31</sub>N<sub>2</sub>O<sub>4</sub>S<sub>3</sub> 399.14, found 399.1 [M + H]<sup>+</sup>.

### 3-((2-(5-(1,2-dithiolan-3-yl)pentanamido)ethyl)dimethylammonio)propanoate (**4**)

Compound **2** (0.90 g, 3.3 mmol) was dissolved in 15 mL of anhydrous THF. Beta-propiolactone (0.25 mL, 4.0 mmol) was added drop-wise to the solution. The mixture was stirred for 24 h and the product, which precipitated out of solution, was isolated by vacuum filtration, washed with chloroform, and dried under vacuum. The product was obtained as a yellow powder (0.44 g, 38% yield). <sup>1</sup>H NMR (D<sub>2</sub>O, 400 MHz):  $\delta$  3.71–3.67 (m, 3H), 3.62 (t, 2H), 3.48–3.45 (m, 2H), 3.28–3.18 (m, 2H), 3.14 (s, 6H), 2.7 (t, 2H), 2.54–2.46 (m, 1H), 2.29 (t, 2H), 2.04–1.96 (m, 1H), 1.78–1.72 (m, 1H), 1.68–1.59 (m, 3H), 1.46–1.39 (m, 2H). <sup>13</sup>C NMR (D<sub>2</sub>O, 100 MHz):  $\delta$  177.2, 176.2, 61.8, 56.5, 50.9, 40.3, 38.1, 35.3, 33.7, 33.1, 30.7, 27.9, 24.8. ESI-TOF MS (pos, *m/z*): calcd for C<sub>15</sub>H<sub>29</sub>N<sub>2</sub>O<sub>3</sub>S<sub>2</sub> 349.16, found 349.1 [M + H]<sup>+</sup>.

2-((2-(5-(1,2-dithiolan-3-yl)pentanamido)ethyl)dimethylammonio)acetate (**5**)

Compound **2** (1.3 g, 4.7 mmol) was dissolved in 10 mL MeOH. In another flask, sodium chloroacetate (1.1 g, 9.4 mmol) was dissolved in 10 mL water and combined with 10 mL of saturated sodium bicarbonate solution. The aqueous solution was added to the solution of compound **2** and let refluxed while lightly sealed with a septum. Two equivalents of sodium chloroacetate and 5 mL of saturated sodium bicarbonate was added every hour and the reaction was monitored by ESI-MS. The reaction was finished after roughly a total of 4 equivalents of sodium chloroacetate was added. After the reaction was let cooled, 3 M HCl (aq) was used to quench the reaction and the solvents were evaporated with a rotary evaporator. The crude product was then loaded onto a C18 column with methanol, while leaving behind any insoluble salt. The column was flushed with 150 mL of 20% MeOH (aq) in water and the product was eluted with 60% MeOH (aq). The combined fractions were then removed of solvents using a rotary evaporator and then further dried under vacuum. Alternatively, the crude can be dissolved in THF and filtered to remove the salts and side products to achieve good purity. The combined organic layers were then dried under a rotary evaporator and then under vacuum. The product was obtained as a yellow oil (0.65g, 41% yield). <sup>1</sup>H NMR (D<sub>2</sub>O, 400 MHz): δ 4.06 (s, 2H), 3.76 (t, 2H), 3.68 (t, 2H), 3.31, (s, 3H), 3.30 (s, 3H), 3.27–3.16 (m, 1H), 2.90 (s, 2H), 2.54–2.46 (m, 1 H), 2.28 (t, 2H), 2.09–1.96 (m, 1H), 1.8–1.14 (m, 6H). <sup>13</sup>C NMR (D<sub>2</sub>O, 100 MHz): δ 177.1, 168.6, 64.0, 61.8, 56.5, 51.8, 40.3, 38.2, 35.4, 33.7, 33.4, 28.0, 24.8. ESI-TOF MS (pos, *m/z*): calcd for C<sub>14</sub>H<sub>27</sub>N<sub>2</sub>O<sub>3</sub>S<sub>2</sub> 335.15, found 335.2 [M + H]<sup>+</sup>.

N-(2-aminoethyl)-2,3,4,5,6-pentahydroxyhexanamide (**6**)

Ethylenediamine (1.5 mL, 28 mmol) was diluted with 10 mL MeOH. In a separate flask, gluconolactone (1.0 g, 5.6 mmol) was dissolved in 90 mL of MeOH with heat. The solution of gluconolactone was added to the stirring ethylenediamine solution using an additional funnel. During the addition, the reaction was heated to reflux and let stirred for 3 h. After the reaction had cooled to room temperature, the solvent was removed by rotary evaporation. The liquid mixture of ethylenediamine and product was diluted with 5 mL of MeOH and about 100 mL of *i*-PrOH was added to precipitate the product. The precipitate was isolated by vacuum filtration and washed with three portions of 100 mL *i*-PrOH to obtain the product as a white powder (0.71 g, 53% yield). <sup>1</sup>H NMR (D<sub>2</sub>O, 400 MHz): δ 4.32 (s, 1H), 4.08 (s, 1H), 3.81 (d, 1H), 3.74, (s, 2H), 3.65

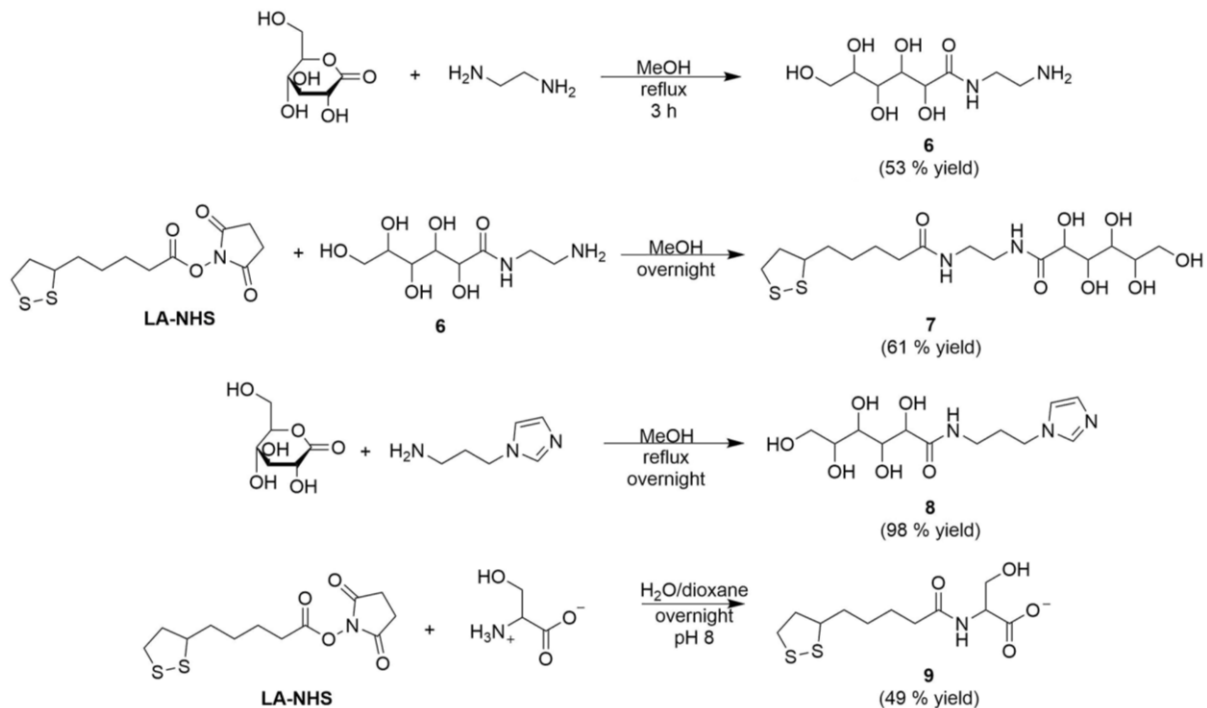
(d, 1H), 3.32–3.33 (m, 2H), 2.76 (m, 2H).  $^{13}\text{C}$  NMR ( $\text{D}_2\text{O}$ , 100 MHz):  $\delta$  174.3, 73.4, 72.1, 71.0, 70.3, 62.5, 41.1, 39.7. ESI-TOF MS (pos,  $m/z$ ): calcd for  $\text{C}_8\text{H}_{19}\text{N}_2\text{O}_6$  239.12, found 239.2  $[\text{M} + \text{H}]^+$ .

*N*-(2-(5-(1,2-dithiolan-3-yl)pentanamido)ethyl)-2,3,4,5,6-pentahydroxyhexanamide (**7**)

*N*-(2-aminoethyl)-2,3,4,5,6-pentahydroxyhexanamide (0.30 g, 1.3 mmol) was dissolved in 100 mL MeOH. LA-NHS (0.46 g, 1.5 mmol) was added to the solution, which was then sonicated to help with dissolution. The yellow reaction mixture was let stirred overnight at room temperature. After reducing the solvent level to a ~10 mL via rotary evaporation, the product that precipitated out of the solution was obtained by vacuum filtration. The solid was washed with a 1:1 mixture of MeOH/acetone and dried under vacuum to obtain an off-white solid (0.25 g, 46% yield).  $^1\text{H}$  NMR ( $\text{D}_2\text{O}$ , 400 MHz):  $\delta$  4.31 (s, 1H), 4.08 (s, 1H), 3.83–3.64 (m, 5H), 3.42–3.36 (m, 4H), 3.28–3.16 (m, 2H), 2.53–2.46 (m, 1H), 2.27–2.24 (m, 2H), 2.04–1.95 (m, 1H), 1.80–1.71 (m, 1H), 1.68–1.61 (m, 3H), 1.45–1.40 (m, 2H).  $^{13}\text{C}$  NMR ( $\text{D}_2\text{O}$ , 100 MHz):  $\delta$  177.3, 174.6, 73.3, 72.1, 71.1, 70.3, 62.6, 56.5, 40.2, 38.6, 38.4, 38.0, 35.5, 33.7, 27.8, 24.9. ESI-TOF MS (pos/neg,  $m/z$ ): calcd for  $\text{C}_{16}\text{H}_{31}\text{N}_2\text{O}_7\text{S}_2$  427.16,  $\text{C}_{16}\text{H}_{29}\text{N}_2\text{O}_7\text{S}_2$  425.14, found 427.0  $[\text{M} + \text{H}]^+$ , 425.0  $[\text{M} - \text{H}]^-$ .

*N*-(3-(1H-imidazol-1-yl)propyl)-2,3,4,5,6-pentahydroxyhexanamide (**8**)

3-aminopropylimidazole (1.6 mL, 13 mmol) was dissolved in 50 mL MeOH. Gluconolactone (2.0 g, 11 mmol) was added to the solution to form a white suspension. The reaction was refluxed overnight and the volume of the mixture was reduced to ~10 mL with a rotary evaporator. The product was precipitated out of solution with 100 mL of *i*-PrOH, collected via vacuum filtration, washed with three portions of 20 mL *i*-PrOH, and dried under vacuum. The product was obtained as a white solid (3.4 g, 98% yield).  $^1\text{H}$  NMR ( $\text{D}_2\text{O}$ , 400 MHz):  $\delta$  7.68 (s, 1H), 7.17 (s, 1H), 7.02 (s, 1H), 4.29 (s, 1H), 4.07 (m, 3 H), 3.82 (d, 1H), 3.75 (s, 2H), 3.66 (d, 1H), 3.23 (t, 2H), 2.04 (q, 2H).  $^{13}\text{C}$  NMR ( $\text{D}_2\text{O}$ , 100 MHz):  $\delta$  174.4, 138.0, 127.8, 120.1, 73.4, 72.2, 71.0, 70.3, 62.5, 44.2, 36.0, 29.6. ESI-TOF MS (pos,  $m/z$ ): calcd for  $\text{C}_{12}\text{H}_{22}\text{N}_3\text{O}_6$  304.15, found 304.1  $[\text{M} + \text{H}]^+$



**Scheme 2.** Synthetic schemes of compounds 5, 6, 7, 8, and 9.

(5-(1,2-dithiolan-3-yl)pentanoyl)serine (**9**)

L-Serine (104 mg, 0.99 mmol) was dissolved in 3 mL borate buffer (50 mM, pH 8) and added to a solution of LA-NHS (200 mg, 0.66 mmol) in 5 mL dioxane. The solution was let stirred overnight at room temperature. The reaction was diluted with 40 mL of water and three portions of 40 mL  $\text{CHCl}_3$  was used to wash the aqueous layer, follow by the addition of 3 M HCl to acidify the solution until  $\text{pH} < 2$ . The product was then extracted with three portions of 40 mL EtOAc. The organic layers were combined, removed of solvents with a rotary evaporator, and dried under vacuum. The product was obtained as a yellow oil (49% yield)  $^1\text{H}$  NMR ( $\text{D}_2\text{O}$ , 400 MHz):  $\delta$  4.29 (s, 1 H), 3.79 (d, 2 H), 2.94-2.88 (m, 1 H), 2.74–2.60 (m, 2 H), 2.29 (t, 2 H), 1.94–1.85 (m, 1H), 1.76–1.44 (m, 8 H).  $^{13}\text{C}$  NMR ( $\text{CD}_3\text{OD}$ , 100 MHz):  $\delta$  175.7, 174.1, 62.9, 56.6, 43.0, 38.7, 38.6, 35.8, 26.4, 25.1, 21.4. ESI-TOF MS (neg,  $m/z$ ): calcd for  $\text{C}_{11}\text{H}_{18}\text{NO}_4\text{S}_2$  292.07, found 292.0  $[\text{M} - \text{H}]^-$ .

## 2.2.4 Ligand Exchange

**Table 2.2.** List of ligands and their abbreviations.

<b>Ligand</b>	<b>Ligand Abbreviation</b>
<b>Lipoic Acid</b>	DHLA
<b>Glutathione</b>	GSH
<b>3</b>	SB
<b>5</b>	CB
<b>7</b>	Glc
<b>9</b>	Ser
<b>8</b>	API-Glc

A list of the ligands used in this chapter and their abbreviations are summarized by Table 2.1. DHLA and GSH ligand exchange procedures are described in Chapter 3.2. The other ligands can be divided into two different methods of ligand exchange: LA-based ligands and imidazole-based ligands.

### **LA-based Ligands**

Ligand (0.10 mmol) was dissolved in 100  $\mu$ L water and a solution of NaBH<sub>4</sub> (8 mg, 0.21 mmol) in 100  $\mu$ L water was added portion-wise to the ligand solution. The microcentrifuge tube was vortexed and quickly opened to vent the evolving hydrogen gas. The reaction was left on the bench for ~10 min at room temperature before being quenched with acetone (200  $\mu$ L). Excess acetone (additional 600  $\mu$ L) was added to precipitate the ligands with centrifugation at 17000 rcf. If the ligand did not precipitate, as was often the case with CB, the reaction mixture was divided into two and acetone was added until the total volume of 1.2 mL was reached. Following centrifugation and the removal of the solvents, clear, viscous liquids were obtained for CB, SB, and Ser, whereas Glc was obtained as a white gel.

The ligands were dissolved in 100  $\mu\text{L}$  borate buffer (50 mM, pH 9.2) and a solution of QD604 (1.0 nmol) in 100  $\mu\text{L}$   $\text{CHCl}_3$  was added to the ligands solution. For CB, SB, and Ser, 200  $\mu\text{L}$  TMAH (25% w/v in methanol) was added. For Glc, 300  $\mu\text{L}$  TMAH (25% w/v in  $\text{H}_2\text{O}$ ) was added. All solutions were incubated at 55  $^\circ\text{C}$  overnight. The QDs were precipitated with acetone after incubation, at 17 000 rcf. Glc QDs were redispersed in water and washed with acetone a total of three times before being redispersed in ultra-pure water. CB, SB, and Ser were redispersed in borate buffer-NaCl (50 mM, pH 9.2, 250 mM NaCl) and washed with 1:1 MeOH/acetone mixture a total of three times before being redispersed in borate buffer (50 mM, pH 9.2). All QDs were stored at 4  $^\circ\text{C}$  following ligand exchange until needed. QDs were quantified using the molar extinction coefficient at the first exciton peak ( $\epsilon = 232\,268\text{ M}^{-1}\text{ cm}^{-1}$ ).

### **Imidazole-based Ligands**

Ligand (0.20 mmol) was dissolved in 150  $\mu\text{L}$  1 M NaOH and QD604 (1.0 nmol) in 200  $\mu\text{L}$   $\text{CHCl}_3$  was added to the solution in a microcentrifuge tube. After cycles of vortexing and centrifugation, the clear aqueous phase with the QDs was transferred to a new microcentrifuge tube and diluted with 500  $\mu\text{L}$  borate buffer (50 mM, pH 9.2). The QDs were stored at 4  $^\circ\text{C}$  and quantified using the molar extinction coefficient at the first exciton peak ( $\epsilon = 232\,268\text{ M}^{-1}\text{ cm}^{-1}$ ).

## **2.2.5 Characterization of QDs**

### **DLS measurements**

Dynamic light scattering (DLS), using a 633 nm laser light source, was used to estimate the hydrodynamic diameter of QDs. Samples in borate buffer (50 mM, pH 9.2) were passed through 0.22  $\mu\text{m}$  filters prior to the measurements and roughly 80  $\mu\text{L}$  of 1–5  $\mu\text{M}$  samples were used for measurements.

### **Ferguson analysis**

Ferguson analysis was used to characterize the zeta potentials of  $\text{QD}_X$ , where X is the ligand, using previously published protocols [109,110]. QDs were prepared by diluting the ligand-exchanged QD stock solutions to 150 nM and glycerol was added to achieve a final concentration of 4% (v/v) glycerin. A volume of 6  $\mu\text{L}$  of the prepared sample was loaded onto the gel. QDs were run through

agarose gels of various concentrations ranging from 0.7%–2% w/v at 7.33 V/cm for 20 min in  $1 \times$  TBE buffer (pH 8.3) and imaged with Gel Doc XR+ System. Each concentration was performed in triplicate.

### **Stability tests (Ionic strengths and pH)**

Ionic strength stability tests were carried out using 0.1 M, 1 M, 2 M, and 4 M NaCl in borate buffer (50 mM, pH 9.2). pH stability tests were conducted using phosphate-citrate buffer for pH 3–8 and carbonate buffer for pH 9–10.8. Samples were prepared by directly diluting QD stock solutions to a final concentration of 0.2  $\mu$ M and a final volume of 100  $\mu$ L. With a smartphone, images were taken weekly at five different time points up to 4 weeks. Before imaging, QD samples were centrifuged for a minute at 17 000 rcf to better visualize aggregated QDs. The samples were vortexed post-imaging to prevent any increase in localized QD concentration.

### **Quantum yield measurements**

QD<sub>x</sub> quantum yields were determined by measuring the absorbance and PL intensities of QD<sub>x</sub> and a standard dye at various concentrations. QD<sub>x</sub> stock solutions in borate buffer (50 mM, pH 9.2) of 100 nM were prepared, followed by serial dilutions to achieve final concentrations of 100 nM, 50 nM, 25 nM, 12.5 nM, 6.3 nM, 3.1 nM, and 1.6 nM. Similarly, a fluorescein stock solution of 0.1 mM in borate buffer (pH 9.2) was prepared and diluted to achieve final concentrations of 12.5  $\mu$ M, 6.3  $\mu$ M, 3.1  $\mu$ M, 1.6  $\mu$ M. A sample of borate buffer (pH 9.2) was used as a blank. Absorbances were measured at 464 nm. PL intensities were measured using an excitation wavelength of 464 nm and measured from 474–700 nm using 2 nm step size.

### **Spectral overlap and Förster distance of QD604-A680 pair**

Spectral overlap between QD604 and A680 was determined by measuring the absorbance spectra over the range of 450–850 nm. The PL spectrum for QD604 was measured between 450–850 nm with 2 nm step size using an excitation wavelength of 400 nm. PL spectrum for A680 was measured between 620–850 nm with 2 nm step size using an excitation wavelength of 590 nm. Both measurements were done using excitation light of a fixed bandwidth (5 nm).

## **2.2.6 Enzyme Assays with QD<sub>x</sub>**

Thrombin substrate, labelled with Alexa Fluor 680 or Sub(A680), was conjugated onto different ligand-coated QDs and assayed with thrombin, trypsin and papain. Details of the peptide labelling and the proteolytic assays are described in Chapter 3.2. Briefly, 8 eq. of Sub(A680) was mixed with QDs to reach a working solution concentration that is double the final concentration in the reaction. This mixture was incubated for a minimum of 30 min prior to the experiment. Enzyme stock solution was added to QD<sub>x</sub>-Sub(A680) in a 96-well microtiter plate (50  $\mu$ L total volume, 50 nM QD<sub>x</sub> and 400 nM Sub(A680) final concentrations). Immediately after the enzyme addition, the PL emissions from QD604 and A680 were monitored at 604 nm and 710 nm, respectively, and at 1 min intervals over 2 h. Experiments with thrombin and trypsin were in borate buffer (50 mM pH 9.2) and papain experiments were in PBS buffer (10 mM PO<sub>4</sub><sup>3-</sup>, 140 mM NaCl, 3 mM KCl; pH 7.2). Thrombin and trypsin were prepared as described in Chapter 3.2. Papain was prepared fresh and activated for at least an hour before the experiment. To activate papain, the powdered enzyme was dissolved in the activation solution (1.1 mM EDTA, 65  $\mu$ M mercaptoethanol, and 5.5 mM cysteine) and quantified using the molar absorptivity at 280 nm ( $\epsilon = 57\,600\text{ M}^{-1}\text{ cm}^{-1}$ ). Various concentrations of each enzyme were used for each set of experiments as summarized in Table 2.3. Each experiment was performed in triplicate.

**Table 2.3.** List of enzymes and concentrations.

<b>Enzyme</b>	<b>Concentration (nM)</b>
<b>Thrombin</b>	1.2 / 2.4 / 7.2 / 14.4
<b>Trypsin</b>	2 / 4 / 8 / 16
<b>Papain</b>	160 / 200 / 240 / 300

## 2.3 Data Analysis

Data analysis for the fitting of enzyme assays can be found in Chapter 3.3

### 2.3.1 Ferguson Analysis

The mobilities of QD<sub>x</sub> were extracted from the images using ImageJ software (National Institutes of Health, Bethesda, MD). Velocities measured in pixels/s were converted into SI units (m/s) and

divided by the field strength ( $\text{V m}^{-1}$ ) to give mobilities ( $\text{m}^2 \text{V}^{-1} \text{s}^{-1}$ ). The relationship between the logarithm of mobility,  $M$ , and the gel concentration,  $T$ , could be expressed as the following equation:

$$\log M = \log M_o - K_R T \quad \text{Eqn. 21}$$

The mobility of particles in solution,  $M_o$ , can then be used to estimate the zeta potentials  $\zeta$  using eqn. 22, where  $\epsilon_S$  is the dielectric constant of the solvent ( $\epsilon_{\text{H}_2\text{O}} = 78.3\epsilon$ , where  $\epsilon$  is the permittivity of the vacuum) and  $\eta_S$  is the solvent viscosity ( $\eta_{\text{H}_2\text{O}} = 0.89 \text{ cP} = 0.00089 \text{ N s m}^{-2}$ ).

$$\zeta = \frac{3M_o\eta_S}{2\epsilon_S} \quad \text{Eqn. 22}$$

### 2.3.2 Quantum Yield Measurements of QD<sub>X</sub>

Fluorescein has a known quantum yield of 0.93 in borate buffer at pH 9.5 [111]. Given eqn. 23, where the subscript  $R$  refers to the reference dye, the quantum yield of the sample can be calculated by experimentally determining the slope of the absorbance versus integrated PL intensities plot as shown in eqn. 24. QD PL intensities were integrated over 480–700 nm.

$$\frac{\Phi}{\Phi_R} = \frac{\int_0^{\square} I(\lambda) d\lambda}{\int_0^{\square} I_R(\lambda) d\lambda} \times \frac{1-10^{A_R}}{1-10^A} \times \frac{n^2}{n_R^2} \quad \text{Eqn. 23}$$

$$\Phi = \frac{\Phi_R \times \text{slope}}{\text{slope}_R} \quad \text{Eqn. 24}$$

### 2.3.3 Spectral Overlap and Förster Distance of QD604-A680 Pair

The absorbance and emission spectra were normalized such that the highest intensity for each spectrum has a value of one. The spectral overlap between QD604 and A680 was calculated to be  $1.1 \times 10^{-9} \text{ cm}^6 \text{ mol}^{-1}$ . Using eqn. 25, where the orientation factor  $\kappa^2$  is 2/3, refractive index  $n$  is 1.33, and  $\Phi$  the quantum yield of QD<sub>X</sub>, the Förster distances of various QD<sub>X</sub>-A680 pairs were determined.

$$R_0 = 3.09 \times 10^2 (\kappa^2 n^{-4} \Phi_D J(\lambda))^{1/6} \quad (\text{in nm}) \quad \text{Eqn. 25}$$

## 2.4 Results and Discussion

### 2.4.1 Design and Synthesis of QD Ligands

The development of the small molecule ligand library was based on the metal-binding affinity of the bidentate lipoic acid and monodentate imidazole groups appended to hydrophilic moieties that can impart QDs with colloidal stability after ligand exchange. A list of the ligands and their structures can be found in Figure 2.1. Carbodiimide coupling was used to activate the carboxylic acid group of lipoic acid to form a semi-stable, amine-reactive, succinimidyl-ester intermediate for the conjugation to various peripheral groups. A total of five lipoic acid derivatives and one imidazole derivative were synthesized. Lower yield for ligand **4** was likely associated with the reactive beta-propiolactone and insufficient drying of the solvent, whereas the synthesis of CB gave an excess of salt and chloroacetate which led to a loss of product during the long purification process. The synthesis of Ser involved NHS coupling between a hydrophobic lipoic acid and a hydrophilic amino acid which required a careful balance between the solubility of the two reactants. Hydrolysis of the NHS intermediate was a significant competing reaction when the nucleophilic serine concentration was low and was likely the leading cause of the loss of product.

The tertiary amine intermediate **2**, CB, and Ser are viscous liquids that tend to crosslink during storage. Therefore, these compounds should be stored as diluted solutions of known concentrations in chloroform (compound **2**) and water (CB and Ser) at 4°C until needed. Overall, the production of each derivative was achieved over 2–3 steps.

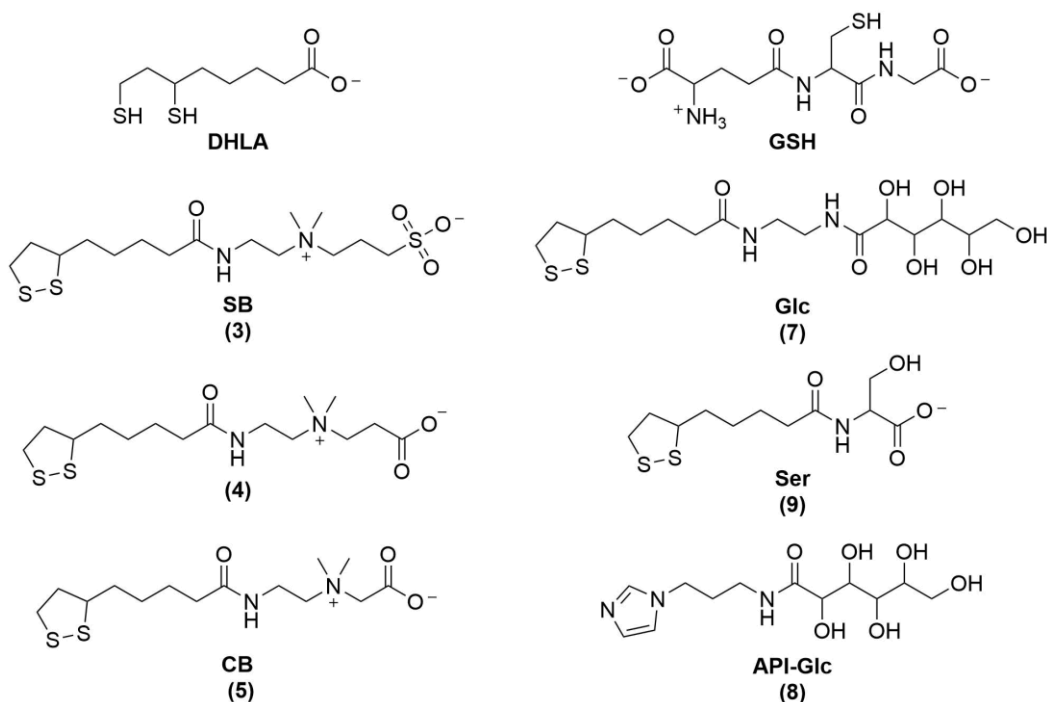


**Figure 2.1.** Structures of ligands used in this chapter. All but GSH was synthesized in this work.

## 2.4.2 Ligand Exchange

LA-based derivatives were ligand exchanged in a similar manner by first reducing the disulfide bond using sodium borohydride, followed by concurrent quenching of this reducing agent and precipitation of the ligands with acetone. Quenching with acetone was preferred over quenching with HCl (aq) followed by neutralization with NaOH (aq) because of the large amount of salt, as well as the dilution of the ligand, involved in the procedure. The precipitation of the ligand allowed for a higher ligand concentration during the ligand exchange which helped with the mass action-driven process.

Although ligands **4** and CB only differ in one carbon chain length, QDs coated with ligand **4** consistently had broader bands and streaked more than CB-coated QDs after agarose gel

electrophoresis. These observations indicate that the former ligand was associated with less aqueous stability or more interactions with the agarose gel medium. The poorer stability may be explained by the differences in the  $^{13}\text{C}$  NMR. The amide carbon of **4** is shifted downfield to 176 ppm compared to that of 169 ppm of CB suggesting that the amide experiences a greater deshielding effect. This is consistent with the finding in literature that additional methylene groups increase the dipole moment between the two charged centres in betaines and their pKa values also increase with increasing charge separation [112]. Thus, the decrease in QD stability associated with ligand **4** could stem from the decrease in the electrostatic stabilization. CB was chosen over **4** as a QD ligand and used for further characterization and experiments.

In contrast to the LA-based derivatives, imidazole-based ligands readily bind to the  $\text{Zn}^{2+}$  ions in the QD shell at basic pH. However, the binding of the monodentate imidazole moiety is weaker than that of the bidentate LA derivatives, as demonstrated by the streaking of QDs on the agarose gel. Instead of three washing steps following the ligand exchange, for imidazole-based ligand-coated QDs, the native, organic ligands were removed by discarding the organic layer of the biphasic ligand exchange reaction.

Typical recovery of QDs was 30–80% post ligand exchange. Most losses of the QDs were from incomplete precipitation as some of the  $\text{QD}_x$  remained in solution even in the presence of organic solvents and NaCl (aq).

### 2.4.3 Characterizations of $\text{QD}_x$

The hydrodynamic diameters of the different  $\text{QD}_x$  were very similar, between 12–14 nm. As expected, these hydrodynamic diameters were slightly larger than the geometric QD diameter of  $9.8 \pm 1.3$  nm measured from the TEM images (Figure 2.2). The differences between ligand structures may be too subtle to have a significant impact on the DLS measurements. A summary

of the QD<sub>X</sub> hydrodynamic diameters, zeta potentials ( $\zeta$ ), and quantum yield ( $\Phi$ ) can be found in Table 2.4.

**Table 2.4.** The hydrodynamic diameters, zeta potential ( $\zeta$ ), and quantum yield ( $\Phi$ ) of QD<sub>X</sub>, where X is the ligand.

QD <sub>X</sub>	Mode (nm)	Mean (nm)	$\zeta$ (mV)	$\Phi$
<b>GSH</b>	11.8 ± 0.3	14.4 ± 0.6	-58	0.29
<b>DHLA</b>	12.4 ± 0.2	16.2 ± 0.5	-60	0.08
<b>SB</b>	14.3 ± 0.1	15.9 ± 0.9	-37	0.14
<b>CB</b>	12.5 ± 0.1	15.4 ± 0.3	-35	0.14
<b>Glc</b>	13.9 ± 0.2	14.9 ± 0.4	-57	0.21
<b>Ser</b>	11.7 ± 0.8	12.3 ± 0.9	-60	0.12
<b>API-Glc</b>	12.2 ± 0.4	13.0 ± 0.6	-40	0.22

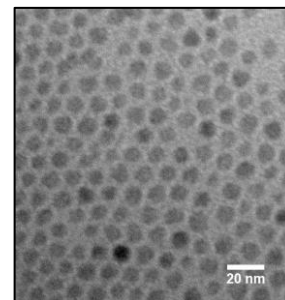


**Figure 2.2.** TEM image of CdSe/CdS/ZnS QD604. Scale bar is 20 nm. Courtesy of Eleonora Petryayeva.

Zeta potentials were determined via a Ferguson analysis. Representative images of different agarose concentrations and a Ferguson plot for QD<sub>X</sub> are shown in Figure 2.3. As shown in Table 2.3, the zeta potentials of QD<sub>GSH</sub> and QD<sub>DHLA</sub> were around -60 mV, whereas QD<sub>SB</sub> had a zeta potential of about -40 mV, which is consistent with our previous findings for another batch of QD with a peak PL at ~630 nm [113]. QD<sub>CB</sub> had virtually the same zeta potential as QD<sub>SB</sub>; whereas QD<sub>Ser</sub> had a similar value as QD<sub>DHLA</sub>, as one would anticipate based on their very similar structures. Glucose-appended ligands, Glc and API-Glc, both resulted in QDs with negative zeta potentials, despite their neutrally charged ligand structures. From literature, it appears that simple carbohydrates-coated QDs [114] and other nanoparticles [115] are associated with negative zeta potentials. This is likely from the high density of hydroxyl groups introduced by the carbohydrates that led to a more negative potential at the surface of the nanoparticle. A simplified criterion for electrostatic stabilization is that the absolute value of zeta potential must be greater than 30 mV for colloidal stability [116] and this criterion was satisfied by all of the QD<sub>X</sub> explored in this chapter.

The quantum yields of the QD<sub>X</sub> were determined using fluorescein as a standard. From visual inspection, QD<sub>GSH</sub> and QD<sub>Glc</sub> consistently had the most intense fluorescence and this was reflected

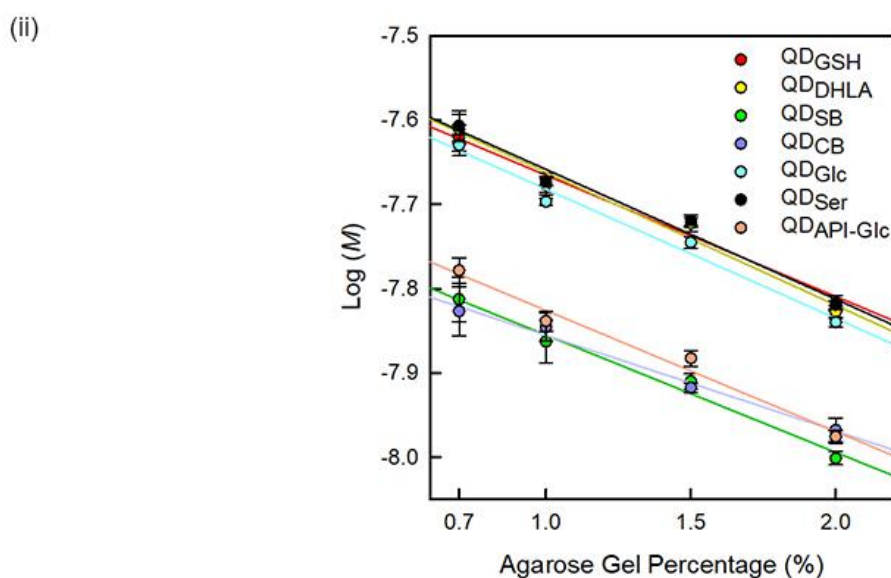
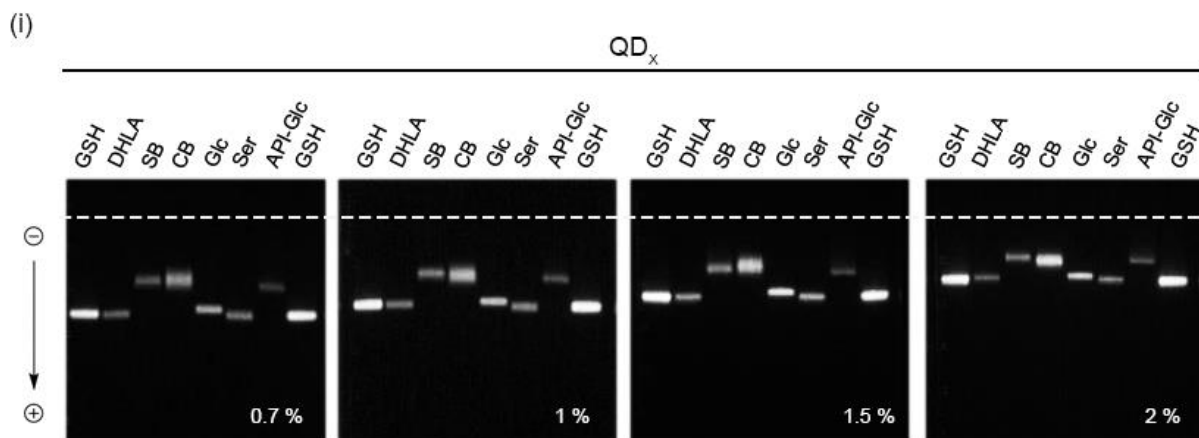


**Figure 2.3.** (i) Representative images of gel electrophoresis at various concentrations of agarose (w/v). (ii) Ferguson plots of  $QD_x$ , where X is the ligand.

by their quantum yields. It should be noted that although differences in quantum yields can be introduced during ligand exchange procedures,  $QD_{SB}$ ,  $QD_{CB}$ ,  $QD_{Glc}$ , and  $QD_{Ser}$  shared the same method of ligand exchange. In addition,  $QD_{API-Glc}$  would be expected to have similar quantum yield as the original organic QDs because its ligand exchange was a simple phase transfer without the addition of any heat or surfactant (i.e. TMAH). Therefore, the bright PL of  $QD_{GSH}$  and  $QD_{Glc}$  may be attributed to the inherent nature of the ligands and possibly additional surface passivation. In addition, the lower quantum yields associated with the dithiolate ligands, particularly DHLA,

may be attributed to the decrease in the surface electron trap and the introduction of new hole trap states associated with the high thiolate concentrations during the ligand exchange, as mentioned previously in Chapter 1 [37].

Ionic strength and pH stability tests with QD<sub>X</sub> over a period of 4 weeks were used to assess the colloidal stability of QDs in various environments. At pH 9 and 0.1, 1, 2, 4 M of NaCl (aq), most QDs were stable at least up to 4 weeks, with the exception of zwitterionic QDs and QD<sub>Glc</sub> (Figure A24–Figure A30). The zwitterionic QDs began to aggregate (indicated by an asterisk) as early as 7 days for QD<sub>SB</sub> and could be pelleted (indicated by a downward arrow) starting from 14 days after the preparation of the samples. Although QDs only pelleted at lower concentrations of NaCl (i.e. 0.1 and 1 M), they were also not stable at higher concentrations of NaCl (aq), as indicated by the aggregation and loss of fluorescence for QD<sub>SB</sub> and the sticking of the QDs to the side of the microcentrifuge tube for QD<sub>CB</sub>. It is possible that the aggregated QDs formed at higher ionic strengths were more colloidally stable than at lower ionic strengths (< 2 M NaCl ) and the aggregates were not large enough to be pelleted by one minute of centrifugation at 17 000 rcf. QD<sub>Glc</sub> also showed signs of aggregation and began to stick to the wall of the microcentrifuge tube beginning from day 14, but the QDs did not aggregate to a degree that could be pelleted out of the solution.

In terms of pH stability, QD<sub>Glc</sub> had superior performance and was stable across pH 4–11 over 28 days, whereas QD<sub>DHLA</sub> and QD<sub>API-Glc</sub> was only stable from pH 8–11 for the same period of time. QD<sub>GSH</sub> also showed good stability across pH 6–11 over 28 days. The zwitterionic QDs, however, began to aggregate at pH 3–5 and pH 9–10 around 14 days. These observations are consistent with their smaller zeta potentials and therefore less electrostatic stabilizations. In particular, QD<sub>CB</sub> appeared to be less stable than QD<sub>SB</sub> and it is likely because of the higher pK<sub>a</sub> of the carboxylate group (pK<sub>a</sub> ≈ 4) compared to that of the sulfonate (pK<sub>a</sub> ≈ -2). The poor stability of QD<sub>API-Glc</sub> is consistent with the coordination of the imidazole groups. At pH lower than 8, they would be protonated and unable to form dative bonds with the Zn<sup>2+</sup> ions in the QD shell. It is also worth noting that for all the QDs but QD<sub>API-Glc</sub> fluorescence was retained even at pH 3 despite aggregation. This suggests that API-Glc provided the least stabilization at low pH (< 4) and that the QD core was prone to etching by the acid in solution.

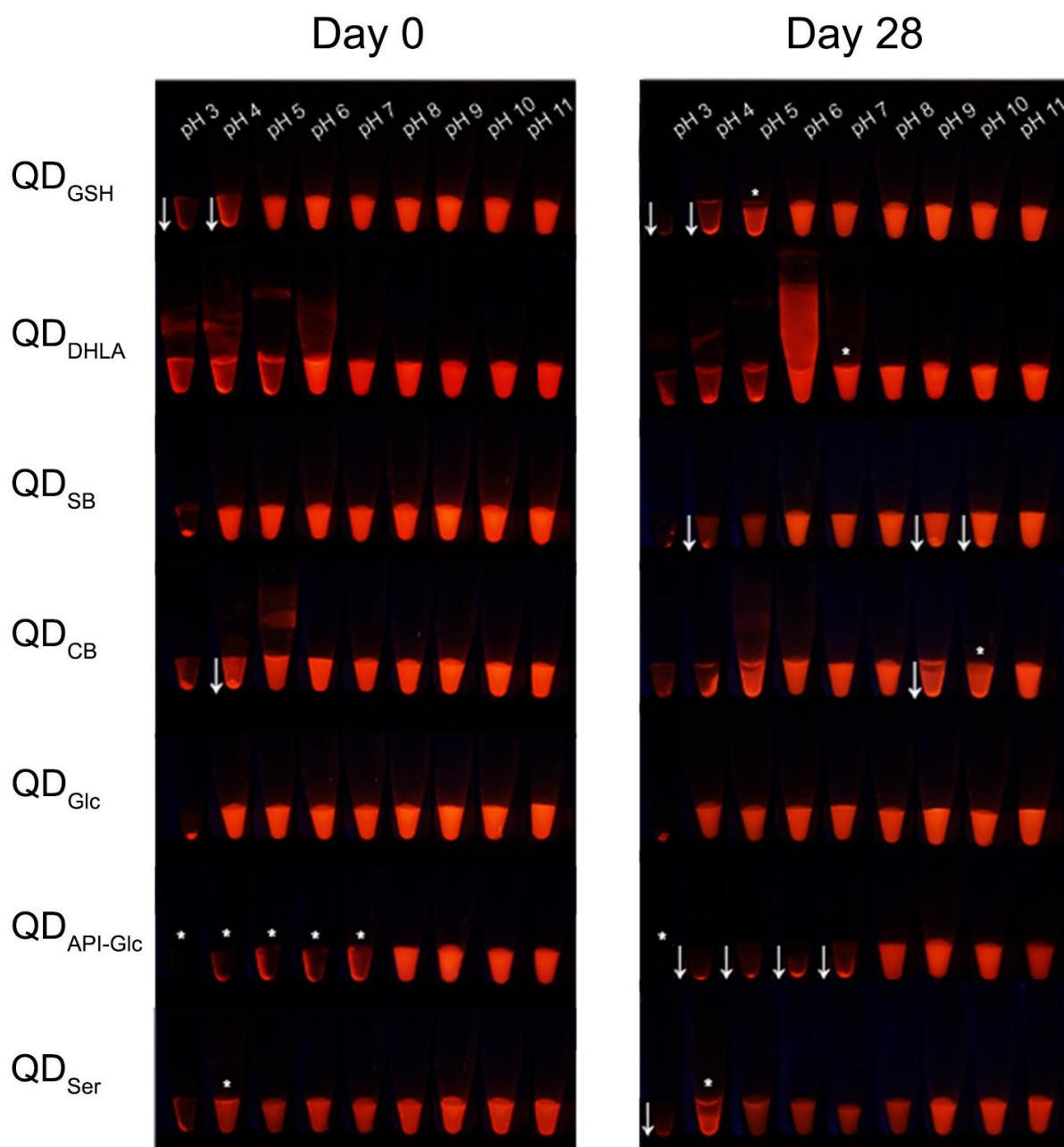


**Figure 2.4.** pH stability tests of QD<sub>x</sub> over four weeks. For clarity, asterisks and arrows are used to indicate aggregation and precipitation, respectively.

Some limitations of these stability tests include a lack of quantitative monitoring of the QD sizes throughout the experiment and that some QD aggregates were not large enough to be pelleted by centrifugation. It is possible that better visualization could be achieved by longer periods of

centrifugation. However, different degrees of aggregation would require different lengths of centrifuging time and the reproducibility of the experiment would suffer. Further complications arose when QDs did not pellet nor stick to the wall of the microcentrifuge tube (e.g. QD<sub>GSH</sub> pH 5, day 28). Finally, the images taken with smartphone was subject to differences in the PL intensity of the QD and the smartphone camera. Possible future work includes monitoring with DLS, but it is a very low throughput method. Although the stability test results are subjective and qualitative, careful interpretation of the results can still allow us to compare the relative stability of QD<sub>X</sub>.

## 2.5 Enzyme Assays with QD<sub>X</sub>

### 2.5.1 QD-A680 FRET Pair

QD604 and A680 have a significant spectral overlap between the donor emission and acceptor absorption and minimal direct excitation of the acceptor dye at 400 nm. The pair also have sufficient spectral separation to resolve the emissions from both fluorophores (Figure 2.5). The spectral overlap between QD604 and A680 was determined to be  $J = 2.2 \times 10^{-9} \text{ cm}^6 \text{ mol}^{-1}$  and the Förster distances for the various QD<sub>X</sub>-A680 pairs are summarized by Table 2.5.

**Table 2.5.** Förster distances between QD<sub>X</sub> and A680.

QD <sub>X</sub>	$\Phi$	R <sub>0</sub> (nm)
GSH	0.29	6.5
DHLA	0.08	5.3
SB	0.14	5.8
CB	0.14	5.8
Glc	0.21	6.2
Ser	0.12	5.7
API-Glc	0.22	6.2

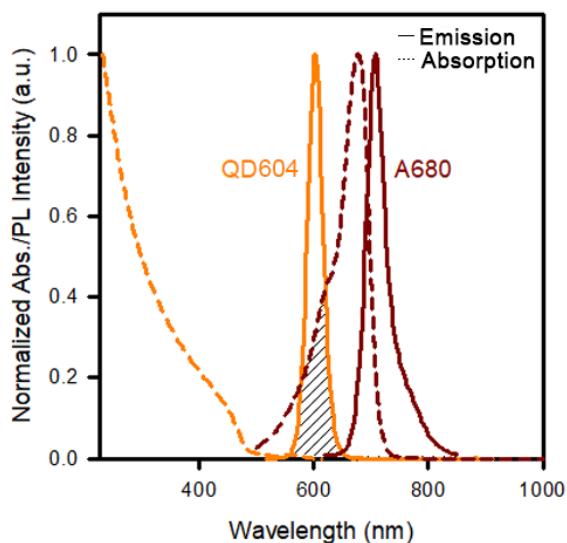


**Figure 2.5.** Normalized absorption and PL emission spectra of QD604 and A680. Spectral overlap between the QD604 emission and A680 absorption is shown as the shaded area.

### 2.5.2 Assays with Thrombin, Trypsin, and Papain

Enzyme assays with QD<sub>X</sub>-Sub(A680)<sub>8</sub> were carried out with three widely available and well-studied enzymes to assess any differences in proteolytic activity as a result of the different surface chemistry. QD<sub>API-Glc</sub> was not used in these experiments because of the weaker binding afforded by the imidazole groups compared to the dithiolate ligands. The summarized progress curves as well as representative progress curves of QD<sub>GSH</sub> are shown in Figure 2.6. It can be seen from the summary progress curves that QD<sub>DHLA</sub>, QD<sub>GSH</sub>, and QD<sub>Glc</sub> had the lowest PL ratio end-points across the various enzymes, suggesting that they were associated with the least non-specific adsorption of the hydrolyzed dye-labelled products. The zwitterionic ligands, CB and SB, were associated with higher PL ratio end-points and showed a drastic change in activity with thrombin. The zwitterionic QDs had zeta potentials of  $-37$  mV and  $-35$  mV compared to around  $-60$  mV of other QDs, it is possible that the higher end-points could stem from the adsorption of the hydrolyzed dye-labeled products because of the lower electrostatic repulsion. As shown by the progress curves of QD<sub>GSH</sub> in Figure 2.6 and other QD<sub>X</sub> in Figure A31–Figure A, with a few exceptions, the curves at the highest enzyme concentrations for each enzyme converged at the end points. This important feature signifies that the enzyme digestion was complete for all of the QD<sub>X</sub>

substrates, except for  $\text{QD}_{\text{SB}}\text{-Sub(A680)}_8$  and  $\text{QD}_{\text{CB}}\text{-Sub(A680)}_8$  with thrombin. However, the proteolytic activity on these QDs might be too slow to see a clear digestion trend. The proteolytic activity of thrombin on zwitterionic QDs will be further explored in Chapter 3.

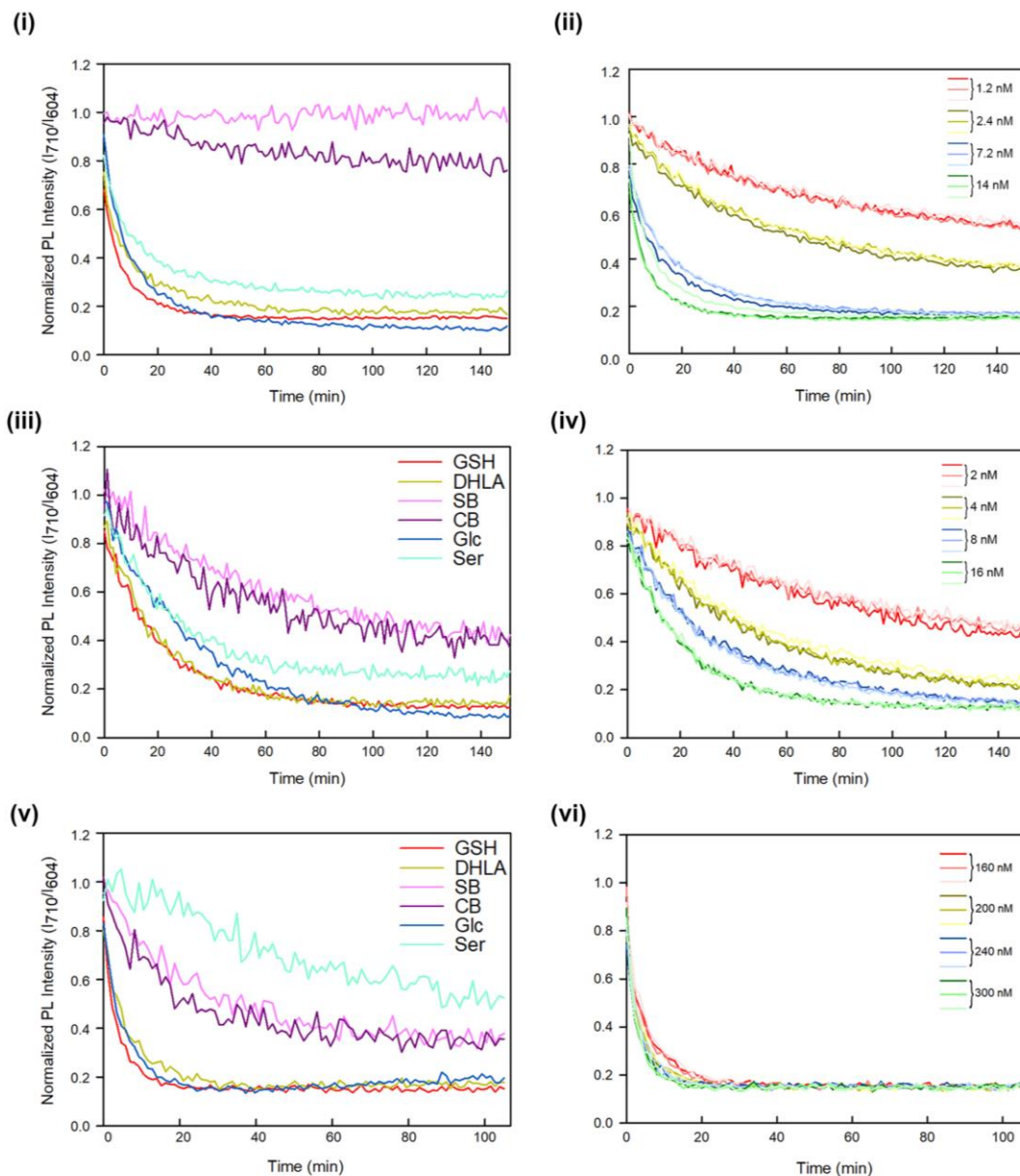


**Figure 2.6.** Left column: summary progress curves of  $\text{QD}_x$ . Right column: representative progress curves of  $\text{QD}_{\text{GSH}}$ . (i–ii) assays with thrombin; (iii–iv) assays with trypsin; (v–vi) assays with papain. Summary progress curves shown for (i) 14 nM thrombin, (iii) 16 nM trypsin, and (v) 240 nM papain. (i) shares the same legend as (iii) and (v).

### 2.5.3 Average Rate of Enzyme Digestion on QD<sub>x</sub>

Average rates of the proteolysis were extracted from the progress curves and summarized by Figure 2.7. QD<sub>GSH</sub> was consistently associated with the fastest proteolytic rates whereas the zwitterionic ligands were associated with lower proteolytic activities, as expected from the progress curves. The subtle differences in the rates among different QDs versus enzymes might be a consequence of different enzyme sizes since thrombin is slightly larger than trypsin and papain (37 kDa for thrombin and 23 kDa for trypsin and papain), but this does not explain the variations between assays with trypsin and papain. More experiments with different sizes of proteases would be needed to confirm this hypothesis. No clear trend can be discerned from the differences in the proteolytic activities based on the isoelectric points. At the experimental pH, which is pH 9 for thrombin and trypsin and pH 7 for papain, thrombin would be expected to have an overall negative charge, while trypsin and papain would be expected to be positively charged given their pIs. Different modes of action may exist on the surface of QD<sub>x</sub> between various classes of proteases. However, no conclusion can be drawn based on the two serine (thrombin and trypsin) and one cysteine (papain) proteases.

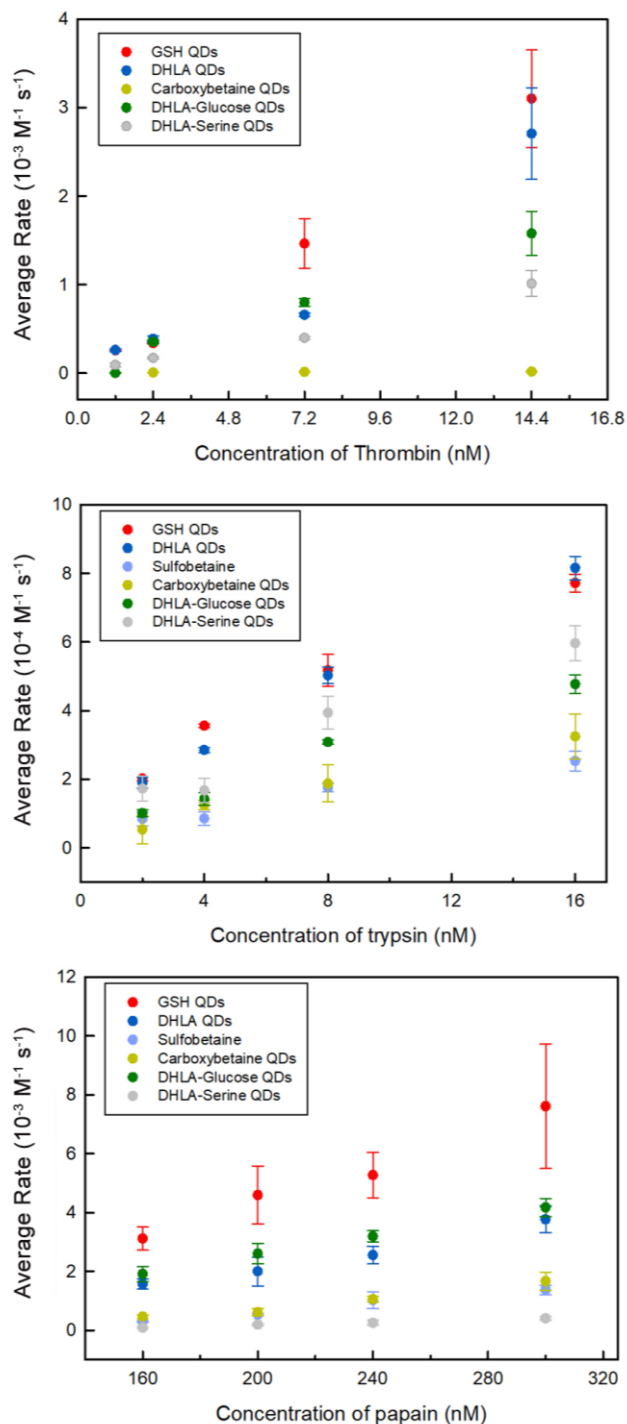


**Figure 2.7.** Summary of the average proteolytic rates on QD<sub>x</sub> for thrombin (top), trypsin (middle), and papain (bottom). QD<sub>SB</sub> was not shown for thrombin because there was virtually no activity.

## 2.5.4 Relative Rate of Enzyme Digestion on QD<sub>X</sub>

Despite the lack of clear trends between the proteolytic rates among the different QD<sub>X</sub>, there are significant differences between the proteolytic rates. The relative rates of certain pairs of QD<sub>X</sub> are distinct for each enzyme. For example, the relative rate of QD<sub>Glc</sub> and QD<sub>SB</sub> can be used to distinguish thrombin from trypsin and papain, whereas the relative rate of QD<sub>GSH</sub> and QD<sub>Ser</sub> can be used to distinguish papain from thrombin and trypsin. When relative rates were generated by comparing average proteolytic rate on QD<sub>X</sub> against QD<sub>DHLA</sub> at a given enzyme concentration, a unique fingerprint for each enzyme can be generated (Figure 2.8). Although the figure below only shows the relative rates at the highest concentration of each enzyme used in the experiments, the trends are consistent across the various concentrations used for each enzyme assay. These patterns are useful for determining the minimal number of QD<sub>X</sub> to identify thrombin, trypsin, or papain in an array format. Moving forward, a more extensive ligand library and surface chemistry can be developed and potentially be used to distinguish between more enzymes.

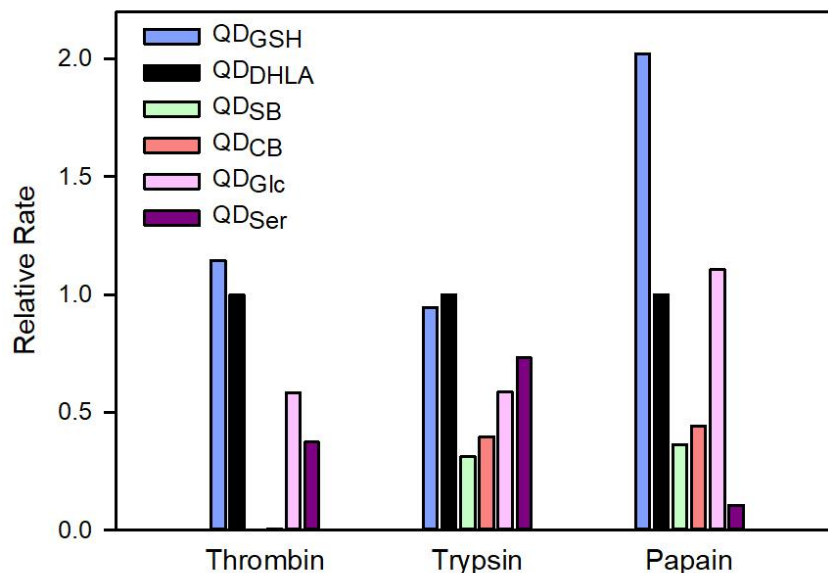


**Figure 2.8.** Relative proteolytic rates of QD<sub>X</sub> compared to QD<sub>DHLA</sub>. One concentration was used for each given enzyme.

## 2.6 Conclusion

Six ligands were synthesized and characterized using NMR spectroscopy and ESI-MS. These ligands were reliably ligand-exchanged using the LA-based and imidazole-based methods. QDs capped with the synthesized ligands, along with GSH- and DHLA-capped QDs were characterized by DLS and Ferguson analysis. It was found that while the QDs were similar in their hydrodynamic diameters, the zwitterionic QDs had 60% less zeta potential compared to other LA-based ligands. The stability of these QDs were qualitatively evaluated over the course of four weeks. Among the QDs evaluated, QD<sub>Glc</sub> showed good stability over a wide pH range, from pH 4–11, followed by QD<sub>GSH</sub>, which was stable across pH 6–11. QD<sub>API-Glc</sub> had the smallest range of pH stability, which is consistent with the weaker and more pH-sensitive binding of imidazole-based ligands [117].

Enzyme assays with different substrate-conjugated QD<sub>X</sub> were conducted with thrombin, trypsin, and papain. The proteolytic rates varied widely across different QD coatings, however, the trend was not clear as to why some QDs were associated with faster proteolytic rates for one enzyme but not for others, and vice versa. In particular, zwitterionic QDs were associated with slower proteolytic rates, whereas GSH-capped QDs were often associated with the fastest rates. A combination of these QDs can be potentially useful in an array format for the generation of an enzyme fingerprint, where the relative proteolytic rates of the enzyme can be used to identify an unknown enzyme.

## Chapter 3 : Evaluating the Effects of Small Molecule Ligands and Macromolecules on Proteolytic Activity

### 3.1 Introduction

Thrombin is an important serine protease in the coagulation pathway that promotes hemostasis by converting coagulation factors into their active forms. One of the products in this cascade is fibrin, which is generated from fibrinogen, and the spontaneous association of fibrin monomers forms a fibrin clot [118]. In addition, thrombin promotes platelet aggregation and activation of cellular responses via proteinase-activated receptors (PAR) on the surface of platelets [99,119].

Thrombin cleaves after arginine residues but displays great substrate specificity in addition to the active site. Part of this specificity can be attributed to the two anionic-binding exosites that are distinct from the catalytic site (Figure 3.1). Exosite I consists of basic amino acid residues Lys21, Arg62, Arg68, Arg70, Arg73, Lys106, and Lys107 and is considered to be responsible for the binding of fibrinogen [119]. Thrombin lacking exosite I has been found to be unable to convert fibrinogen into fibrin, despite demonstrating activity towards synthetic peptide substrates. Other prominent substrates that bind to exosite I include PAR1, Factor V, Factor VIII, and thrombomodulin, among others. Notably, hirudin is a powerful inhibitor of thrombin that interacts with exosite I and blocks the active site with its extended acidic C-terminus and N-terminus, respectively. [120]. Exosite II also consists of several basic residues, including Arg89, Arg98, Arg245, Lys248, and Lys252, and the exosite is known to bind to sulfated glycosaminoglycans such as heparin through electrostatic interactions.

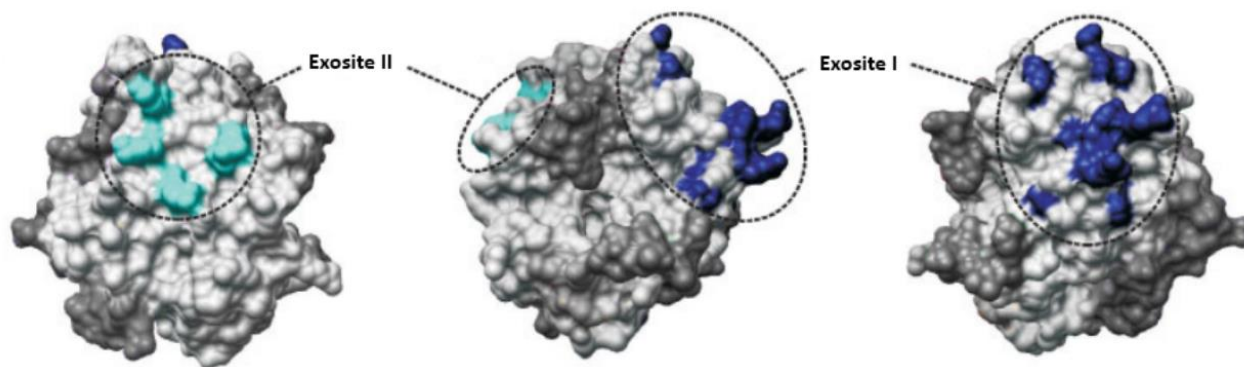


**Figure 3.1.** Thrombin anion-binding exosites in left, standard, and right orientations. Adapted from reference [119], copyright 2006 Thieme Medical Publishers.

PAR1 is known to modulate thrombin activity through allosteric interactions with exosite I as seen in Figure 3.2 [119,121]. It contains an exodomain at the N-terminus that undergoes thrombin cleavage at LDPR<sup>41</sup>↓S<sup>42</sup> to generate a new N-terminus. This new terminus then activates the signalling pathway by binding intramolecularly to the receptor as a tethered ligand. The newly generated N-terminus of PAR1 also contains a hirudin-like acidic sequence, DKYEPFWEE, which has been shown to enhance thrombin activity towards PAR1-based substrates [122–124], and alter the thrombin activity to varying degrees towards chromogenic substrates [125].

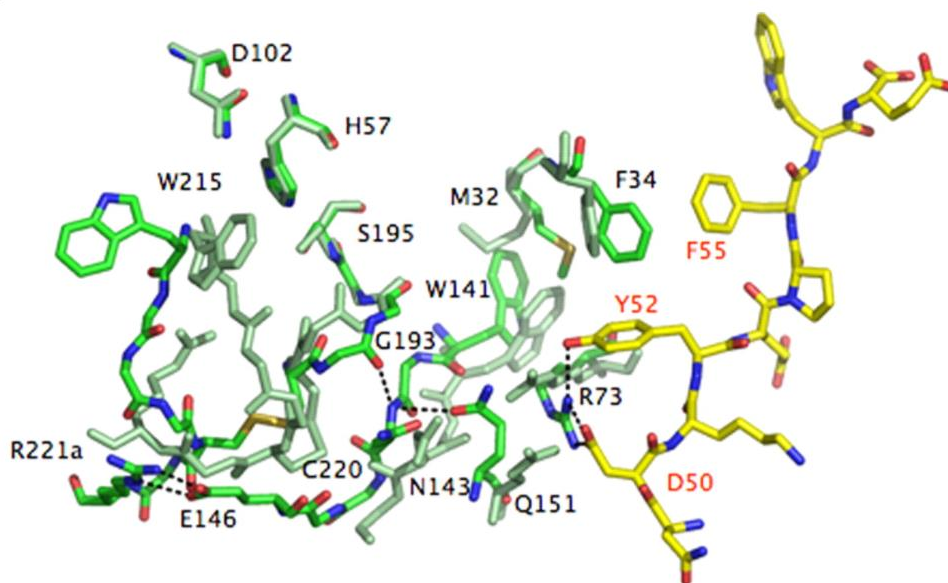


**Figure 3.2.** Mutant thrombin D102N in self-inhibited conformation (light green) and the catalytically competent enzyme (green) complexed with PAR1 (yellow). Thrombin binding of PAR1 via part of the hirudin sequence can be seen with Phe55, Tyr52, and Asp50. Through allosteric communications, the PAR1 bound mutant restores the oxyanion hole formed by Ser195 and Gly193 and frees the catalytic His57 from the hydrophobic interactions with Trp215. The binding also restores the access to the active site and the primary specificity site by shifting the 220-loop formed by the Cys191-Cys220 disulfide bond. The mutant thrombin-PAR1 complex and its relative free enzyme demonstrate the molecular basis of the allosteric communications of PAR1. Reproduced from reference [121], copyright 2008 National Academy of Sciences.

This chapter focuses on coupling the PAR1 hirudin-like sequence to substrate-conjugated QDs to enhance thrombin activity towards a previously reported thrombin substrate sequence [126]. In this study, the thrombin substrate was labeled with Alexa Fluor 647 dye via maleimide-thiol

coupling. An unlabeled thrombin substrate with a different sequence was used as a control in this experiment to account for changes, if any, in the enzyme activity as a result of surface passivation. The effect of PAR1 was evaluated both when conjugated to QDs and when in bulk solution. A list of peptides used in this study can be found in Table 3.1, including their peptide sequences, molecular weight (MW), and their abbreviations. The peptides were conjugated to QDs via hexahistidine tag-mediated self-assembly after the initially hydrophobic QDs were ligand-exchanged with hydrophilic ligands. Changes in the FRET PL ratio between the CdSe/CdS/ZnS QDs and the dye-labeled substrates were used to monitor the progression of the enzyme-catalyzed substrate digestion. QDs with different ligand coatings, including DHLA, GSH, SB, CB, and Glc were also assessed to determine their effect on the protease probe.

## **3.2 Experimental Methods**

### **3.2.1 Materials**

L-glutathione reduced (GSH), tetramethylammonium hydroxide (TMAH) solution in methanol (25% w/v), TMAH solution in H<sub>2</sub>O (25% w/v), sodium borohydride ( $\geq 98\%$ ), lipoic acid (LA,  $\geq 99\%$ ), and trypsin from bovine pancreas were from Sigma-Aldrich (Oakville, ON, Canada).

CdSe/CdS/ZnS core/shell QDs with peak PL at 604 nm (QD604), 630 nm (QD630), 650 (QD650<sup>1</sup> and QD650<sup>2</sup>) were synthesized by a collaborator using a previously reported method [107,108]. Alexa Fluor 647 C2 maleimide, Alexa Fluor 680 C2 maleimide, decolourizing carbon, triethylamine, and acetic acid were from Thermo-Fisher Scientific (Carlsbad, CA, USA). Ni-NTA agarose was from Qiagen (Hilden, Germany). Oligonucleotide purification cartridge was from Life Technologies (Carlsbad, CA, USA).

Human alpha-thrombin ( $>95\%$ ) was from Haematologic Technologies, Inc. (Essex Junction, VT USA). Peptides were from Bio-Synthesis Inc. (Lewisville, TX, USA) and the peptide sequences are shown in Table 3.1.

Buffers were prepared with water purified by Milli-Q Synthesis Water Purification System from Millipore (Burlington, MA, United States) and filtered through a 0.22  $\mu\text{m}$  sterilized syringe filter. Buffers included TEAA (2 M, 0.2 M), Phosphate-buffered saline (PBS; 10 mM  $\text{Na}_2\text{HPO}_4$ , 1.8 mM  $\text{KH}_2\text{PO}_4$ , 137 mM NaCl, 2.7 mM KCl), borate buffer (50 mM, pH 9.2; 50 mM, pH 9.2, 250 mM NaCl), HEPES (100 mM, pH 7.0, 50 mM NaCl), and TBE (1 M Tris, 0.9 M boric acid, and 0.01 M EDTA).

**Table 3.1.** Peptide sequences.

Peptide sequence (N-terminus to C-terminus) <sup>a</sup>	MW	Abbreviation
$\text{H}_6\text{SP}_5\text{GSDGNESGLVPR}\downarrow\text{GSGC}$	3.0 kDa	Sub
$\text{H}_6\text{GGSGGGGGYNPNDKYEPFWEDEEKNESG}$	3.8 kDa	HisPAR
$\text{GGSGGGGGYNPNDKYEPFWEDEEKNESG}$	3.0 kDa	PAR
$\text{GGNGSGQNGAAYALVPR}\downarrow\text{GSGP}_5\text{GH}_6$	3.1 kDa	Sub <sup>2</sup>
$\text{H}_6\text{GP}_5\text{GSDGNEGNLAGSGC}$	2.6 kDa	Pep

<sup>a</sup> Substrate cleavage P1 site is bolded and denoted with a downward arrow.

## Ligand Exchange

$\text{QD}_{\text{SB}}$ ,  $\text{QD}_{\text{CB}}$ , and  $\text{QD}_{\text{Glc}}$  ligand exchange procedures are described in Chapter 2.2.

### $\text{QD}_{\text{DHLA}}$ Ligand Exchange

Neat DHLA (26 mg, 0.13 mmol) was dissolved in 50  $\mu\text{L}$   $\text{CHCl}_3$  in a microcentrifuge tube. From a  $\text{QD}_{604}$  stock solution with a concentration of 235  $\mu\text{M}$ , 6.0  $\mu\text{L}$  (1.4 nmol) was added to the microcentrifuge tube. The solution was vortexed and then incubated for 3 h at 60 °C. Borate buffer (50 mM, pH 9.2, 200  $\mu\text{L}$ ) and TMAH (100  $\mu\text{L}$ , 25% w/v in methanol) were added to the microcentrifuge tube and the layers were left to separate after mixing. The aqueous layer was transferred to a new microcentrifuge tube. The QDs were washed by three cycles of precipitation with EtOH, centrifugation at 17 000 rcf, and redispersion in borate buffer-NaCl (50 mM, 250 mM NaCl, pH 9.2). After the final wash, the QDs were redispersed in borate buffer (50 mM, pH 9.2) and stored at 4 °C.

### **QD<sub>GSH</sub> Ligand Exchange**

Glutathione (40 mg, 0.13 mmol) was dissolved in 100  $\mu$ L TMAH in methanol (25% w/v). In a microcentrifuge tube, 6  $\mu$ L of a QD604 stock solution (235  $\mu$ M, 1.4 nmol) was diluted with 100  $\mu$ L of  $\text{CHCl}_3$ . The ligand solution was added to the microcentrifuge tube, followed by the addition of 200  $\mu$ L of borate buffer (200  $\mu$ L, 50 mM, pH 9.2). The microcentrifuge tube was vortexed until the layers separated and incubated in the dark overnight at 55 °C. The aqueous layer was transferred to a new microcentrifuge tube. The QDs were precipitated with 1:1 MeOH/acetone mixtures at 17 000 rcf and redispersed in borate buffer-NaCl (50 mM, 250 mM NaCl, pH 9.2). After three total washing and redispersion cycles, the QDs were redispersed in borate buffer (50 mM, pH 9.2) and stored at 4 °C.

### **3.2.2 Peptide Labeling**

Thrombin substrate (Sub) with a cysteine residue was labeled with Alexa Fluor 647 C2 maleimide (A647) according to previously published protocols [127]. Thrombin substrate was also labelled with Alexa Fluor 680 C2 maleimide (A680) using the same method. Sub (1 mg, 0.3  $\mu$ mol) was dissolved in 10  $\mu$ L of 50% MeCN (aq) and mixed with A647 (1 mg, 0.8  $\mu$ mol) dissolved in 5  $\mu$ L of DMSO. The solution was diluted with 200  $\mu$ L of HEPES buffer (pH 7.0, 100 mM, 50 mM NaCl). The reaction was agitated by a mixer in the dark at room temperature for 4 h and stored at 4 °C before purification (if purification was not immediate after the reaction). The labeled peptides were purified with a nickel(II)-nitrilotriacetic acid (Ni-NTA) agarose resin.

Two freshly prepared Ni-NTA cartridges were each rinsed with 5 mL PBS. The reaction mixture was first loaded onto the first cartridge by flushing the reaction mixture through the cartridge for 2–3 min. Similarly, the remaining solution was flushed through the second cartridge. Each cartridge was washed in sequence with 10 mL of PBS, 10 mL of 1:1 EtOH/PBS mixture, and followed by 2  $\times$  10 mL of PBS. The bound peptide was eluted with 3  $\times$  0.5 mL 300 mM imidazole (filtered through decolourizing carbon). The peptide solution was then desalted using an oligonucleotide purification cartridge (OPC). Briefly, Amberchrom CG300 resin was conditioned overnight in a solution of 1:3 resin suspension: 20% v/v *i*-PrOH (aq). After loading the column, the resin was washed with 3 mL of MeCN, followed by 3 mL of 2 M TEAA buffer. The peptide solution was flushed through the OPC column for 2 min, or until the solution turned colourless.

The column was washed with  $4 \times 10$  mL of 0.2 M TEAA buffer and eluted with  $2 \times 0.5$  mL 70% MeCN (aq). The solution was aliquoted into four fractions, dried under vacuum, and stored at  $-20^{\circ}\text{C}$ .

### 3.2.3 Peptide Quantification and Self-Assembly

A647-labelled thrombin substrate, Sub(A647), was dissolved in 1 mL of borate buffer and stored at  $4^{\circ}\text{C}$  until needed. The concentration of the peptide was determined by the absorbance of the A647 ( $\epsilon = 270\,000\text{ M}^{-1}\text{ cm}^{-1}$  at 647 nm) using the plate reader.

HisPAR and PAR peptides were quantified using their absorbance at 280 nm from the tyrosine and tryptophan residues in their sequences. The molar extinction coefficient was estimated to be  $9970\text{ M}^{-1}\text{ cm}^{-1}$  using the ExPASy ProtParam software (SIB Swiss Institute of Bioinformatics, Lausanne, Switzerland) [128].

### 3.2.4 Characterization of QDs

#### Agarose gel electrophoresis

Maximum substrate loading of QD604 was visualized using 1% w/v agarose gel electrophoresis and Alexa Fluor 488-labelled thrombin substrates, Sub(A488). Samples were prepared with stock solutions of QD<sub>DHLA</sub> and Sub(A488) in borate buffer (pH 9.2) to achieve final concentrations of  $0.4\text{ }\mu\text{M}$  for the QDs and  $8\text{ }\mu\text{M}$ ,  $16\text{ }\mu\text{M}$ ,  $24\text{ }\mu\text{M}$ , and  $36\text{ }\mu\text{M}$  for Sub(A488). Control samples of QD and Sub(A488) were prepared with final concentrations of  $0.4\text{ }\mu\text{M}$  and  $6.6\text{ }\mu\text{M}$ , respectively. Glycerol was added to the samples to achieve a final concentration of 2% v/v. The gel was run for 30 min at  $6.67\text{ V cm}^{-1}$  in  $1 \times$  TBE buffer (100 mM, pH 8.3) and imaged with a smartphone.

Protease adsorption on QD<sub>X</sub> and QD<sub>X</sub>-[HisPAR]<sub>40</sub> was evaluated via electrophoretic mobility shift assays on 1% w/v agarose gels. The samples were prepared by mixing thrombin and QDs to achieve final concentrations of  $0.2\text{ }\mu\text{M}$  QD<sub>X</sub> and  $0.1\text{ }\mu\text{M}$ ,  $0.2\text{ }\mu\text{M}$ ,  $0.4\text{ }\mu\text{M}$ ,  $0.8\text{ }\mu\text{M}$ ,  $1.6\text{ }\mu\text{M}$ ,  $3.2\text{ }\mu\text{M}$ ,  $6.4\text{ }\mu\text{M}$ , or  $10\text{ }\mu\text{M}$  of thrombin. QD<sub>X</sub>-[HisPAR]<sub>40</sub> samples were prepared with the addition of HisPAR ( $8\text{ }\mu\text{M}$  final concentration). The samples were incubated for at least 20 min at room temperature. Glycerol (20% v/v) was added just before the sample loading to achieve a final

concentration of 1.3% and 1  $\mu\text{L}$  of sample was loaded onto the gel. The gels were run for 20 min at  $6.67 \text{ V cm}^{-1}$  in  $1 \times$  TBE buffer (100 mM, pH 8.3) and imaged with Gel Doc XR+ System (Bio-Rad Laboratories Inc., Hercules, CA, USA).

### **Photoluminescence (PL) measurements**

Peptide-conjugated QDs were characterized by a plate reader (Tecan Ltd., Morrisville, NC, USA). The PL intensities of A647 and QD604 were monitored at 668 nm and 604 nm, respectively, using an excitation wavelength at 400 nm for QD604. Minimal direct excitation of A647 was observed at 400 nm. The samples were prepared with borate buffer (100 mM, pH 9.2).

### **3.2.5 Spectral Overlap and Förster Distance of QD604-A647 Pair**

Spectral overlap between QD604 and A647 was determined by measuring the absorbance spectra over the range of 450–850 nm. The PL spectrum for QD604 was measured between 450–850 nm with 2 nm step size using an excitation wavelength of 400 nm. PL spectrum for A647 was measured between 620–850 nm with 2 nm step size using an excitation wavelength of 610 nm. Both measurements were done using excitation light of a fixed bandwidth (5 nm).

### **3.2.6 Proteolytic Assays**

$\text{QD}_X\text{-Sub(A647)}_8\text{-[Y]}_N$ , where X was the ligand on the QD (X = GSH, DHLA, SB, CB, or Glc), Sub(A647) was A647-labeled thrombin substrate, Y was an unlabeled peptide (Y = HisPAR, PAR or Sub<sup>2</sup>), were prepared by mixing QDs with 8 equivalents of Sub(A647) and  $N$  equivalents of  $Y$  in borate buffer (50 mM, pH 9.2). Thrombin was prepared by diluting the commercially available thrombin of a known concentration with borate buffer (pH 7) and stored at  $4^\circ\text{C}$ . We observed that thrombin stored in this method maintained similar activity even a year after preparation. Fresh trypsin stock solutions were prepared before the assays by dissolving trypsin in 1 M HCl (aq) and its concentration was determined from the absorbance at 280 nm ( $\epsilon = 37\,650 \text{ cm}^{-1} \text{ M}^{-1}$ ). Working solutions of the QD conjugates and proteases were prepared by scaling the final concentrations by a factor of two. Final concentrations of 50 nM QD, 400 nM Sub(A647), and  $N = 0, 10, 20, 30, 40$  were used in the experiments. Different concentrations of thrombin were used to achieve sufficient activity with various  $\text{QD}_X$ . Final concentrations of 1 nM, 3.5 nM, 5 nM, 5nM, and 8 nM of thrombin were used for GSH, Glc, DHLA, CB, and SB-coated QDs, respectively. A final

concentration of 25 nM of trypsin was used to assay with QD<sub>SB</sub> conjugates. Samples were incubated for a minimum of 30 min prior to the proteolytic assays.

Aliquots of QD conjugate solution were mixed with equal volume of protease solution in a 96-well microtiter plate (final volume = 60  $\mu$ L) just prior to the start of the experiment. Immediately after mixing, PL emissions from the QD and A647 were monitored at 604 nm and 668 nm over 1–2 h, using 400 nm excitation wavelength, and recorded at 1 min intervals. Each experiment was performed in triplicate.

Similarly, 50 nM of QD<sub>SB</sub>-Sub(A680)<sub>8</sub> or QD<sub>SB</sub>-Sub(A680)<sub>8</sub>-[HisPAR]<sub>40</sub> was assayed with final thrombin concentrations ranging 0.1–208 nM. Working thrombin solutions were prepared as double the final concentrations via serial dilutions. The PL emissions from QD and A680 were monitored at 604 nm and 700 nm, respectively, over 3 h using 400 nm excitation wavelength and recorded at 1 min intervals.

QD604<sub>SB</sub>, QD630<sub>SB</sub>, QD650<sup>1</sup><sub>SB</sub>, and QD650<sup>2</sup><sub>SB</sub> substrate conjugates, QD $\lambda$ <sub>SB</sub>-Sub(A680)<sub>8</sub>, were assayed with and without 40 eq. of HisPAR. Final concentrations of 50 nM and 20 nM were used for QD and thrombin, respectively. The PL emissions from the QDs and A680 were monitored at 600 nm, 626 nm, 652 nm, and 704 nm, over 3 h at 90 s intervals using 400 nm excitation wavelength and 26 nm step size.

### 3.3 Data analysis

#### 3.3.1 Proteolytic Assays

Peak PL intensity ratio  $\rho_{A647/QD}$  was calculated according to eqn. 26, where  $I_{668}$  and  $I_{604}$  are the peak PL intensities of A647 and QD604, respectively. No correction factor was required since the signals were well-resolved and there was minimal crosstalk between the two emissions.

$$\rho_{A647/QD} = \frac{I_{668}}{I_{604}} \quad \text{Eqn. 26}$$

The peak PL ratio, as a function of time  $t$  and protease concentration  $[E]$ , was normalized according to eqn. 27, where *control* denotes the sample with borate buffer only (50 mM, pH 9.2), without the addition of enzyme. The normalization serves to minimize PL ratio changes from non-proteolytic processes.

$$\rho_{A647/QD}([E], t)_{normalized} = \frac{\rho_{A647/QD}([E], t)}{\rho_{A647/QD}(control)(t)} \quad \text{Eqn. 27}$$

Progress curves were generated from the normalized PL ratio versus time and fitted with the mathematical functions (eqn. 28 and eqn. 29) using OriginPro (OriginLab, Northampton, MA).  $A_1$ ,  $A_2$ ,  $C$ ,  $k_1$ , and  $k_2$  are constants, and  $0 \leq A_1, C \leq 1$ . For consistency and to minimize overfitting the data set, single exponential model was used when biexponential model gave an  $A_1$  or  $A_2$  value greater than 0.35 (i.e.  $A_1/(A_1+A_2) < 0.35$  or  $A_1/(A_1+A_2) > 0.65$ ) because a single exponential model can better describe the progress curve when it is dominated by one process.

$$\rho_{A647/QD}([E], t) \approx A_1 e^{-k_1 t} + A_2 e^{-k_2 t} + C \quad \text{Eqn. 28}$$

$$\rho_{A647/QD}([E], t) \approx A_3 e^{-k_1 t} + C \quad \text{Eqn. 29}$$

Initial rate constants were calculated by taking the derivatives of eqn. 28 and eqn. 29 at  $t = 0$ . The weighted average rate constants for biexponential model were calculated using eqn. 30.

$$\frac{d \rho_{A647/QD}([E], t)}{dt} = \frac{A_1 \times k_1 + A_2 \times k_2}{A_1 + A_2} \quad \text{Eqn. 30}$$

Sometimes it was necessary to use linear regression when the proteolytic rate was relatively slow. In such cases, the slope of the data would be taken as both the average and initial rates.

### 3.4 Results and Discussion

### 3.4.1 QD604–A647 FRET Pair

Similar to the QD604–A680 FRET pair, QD604 and A647 make a good FRET pair because of their significant spectral overlap. There is also minimal direct excitation of A647 when exciting QD604 at 400 nm and their emissions can be resolved easily given their spectral separation (Figure 3.3). The spectral overlap between QD604 and A647 was determined as  $J = 1.1 \times 10^{-9} \text{ cm}^6 \text{ mol}^{-1}$  and the Förster distances for the various QD<sub>x</sub> are listed in Table 3.2.

**Table 3.2.** Förster distances between QD<sub>x</sub> and A647.

QD <sub>x</sub>	R <sub>0</sub> (nm)
GSH	5.8
DHLA	4.7
SB	5.2
CB	5.2
Glc	5.5
Ser	5.1
API-Glc	5.6

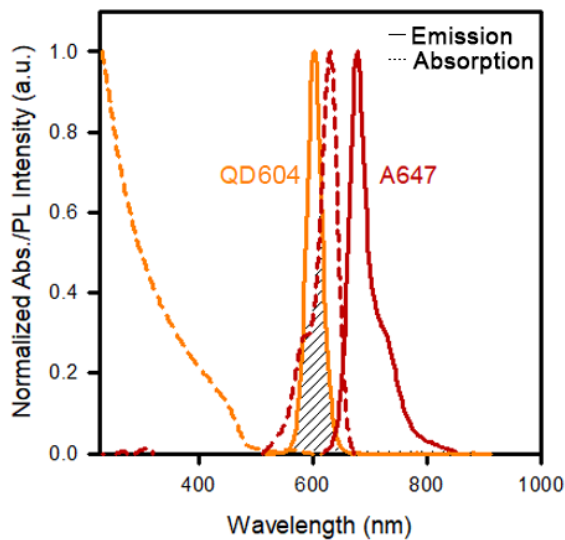


**Figure 3.3.** Normalized absorption and PL emission spectra of QD604 and A647. Spectral overlap between the QD604 emission and A647 absorption is shown as the shaded area.

### 3.4.2 Maximum Substrate Loading on QD604

QD<sub>DHLA</sub> was used to determine the maximum substrate loading. However, it is expected that the self-assembly of Sub(A488) would not differ significantly between the different QD<sub>x</sub>.

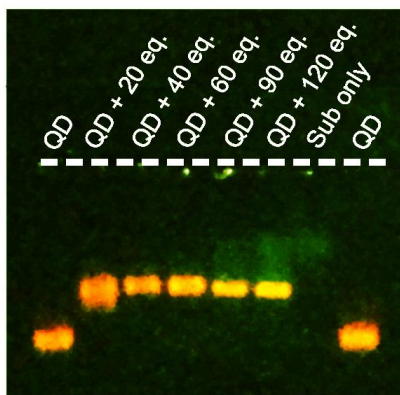


**Figure 3.4.** PL image of an agarose gel after electrophoresis of DHLA-capped QD604 conjugated with 20–120 equivalents of Sub(A488); Sub(A488) is shown for comparison. Image contrast was adjusted using image processing software to show the PL of the faint dye more clearly.

Figure 3.4 shows that the QD surface becomes saturated with Sub(A488) above 60 eq. of the dye-labelled peptide, as indicated by the streaking of the excess dye. Thus, it is expected that 60 or less equivalents of hexahistidine-tagged peptides could be conjugated onto QDs via self-assembly and form a population of QD-[peptide]<sub>N</sub> conjugates where *N* follows a Poisson distribution [129].

### 3.4.3 Proteolytic Assays with Thrombin

Thrombin assays with  $QD_X\text{-Sub}(A680)_8$ , where  $X = \text{GSH}, \text{DHLA}, \text{SB}, \text{CB}, \text{and Glc}$  were summarized by the progress curves shown in Figure 2.4 (i). As shown in the previous chapter, SB and CB-capped QDs were associated with extremely slow thrombin proteolytic rates compared to

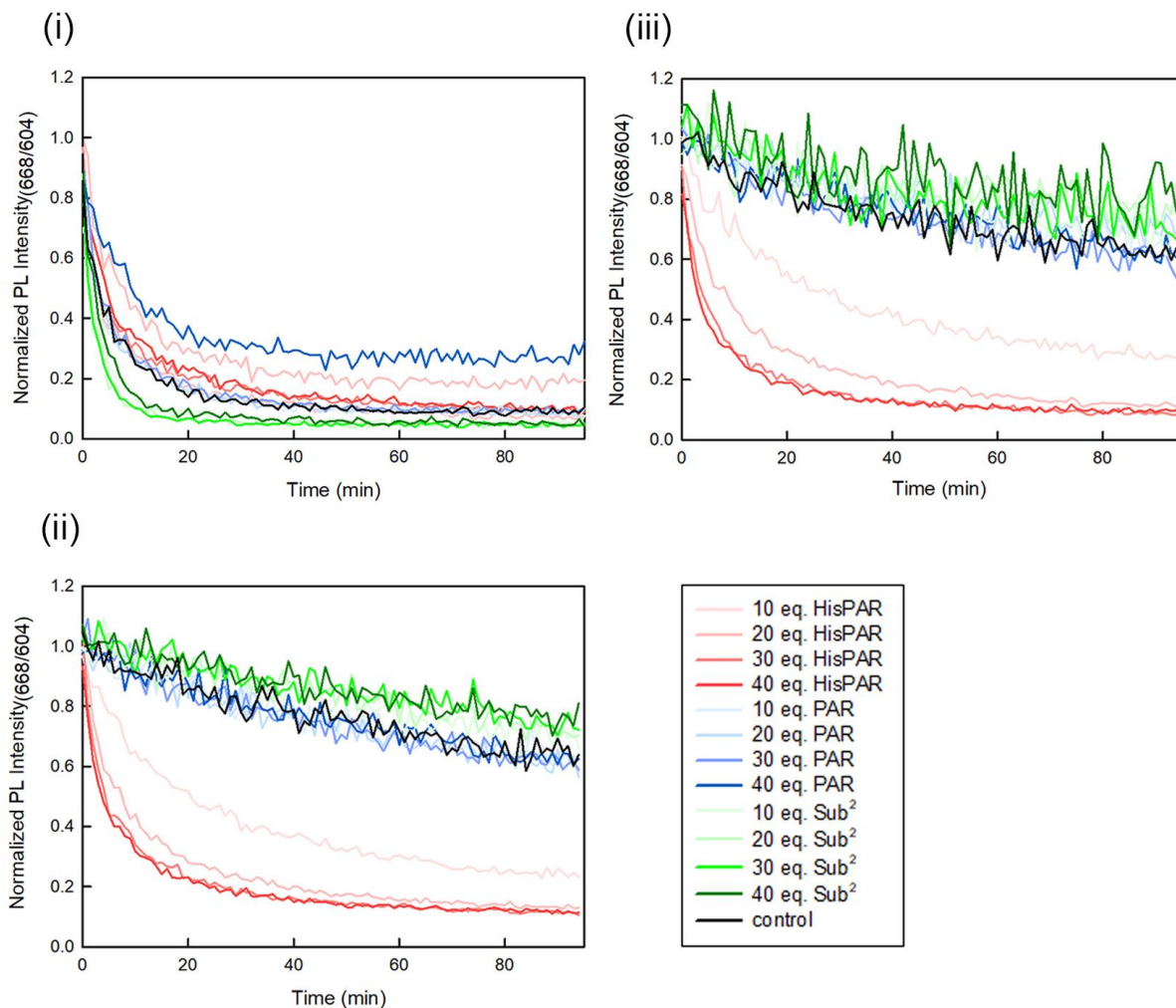


**Figure 3.5.** Progress curves of  $QD_X\text{-Sub}(A647)_8\text{-}[Y]_N$ , where  $X = \text{DHLA}$  (i),  $\text{SB}$  (ii), and  $\text{CB}$  (iii),  $Y = \text{HisPAR}, \text{PAR}, \text{or } \text{Sub}^2$ , and  $N = 0\text{--}40$  of peptides.

other ligands. However, the proteolytic activities on  $QD_{\text{SB}}$  and  $QD_{\text{CB}}$  were drastically altered when assayed as  $QD_X\text{-Sub}(A647)_8\text{-}[Y]_N$  conjugates, where  $Y = \text{HisPAR}$  (Figure 3.5 ii–iii); whereas the enzyme activities on  $QD_{\text{GSH}}$ ,  $QD_{\text{DHLA}}$ ,  $QD_{\text{Glc}}$  were unaltered as shown by the representative progress curves of  $QD_{\text{DHLA}}$  in Figure 3.5 (i) and in Figure A.

### 3.4.4 Initial Rate of $QD_X\text{-Sub(A647)}_8\text{-[Y]}_N$

The relative initial rates of various QD conjugates compared to  $QD_X\text{-Sub(A647)}_8$  are summarized in Figure 3.6 (i–v). As expected by the trend seen in the progress curves,  $QD_{DHLA}$ ,  $QD_{GSH}$ , and  $QD_{Glc}$  had virtually no change in activity between the different conjugates. In the case of zwitterionic ligands, only  $Y = \text{HisPAR}$  increased the relative initial rates with increasing equivalents. This increase was not observed when the non-conjugated PAR was in bulk solution, when the conjugated peptide sequence did not contain the PAR1 sequence, or when  $QD_{SB}\text{-Sub(A647)}_8\text{-[Y]}_N$  was assayed with trypsin.

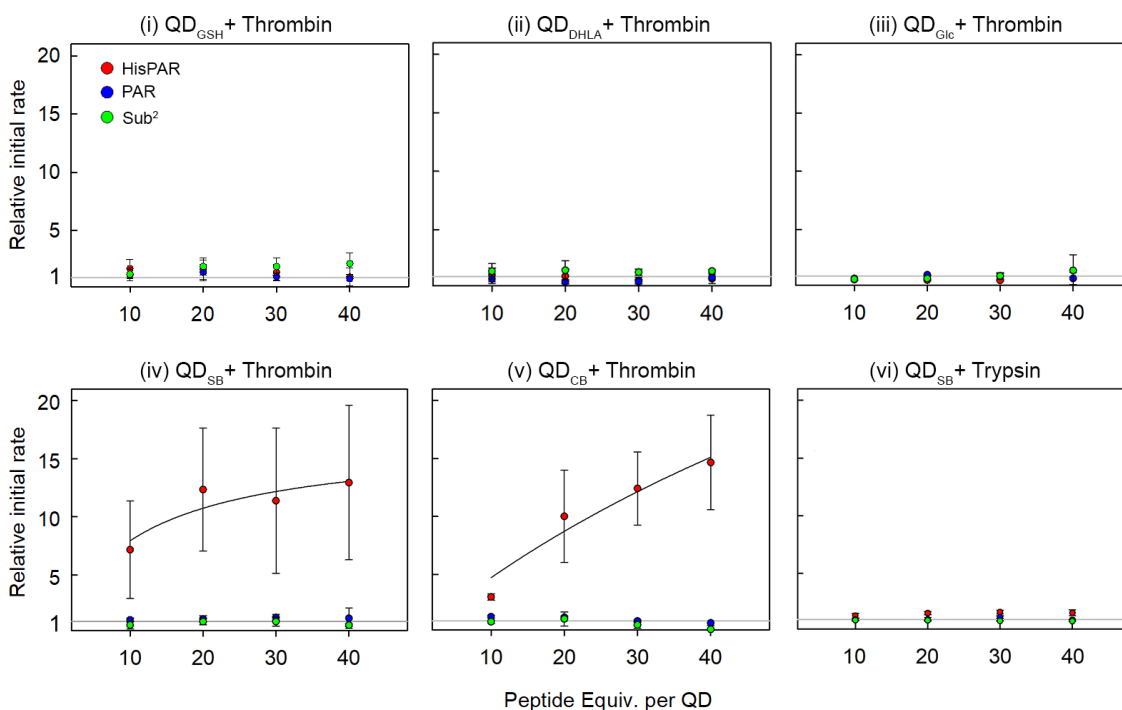


**Figure 3.6.** Summary of relative initial rates for enzyme assays with thrombin (i–v) and trypsin (vi). Relative initial rates of  $QD_X\text{-Sub(A647)}_8\text{-[Y]}_N$  ( $Y = \text{HisPAR}$ ,  $\text{PAR}$ , or  $\text{Sub}^2$ , and  $N = 0\text{--}40$  of peptides) compared to  $QD_X\text{-Sub(A647)}_8$ .  $X = \text{GSH}$  (i),  $\text{DHLA}$  (ii),  $\text{Glc}$  (iii),  $\text{SB}$  (iv, vi), and  $\text{CB}$  (v). Grey line indicates where relative rate = 1 for comparison.

As highlighted in Chapter 2, different ligands are associated with different proteolytic rates. In these experiments, the concentrations of thrombin were varied between  $QD_X$  to obtain sufficient data for the progress curves. Thus, the difference in thrombin concentration can be as large as

eight-fold between the fastest ( $QD_{GSH}$ ) and slowest ( $QD_{SB}$ ) enzyme assays. Despite the lower thrombin concentrations used in the experiments, there was still significant proteolytic activity on  $QD_{GSH}$ ,  $QD_{DHLA}$ , and  $QD_{Glc}$  across different conjugates; whereas in the absence of HisPAR,  $QD_{SB}$  and  $QD_{CB}$  experienced very little proteolysis. The differences in the proteolytic activity suggests that thrombin exhibited another mode of action on the zwitterionic surface that could be mediated by the presence of HisPAR. In addition, the lack of significant enhancement seen with trypsin, another enzyme from the serine protease family, with  $QD_{SB}$ -HisPAR conjugates suggests that this interaction is specific for thrombin, as expected from the known biochemistry of thrombin, trypsin and PAR1. Although the PAR1 exodomain could be cleaved by trypsin, unlike thrombin, trypsin does not undergo the subsequent binding event with the newly-formed N-terminus because of a lack of the anion-binding exosite [130].

#### **3.4.4 HisPAR Enhancement vs. Thrombin Concentration**

$QD_{SB}$ -Sub(A680)<sub>8</sub>-HisPAR<sub>40</sub> was assayed against a series of thrombin concentrations to probe the effect of thrombin concentration on the proteolytic enhancement. As previously observed,  $QD_{SB}$ -Sub(A680)<sub>8</sub> conjugates with HisPAR displayed on the surface were associated with faster proteolytic rates than  $QD_{SB}$ -Sub(A680)<sub>8</sub> alone. It is important to note that while in Chapter 2  $QD_{SB}$  was associated with negligible thrombin activity, the progress curves shown below suggests that enzyme digestion does occur on the surface of  $QD_{SB}$ -Sub(A680)<sub>8</sub> alone without HisPAR, albeit at a very slow pace. In addition, thrombin digestion on  $QD_{SB}$ -Sub(A680)<sub>8</sub> was able to go to completion, as seen from the convergence of the  $QD$ -Sub(A680)<sub>8</sub> curve at the highest thrombin concentration (grey) and the curves for  $QD_{SB}$ -Sub(A680)<sub>8</sub>-HisPAR<sub>40</sub> (pink and red curves). It can be seen from the summary initial rate graph (Figure 3.8) that while the initial rates generally increased with increasing thrombin concentrations for both  $QD_{SB}$ -Sub(A680)<sub>8</sub> and  $QD_{SB}$ -Sub(A680)<sub>8</sub>-HisPAR<sub>40</sub>, this increase tapered off around 100 nM of thrombin for the latter conjugate but continued to increase for the former conjugate. As we would expect from the constant concentration of HisPAR displayed on the surface of QDs, the number of interactions between HisPAR-QD conjugate and an excess of thrombin was limited to the number of HisPAR on QDs. This results in a saturable response with increasing concentrations of thrombin and provides further evidence that the interaction between HisPAR and thrombin is the driving force behind the enhancement.

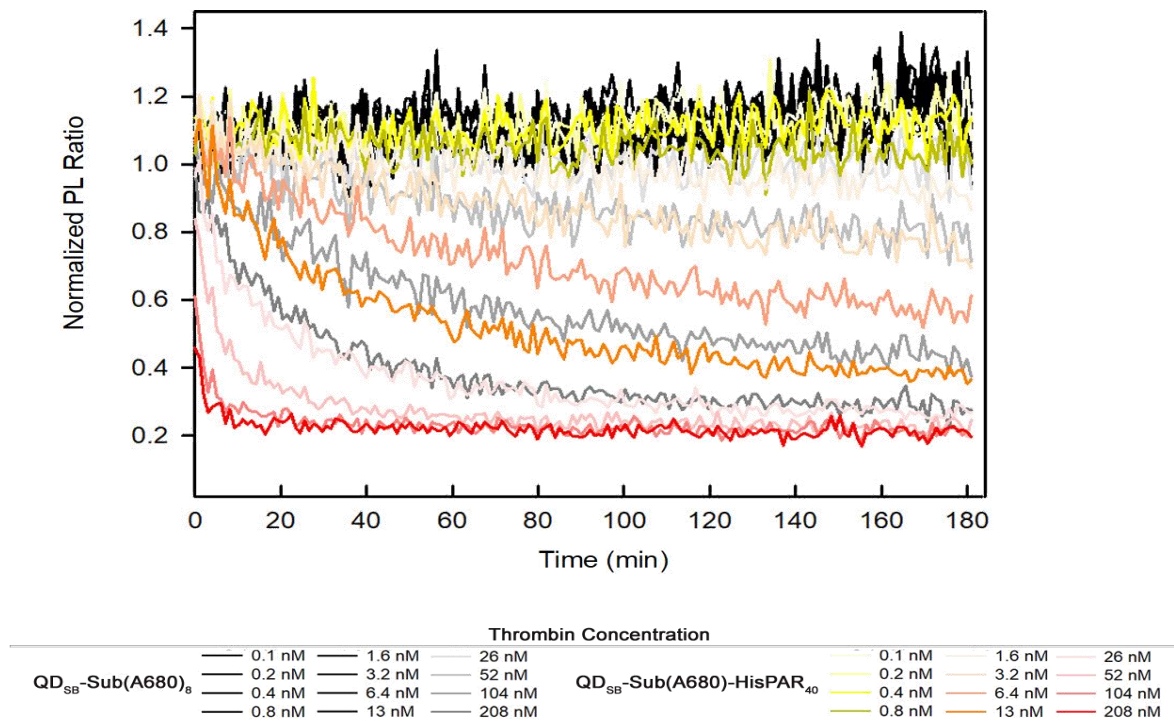


**Figure 3.7.** Progress curves of QD<sub>SB</sub>-Sub(A680)<sub>8</sub> and QD<sub>SB</sub>-Sub(A680)<sub>8</sub>-HisPAR<sub>40</sub> with thrombin concentrations from 0.1 nM–208 nM.

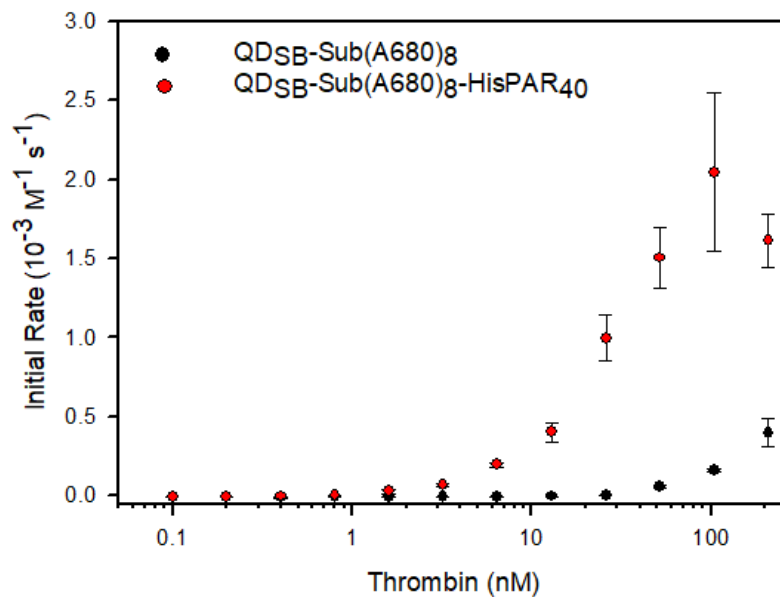


**Figure 3.8.** Summary initial rates of QD<sub>SB</sub>-Sub(A680)<sub>8</sub> and QD<sub>SB</sub>-Sub(A680)<sub>8</sub>-HisPAR<sub>40</sub> with thrombin concentrations from 0.1 nM–208 nM.

### 3.4.5 HisPAR Enhancement on Different Nanocrystals

QDs can vary widely batch-to-batch in their physical properties, including their crystal structure, shape and number of facets, and thickness of the inorganic shell(s). More variations are introduced when comparing QDs with different sizes, materials, and core/shell structures. All of these factors could result in subtle differences in QD's surface chemistry and potentially enzyme activity on the QD platform. Thus, different nanocrystals were tested using similar experimental conditions as above to gauge the generalizability of the HisPAR enhancement across different batches and sizes of QDs.

Between the different  $QD\lambda$ , where  $\lambda$  is the emission wavelength of the QD,  $QD\lambda_{SB-Sub(A680)_8-HisPAR_{40}}$  was consistently associated with faster proteolytic rates than the conjugates without HisPAR, i.e.  $QD\lambda_{SB-Sub(A680)_8}$ , and  $QD\lambda_{SB-Sub(A680)_8-Sub^2_{40}}$ . The proteolytic enhancement ranged from two-fold to sixteen times that of the control (Figure 3.9). In particular, there was a significant difference in the proteolytic rates between the two batches of QDs with emission wavelength of 650 nm. Such a difference may arise from less favourable orientation with which

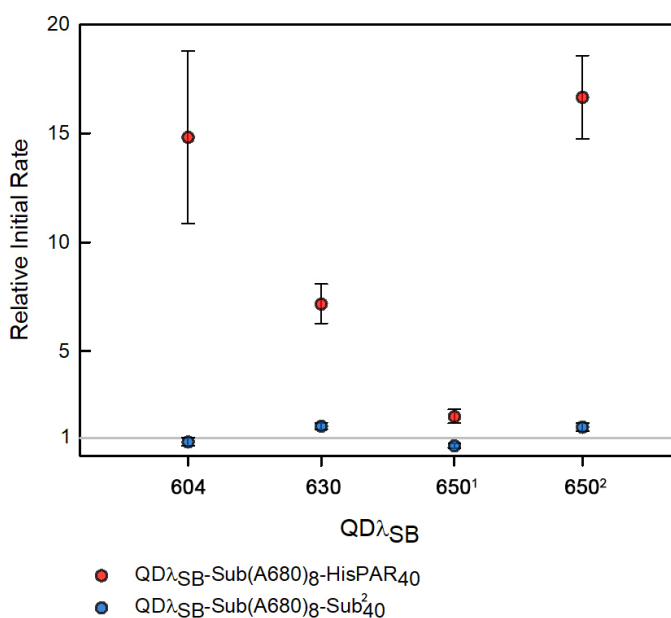


**Figure 3.9.** Relative initial rates of  $QD\lambda_{SB-Sub(A680)_8-[Y]_{40}}$  ( $Y = HisPAR, PAR, \text{ or } Sub^2$ ) compared to  $QD\lambda_{SB-Sub(A680)_8}$ .  $\lambda$  denotes the emission wavelength of the QD ( $\lambda = 604, 630, 650^1, 650^2$  nm). Grey line indicates where relative rate = 1 for comparison.

the HisPAR was arranged on the surface of the QDs so that HisPAR enhanced the proteolytic activity to a lesser degree compared to the other QDs.

### 3.4.6 Protease Adsorption on QDs

Thrombin adsorption on QD<sub>X</sub> was probed using agarose gel electrophoresis to help elucidate the differences in enzyme activity. QD<sub>Glc</sub> was not investigated because its zeta potential and proteolytic profile were very similar to that of QD<sub>DHLA</sub> and QD<sub>GSH</sub>.

Agarose gel electrophoresis reflects protease adsorption in the form of changes in electrophoretic mobilities and band shape of the samples. When enzymes are adsorbed onto the surface of QD, the electrophoretic mobility of the QD is reduced because of an increase in the effective size. Band shape can provide further insight into the nature of the interaction. Streaking and lack of a well-defined band indicate a weak and dynamic interaction that maybe disrupted in the presence of an electric field or by the agarose matrix. A sample that results in multiple bands on a gel suggests a stronger interaction that is less susceptible to external factors, whereas a sample with no apparent mobility suggests that the interaction between the QD and the enzyme is extensive and the effective diameter of the QD is larger than that of the agarose gel pore size.

Consistent with our previous findings, QD<sub>DHLA</sub> and QD<sub>GSH</sub> began to aggregate at 0.8–1.6  $\mu\text{M}$  of thrombin as shown in Figure 3.10 (i–ii, top) [113,131]. Zwitterionic QDs, on the other hand, showed minimal thrombin adsorption and electrophoretic mobility shifts even at thrombin concentration as high as 10  $\mu\text{M}$  (Figure 3.11 iii–iv, top). When 40 eq. of HisPAR was conjugated onto QD<sub>X</sub>, QD<sub>GSH</sub> exhibited the same adsorption trend as before, whereas QD<sub>DHLA</sub> no longer showed the severe aggregation that was seen before (Figure 3.10 ii, middle). Instead, the electrophoretic mobility of QD<sub>DHLA</sub> was slowed down by the thrombin adsorbed on the surface from 0.8–6.4  $\mu\text{M}$  until the electrostatic force from thrombin, which was negatively charged under the experimental conditions ( $\text{pI} \approx 7$ ), overcame the drag force around 10  $\mu\text{M}$ . The discrete bands that formed at 3.2–10  $\mu\text{M}$  of thrombin indicate that thrombin was strongly adsorbed onto the surface of QD<sub>DHLA</sub> and thereby forming distinct populations that could be separated using agarose gel electrophoresis. The electrophoretic mobilities of HisPAR-conjugated QD<sub>SB</sub> and QD<sub>CB</sub> were both changed at higher concentrations of thrombin ca. 1.6–10  $\mu\text{M}$  and the QDs also showed signs

of streaking, which indicate that their interactions with thrombin were more dynamic and weaker compared to that of QD<sub>DHLA</sub> and QD<sub>GSH</sub>. Finally, a control was run with QD<sub>X</sub> conjugated to 40 eq. of a peptide without a recognition site for thrombin (Pep, see Table 3.1). The controls were originally run with QD<sub>X</sub>-[Sub<sup>2</sup>]<sub>40</sub>, however, the agarose gels had significant streaking which made the bands difficult to resolve. Virtually no change in thrombin adsorption was seen when QD<sub>X</sub> was conjugated to 40 eq. of Pep (Figure 3.10 and Figure 3.11, bottom).

Thrombin showed little, if any, adsorption to the zwitterionic QDs. This result supports previous findings on zwitterionic-based nonfouling materials and that they can minimize non-specific interactions [132]. It has been proposed that the nonfouling zwitterionic surfaces can electrostatically induce hydration, much similar to how hydrophilic surfaces, such as those modified with PEG and sugar alcohols, are hydrated via hydrogen bonding. This tightly surface-bound water layer is a physical and energetic barrier to protein adsorption [133,134]. In addition, zwitterions have the potential to form interzwitterion pairs and minimize interactions with other species in solution [135]. The slow proteolytic rates associated with the zwitterionic QDs might then be attributed to the lack of interaction between the surface of the QDs and thrombin.

When the zwitterionic QDs were conjugated to Pep, the non-specific adsorption was still minimized. However, when the QDs were conjugated to HisPAR some interactions with thrombin could be seen when the electrophoretic mobility shifts were magnified at higher concentrations of thrombin. Given that the PAR1 sequence in HisPAR, it is likely that the interactions of QD<sub>X</sub>-HisPAR conjugate stemmed from HisPAR allosterically interacting with thrombin's exosite I. For QD<sub>DHLA</sub>, HisPAR reduced the aggregations induced by high thrombin concentrations, likely by providing better passivation than Pep, but the interactions between the QD and thrombin were too strong to enhance the proteolytic rate.

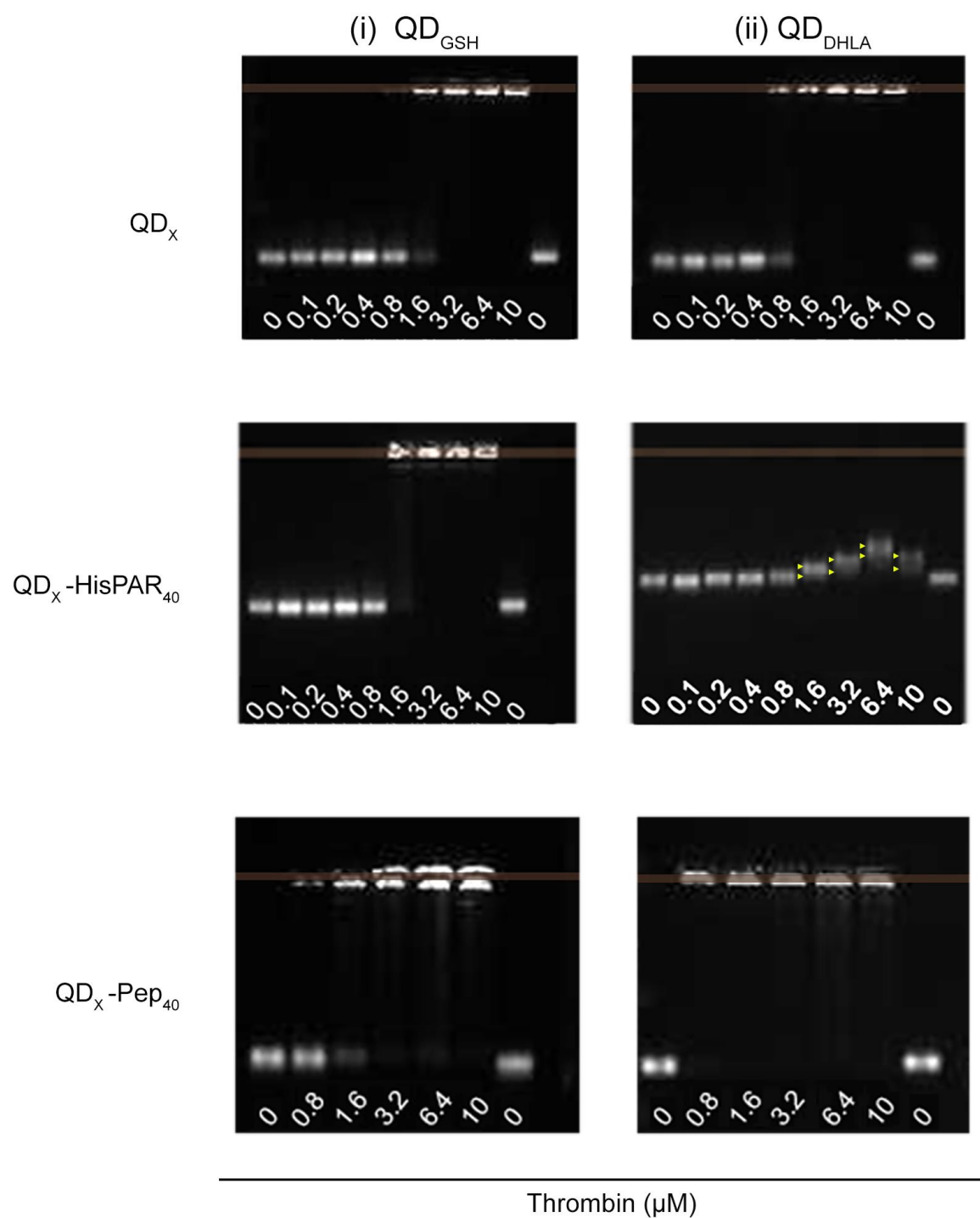


**Figure 3.10.** Agarose gel electrophoresis of  $QD_x$  (top row) and  $QD_x-[Y]_{40}$  where  $X = \text{GSH}$  or  $\text{DHLA}$ , and  $Y = \text{HisPAR}$  (middle), or  $\text{Pep}$  (bottom). Samples were incubated with various concentrations of thrombin (0.1–10  $\mu\text{M}$ ) to probe the tendency for thrombin to adsorb onto the surface of QDs and QD-conjugates. Arrows indicate the formation of discrete bands.

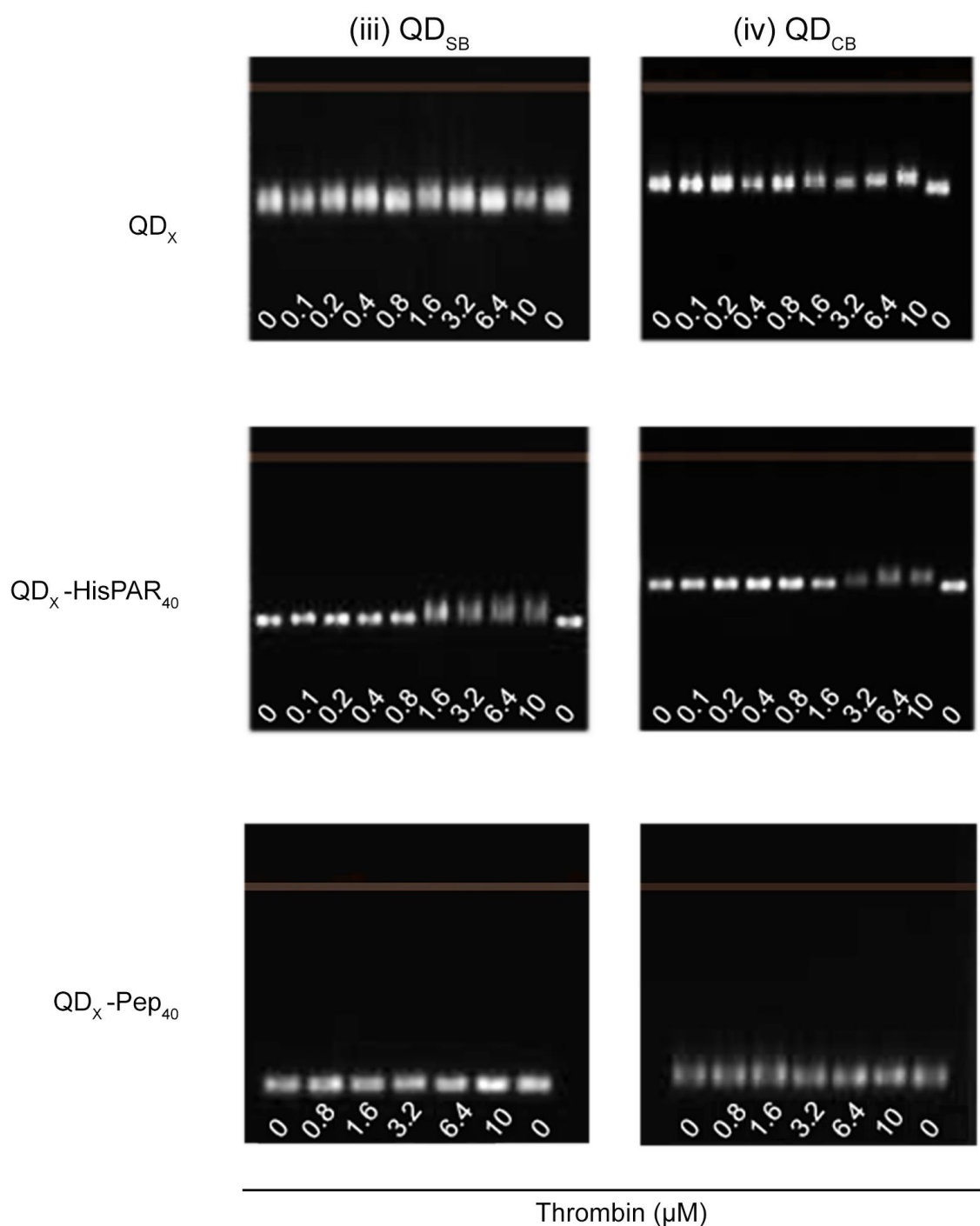


**Figure 3.11.** Agarose gel electrophoresis of QD<sub>x</sub> (top row) and QD<sub>x</sub>-[Y]<sub>40</sub> where X = SB or CB and Y = HisPAR (middle), or Pep (bottom). Samples were incubated with various concentrations of thrombin (0.1–10 μM) to probe the tendency for thrombin to adsorb onto the surface of QDs and QD-conjugates.

### 3.5 Conclusion

Thrombin activity on QD<sub>DHLA</sub>, QD<sub>GSH</sub>, QD<sub>Glc</sub>, QD<sub>SB</sub>, and QD<sub>CB</sub> was evaluated in the presence and absence of HisPAR, a peptide based on the PAR1 sequence that is known to allosterically interact with thrombin's exosite I. It was found that QD-conjugated HisPAR enhanced the initial rate of proteolysis for QD<sub>SB</sub> and QD<sub>CB</sub>, but not for QD<sub>DHLA</sub>, QD<sub>GSH</sub>, QD<sub>Glc</sub>. In addition, this enhancement was not seen when additional non-PAR1-based peptides were conjugated to the surface of QD nor when PAR1-based peptide was not conjugated onto the QD surface but instead was in the bulk solution. The enhancement was also not seen with trypsin, which shares similar proteolytic mechanism with thrombin, but does not have known interactions with the hirudin-like region of PAR1. The enhancement was observed in different QD nanocrystals, albeit with variations in the extent of the proteolytic enhancement. We postulate that the interactions between the zwitterionic QDs, thrombin, and HisPAR visualized via agarose gel electrophoresis are responsible for the enhancement of initial rate seen in the enzyme assays. This was further supported by assays with varied enzyme concentrations and constant substrate concentration. The results from these assays showed a plateau behaviour in the enhancement with increasing thrombin concentrations. The HisPAR effect on thrombin activity with zwitterionic QDs may originate from the similarity between the zwitterionic QD surface and the extracellular side of the mammalian cell membrane, which is rich in phospholipids with zwitterionic headgroups. The display of HisPAR on zwitterionic QDs is thus akin to its display on platelets, among other cells, and appears to impart thrombin with similar enhancement of activity on the QD scaffold.

Future work includes further exploring the use of zwitterionic QD surfaces as cellular surface mimics for enhanced sensing of other proteases. The minimal non-specific adsorption on QD<sub>SB</sub> and QD<sub>CB</sub> can also be exploited for sensing in more complex sample matrices, such as cells, whole blood, or plasma.

## Chapter 4 : Conclusions and Future Work

### 4.1 Thesis Overview

The work presented in this thesis highlights that QD surface chemistry as yet another important property that can be leveraged for QD applications. The thorough characterizations of the ligands synthesized, as well as the corresponding ligand-capped QDs, provide a solid foundation for future application of these QDs. Certain ligands, such as CB and SB, showed minimal nonspecific adsorption and they are promising ligands to be used in more complex matrices. Others showed superior pH stability over a wide range of pH (Glc and Ser), and another was only stable under alkaline conditions (API-Glc). These differences add another layer of complexity when choosing a hydrophilic ligand to render QD stable in aqueous solutions. Nonetheless, this complexity can become another tool in our toolkit when distinguishing between various analytes using these QD probes. Preliminary results with model proteases show that under the same conditions, different ligands are associated with a wide range of proteolytic rates, with 3-fold to 160-fold increase between the best and worst-performing QD conjugates. The variations in the enzyme behaviour on different ligand-coated QDs were unique to each enzyme tested, including thrombin, trypsin, and papain. Relative proteolytic rates on different ligand-coated QDs showed consistent trends that could be used to discriminate between these enzymes.

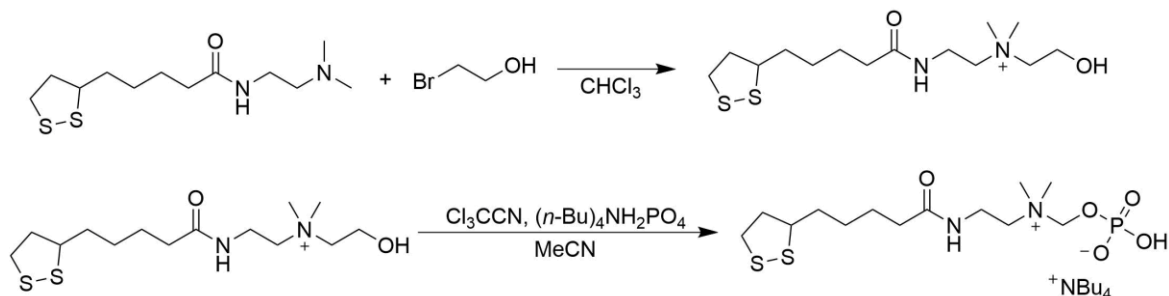
This thesis also provides an example of QD as a promising platform that can be modified with biomolecule to better mimic the biological environment. A sequence of PAR1, which is typically found on a cellular surface to facilitate thrombin-associated coagulation pathway through allosteric interactions, was shown to enhance thrombin activity when displayed on a QD-substrate conjugate. However, this enhancement is sensitive to the QD surface chemistry, i.e. ligand coating, and it was only observed with zwitterionic ligand-coated QDs which is likely because of their resemblance to the phospholipid-rich cellular surfaces. Experiments also showed that this enhancement only occurs on QD surface and it was not observed when the PAR1-based peptide was in the bulk solution. These QD conjugates demonstrated that allosteric interactions can be reproduced between a pair of synthetic nanomaterial and biomolecule and allosteric regulation with

biomolecules is another available strategy to increase the sensitivity and selectivity of our biosensors.

## 4.2 Future Outlook

As the preliminary results in Chapter 2 show, expanding the ligand library can be used to generate a fingerprint to distinguish between different enzymes. Further expansion of the ligand and substrate libraries can be combined to form a protease “nose” array. Similar to the olfactory receptors, the protease array would have a number of receptors, or QD probes, that can respond to a number of analytes and their combined signals could be used to distinguish the analytes through machine learning and spatial encoding. A sizeable array with about ten elements can be created, with substrate sequences containing different recognition residues and various ligand coatings, to distinguish and identify enzymes. Moving forward, other model proteases can be tested against various ligand-coated QDs such as subtilisin, plasmin, and elastase before assaying enzymes that are associated with pathological pathways.

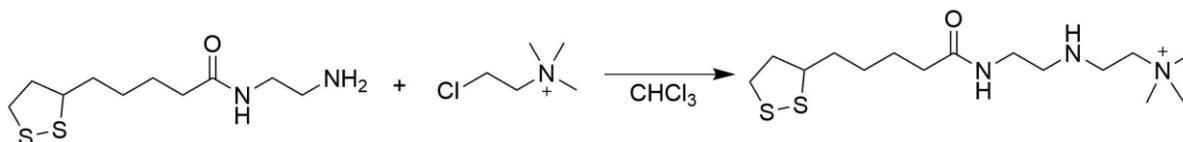
Some potential ligands of interest include a zwitterionic ligand with a terminal phosphate group. A possible synthetic scheme based on a procedure reported by Wessjohann *et al.* is shown in Scheme 3 [136].



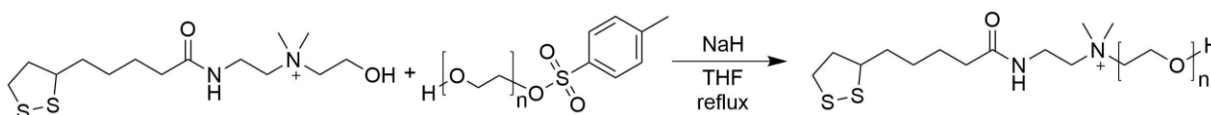
**Scheme 3.** Proposed synthetic scheme for phosphate-terminating zwitterionic LA.

All the ligands studied in this thesis were either anionic, zwitterionic, or neutral, and there is a lack of cationic ligands. As a QD ligand, tertiary amine-terminating DHLA (reduced compound **2**) ligand was previously reported to be associated with instability at higher pH range (pH > 8) and non-specific adsorption. These disadvantages could be ameliorated by the replacement of the

tertiary amine with a quaternary ammonium (Scheme 4) or both quaternary ammonium and PEG (Scheme 5). In addition, hydrophobic moiety-appended LA, although not ideal for colloidal stability, can be introduced as a charged species or with a PEG terminal group. Amino acids provide a wide variety of side chains and they can likely undergo conjugation in a similar manner as the serine-appended LA synthesized herein.



**Scheme 4.** Proposed synthetic scheme for quaternary ammonium terminating cationic LA.



**Scheme 5.** Proposed synthetic scheme for PEGylated quaternary ammonium terminating LA.

With the demonstration of proteolytic enhancement by conjugating a PAR1-based peptide onto the QD surface, it is conceivable that the display of other small molecules can be used to allosterically moderate enzyme activity. It would be interesting to study other biomolecules that are known to modulate thrombin activity, such as sulfated glycosaminoglycan (e.g. heparin). As well, other allosteric regulating small molecules that have been reported in bulk solutions can also be tested on the QD platform, such as the conjugation of outer-membrane peptide for the allosteric activation of a periplasmic *Escherichia coli* protease, DegS [137].

By optimizing the QD surface chemistry with model proteases and expanding the ligand and conjugating biomolecule libraries, more strategies can be developed to enhance the sensitivity and selectivity of QD probes. These results can also be applied to different aspects of QD applications, beyond protease probes. By demonstrating QD as a promising cellular surface mimic it is foreseeable that new nanotechnology designs will be developed to help bridge the gap between biology and synthetic nanotechnology.

## References

- (1) Roberti, M. J.; Morgan, M.; Menéndez, G.; Pietrasanta, L. I.; Jovin, T. M.; Jares-Erijman, E. A. Quantum Dots As Ultrasensitive Nanoactuators and Sensors of Amyloid Aggregation in Live Cells. *J. Am. Chem. Soc.* **2009**, *131*, 8102–8107.
- (2) Goldman, E. R.; Clapp, A. R.; Anderson, G. P.; Uyeda, H. T.; Mauro, J. M.; Medintz, I. L.; Mattoussi, H. Multiplexed Toxin Analysis Using Four Colors of Quantum Dot Fluororeagents. *Anal. Chem.* **2004**, *76*, 684–688.
- (3) Goldman, E. R.; Anderson, G. P.; Tran, P. T.; Mattoussi, H.; Charles, P. T.; Mauro, J. M. Conjugation of Luminescent Quantum Dots with Antibodies Using an Engineered Adaptor Protein To Provide New Reagents for Fluoroimmunoassays. *Anal. Chem.* **2002**, *74*, 841–847.
- (4) Courty, S.; Luccardini, C.; Bellaiche, Y.; Cappello, G.; Dahan, M. Tracking Individual Kinesin Motors in Living Cells Using Single Quantum-Dot Imaging. *Nano Lett.* **2006**, *6*, 1491–1495.
- (5) Ruan, G.; Agrawal, A.; Marcus, A. I.; Nie, S. Imaging and Tracking of Tat Peptide-Conjugated Quantum Dots in Living Cells: New Insights into Nanoparticle Uptake, Intracellular Transport, and Vesicle Shedding. *J. Am. Chem. Soc.* **2007**, *129*, 14759–14766.
- (6) Yezhelyev, M. V.; Qi, L.; O'Regan, R. M.; Nie, S.; Gao, X. Proton-Sponge Coated Quantum Dots for siRNA Delivery and Intracellular Imaging. *J. Am. Chem. Soc.* **2008**, *130*, 9006–9012.
- (7) Koshman, Y. E.; Waters, S. B.; Walker, L. A.; Los, T.; Tombe, P. de; Goldspink, P. H.; Russell, B. Delivery and Visualization of Proteins Conjugated to Quantum Dots in Cardiac Myocytes. *Journal of Molecular and Cellular Cardiology* **2008**, *45*, 853–856.
- (8) Alivisatos, A. P. Semiconductor Clusters, Nanocrystals, and Quantum Dots. *Science* **1996**, *271*, 933–937.
- (9) Alivisatos, A. P. Perspectives on the Physical Chemistry of Semiconductor Nanocrystals. *J. Phys. Chem.* **1996**, *100*, 13226–13239.
- (10) Algar, W. R.; Susumu, K.; Delehanty, J. B.; Medintz, I. L. Semiconductor Quantum Dots in Bioanalysis: Crossing the Valley of Death. *Anal. Chem.* **2011**, *83*, 8826–8837.
- (11) Petryayeva, E.; Algar, W. R.; Medintz, I. L. Quantum Dots in Bioanalysis: A Review of Applications across Various Platforms for Fluorescence Spectroscopy and Imaging. *Appl Spectrosc* **2013**, *67*, 215–252.
- (12) Medintz, I. L.; Uyeda, H. T.; Goldman, E. R.; Mattoussi, H. Quantum Dot Bioconjugates for Imaging, Labelling and Sensing. *Nature Materials* **2005**, *4*, 435–446.
- (13) Resch-Genger, U.; Grabolle, M.; Cavaliere-Jaricot, S.; Nitschke, R.; Nann, T. Quantum Dots versus Organic Dyes as Fluorescent Labels. *Nature Methods* **2008**, *5*, 763–775.
- (14) Qu, L.; Peng, X. Control of Photoluminescence Properties of CdSe Nanocrystals in Growth. *J. Am. Chem. Soc.* **2002**, *124*, 2049–2055.
- (15) Du, H.; Chen, C.; Krishnan, R.; Krauss, T. D.; Harbold, J. M.; Wise, F. W.; Thomas, M. G.; Silcox, J. Optical Properties of Colloidal PbSe Nanocrystals. *Nano Lett.* **2002**, *2*, 1321–1324.
- (16) Schlegel, G.; Bohnenberger, J.; Potapova, I.; Mews, A. Fluorescence Decay Time of Single Semiconductor Nanocrystals. *Phys. Rev. Lett.* **2002**, *88*, 137401.

- (17) Grecco H.E.; Lidke K.A.; Heintzmann R.; Lidke D.S.; Spagnuolo C.; Martinez O.E.; Jares-Erijman E.A.; Jovin T.M. Ensemble and Single Particle Photophysical Properties (Two-photon Excitation, Anisotropy, FRET, Lifetime, Spectral Conversion) of Commercial Quantum Dots in Solution and in Live Cells. *Microscopy Research and Technique* **2005**, *65*, 169–179.
- (18) Jones, M.; Nedeljkovic, J.; Ellingson, R. J.; Nozik, A. J.; Rumbles, G. Photoenhancement of Luminescence in Colloidal CdSe Quantum Dot Solutions. *J. Phys. Chem. B* **2003**, *107*, 11346–11352.
- (19) Peng, X.; Schlamp, M. C.; Kadavanich, A. V.; Alivisatos, A. P. Epitaxial Growth of Highly Luminescent CdSe/CdS Core/Shell Nanocrystals with Photostability and Electronic Accessibility. *J. Am. Chem. Soc.* **1997**, *119*, 7019–7029.
- (20) Yu, W. W.; Qu, L.; Guo, W.; Peng, X. Experimental Determination of the Extinction Coefficient of CdTe, CdSe, and CdS Nanocrystals. *Chem. Mater.* **2003**, *15*, 2854–2860.
- (21) Zhu, H.; Song, N.; Lian, T. Controlling Charge Separation and Recombination Rates in CdSe/ZnS Type I Core–Shell Quantum Dots by Shell Thicknesses. *J. Am. Chem. Soc.* **2010**, *132*, 15038–15045.
- (22) Kloepper, J. A.; Bradforth, S. E.; Nadeau, J. L. Photophysical Properties of Biologically Compatible CdSe Quantum Dot Structures. *J. Phys. Chem. B* **2005**, *109*, 9996–10003.
- (23) Talapin, D. V.; Mekis, I.; Götzinger, S.; Kornowski, A.; Benson, O.; Weller, H. CdSe/CdS/ZnS and CdSe/ZnSe/ZnS Core–Shell–Shell Nanocrystals. *J. Phys. Chem. B* **2004**, *108*, 18826–18831.
- (24) Talapin, D. V.; Koeppel, R.; Götzinger, S.; Kornowski, A.; Lupton, J. M.; Rogach, A. L.; Benson, O.; Feldmann, J.; Weller, H. Highly Emissive Colloidal CdSe/CdS Heterostructures of Mixed Dimensionality. *Nano Letters* **2003**, *3*, 1677–1681.
- (25) Swafford, L. A.; Weigand, L. A.; Bowers, M. J.; McBride, J. R.; Rapaport, J. L.; Watt, T. L.; Dixit, S. K.; Feldman, L. C.; Rosenthal, S. J. Homogeneously Alloyed Cd<sub>x</sub>Se<sub>1-x</sub> Nanocrystals: Synthesis, Characterization, and Composition/Size-Dependent Band Gap. *J. Am. Chem. Soc.* **2006**, *128*, 12299–12306.
- (26) Bailey, R. E.; Nie, S. Alloyed Semiconductor Quantum Dots: Tuning the Optical Properties without Changing the Particle Size. *J. Am. Chem. Soc.* **2003**, *125*, 7100–7106.
- (27) Murphy, C. J. Peer Reviewed: Optical Sensing with Quantum Dots. *Anal. Chem.* **2002**, *74*, 520 A–526 A.
- (28) Kim, S.; Fisher, B.; Eisler, H.-J.; Bawendi, M. Type-II Quantum Dots: CdTe/CdSe(Core/Shell) and CdSe/ZnTe(Core/Shell) Heterostructures. *J. Am. Chem. Soc.* **2003**, *125*, 11466–11467.
- (29) Green, M. The Nature of Quantum Dot Capping Ligands. *J. Mater. Chem.* **2010**, *20*, 5797–5809.
- (30) Sapsford, K. E.; Algar, W. R.; Berti, L.; Gemmill, K. B.; Casey, B. J.; Oh, E.; Stewart, M. H.; Medintz, I. L. Functionalizing Nanoparticles with Biological Molecules: Developing Chemistries That Facilitate Nanotechnology. *Chem. Rev.* **2013**, *113*, 1904–2074.
- (31) Parak, W. J.; Gerion, D.; Pellegrino, T.; Zanchet, D.; Micheel, C.; Williams, S. C.; Boudreau, R.; Gros, M. A. L.; Larabell, C. A.; Alivisatos, A. P. Biological Applications of Colloidal Nanocrystals. *Nanotechnology* **2003**, *14*, R15.
- (32) Díaz, S. A.; Sen, S.; Boeneman Gemmill, K.; Brown, C. W.; Oh, E.; Susumu, K.; Stewart, M. H.; Breger, J. C.; Lasarte Aragonés, G.; Field, L. D.; *et al.* Elucidating Surface Ligand-

- Dependent Kinetic Enhancement of Proteolytic Activity at Surface-Modified Quantum Dots. *ACS Nano* **2017**, *11*, 5884–5896.
- (33) Susumu, K.; Uyeda, H. T.; Medintz, I. L.; Pons, T.; Delehanty, J. B.; Mattoussi, H. Enhancing the Stability and Biological Functionalities of Quantum Dots via Compact Multifunctional Ligands. *J. Am. Chem. Soc.* **2007**, *129*, 13987–13996.
- (34) Zhan, N.; Palui, G.; Safi, M.; Ji, X.; Mattoussi, H. Multidentate Zwitterionic Ligands Provide Compact and Highly Biocompatible Quantum Dots. *J. Am. Chem. Soc.* **2013**, *135*, 13786–13795.
- (35) Gravel, E.; Tanguy, C.; Cassette, E.; Pons, T.; Knittel, F.; Bernardis, N.; Garofalakis, A.; Ducongé, F.; Dubertret, B.; Doris, E. Compact Tridentate Ligands for Enhanced Aqueous Stability of Quantum Dots and in Vivo Imaging. *Chem. Sci.* **2012**, *4*, 411–417.
- (36) Stewart, M. H.; Susumu, K.; Mei, B. C.; Medintz, I. L.; Delehanty, J. B.; Blanco-Canosa, J. B.; Dawson, P. E.; Mattoussi, H. Multidentate Poly(Ethylene Glycol) Ligands Provide Colloidal Stability to Semiconductor and Metallic Nanocrystals in Extreme Conditions. *J. Am. Chem. Soc.* **2010**, *132*, 9804–9813.
- (37) Jeong, S.; Achermann, M.; Nanda, J.; Ivanov, S.; Klimov, V. I.; Hollingsworth, J. A. Effect of the Thiol–Thiolate Equilibrium on the Photophysical Properties of Aqueous CdSe/ZnS Nanocrystal Quantum Dots. *J. Am. Chem. Soc.* **2005**, *127*, 10126–10127.
- (38) Gao, X.; Cui, Y.; Levenson, R. M.; Chung, L. W. K.; Nie, S. *In Vivo* Cancer Targeting and Imaging with Semiconductor Quantum Dots. *Nature Biotechnology* **2004**, *22*, 969–976.
- (39) Liu, W.; Greytak, A. B.; Lee, J.; Wong, C. R.; Park, J.; Marshall, L. F.; Jiang, W.; Curtin, P. N.; Ting, A. Y.; Nocera, D. G.; *et al.* Compact Biocompatible Quantum Dots via RAFT-Mediated Synthesis of Imidazole-Based Random Copolymer Ligand. *J. Am. Chem. Soc.* **2010**, *132*, 472–483.
- (40) Smith, A. M.; Nie, S. Minimizing the Hydrodynamic Size of Quantum Dots with Multifunctional Multidentate Polymer Ligands. *J. Am. Chem. Soc.* **2008**, *130*, 11278–11279.
- (41) Wang, C.-W.; Moffitt, M. G. Surface-Tunable Photoluminescence from Block Copolymer-Stabilized Cadmium Sulfide Quantum Dots. *Langmuir* **2004**, *20*, 11784–11796.
- (42) Mulvaney, P.; M. Liz-Marzán, L.; Giersig, M.; Ung, T. Silica Encapsulation of Quantum Dots and Metal Clusters. *Journal of Materials Chemistry* **2000**, *10*, 1259–1270.
- (43) Hu, X.; Gao, X. Silica–Polymer Dual Layer-Encapsulated Quantum Dots with Remarkable Stability. *ACS Nano* **2010**, *4*, 6080–6086.
- (44) Ma, Y.; Li, Y.; Ma, S.; Zhong, X. Highly Bright Water-Soluble Silica Coated Quantum Dots with Excellent Stability. *J. Mater. Chem. B* **2014**, *2*, 5043–5051.
- (45) Gerion, D.; Pinaud, F.; Williams, S. C.; Parak, W. J.; Zanchet, D.; Weiss, S.; Alivisatos, A. P. Synthesis and Properties of Biocompatible Water-Soluble Silica-Coated CdSe/ZnS Semiconductor Quantum Dots. *J. Phys. Chem. B* **2001**, *105*, 8861–8871.
- (46) Yang, H.; Holloway, P. H.; Santra, S. Water-Soluble Silica-Overcoated CdS:Mn/ZnS Semiconductor Quantum Dots. *The Journal of Chemical Physics* **2004**, *121*, 7421–7426.
- (47) Wu, L.; Guo, Q.-S.; Liu, Y.-Q.; Sun, Q.-J. Fluorescence Resonance Energy Transfer-Based Ratiometric Fluorescent Probe for Detection of Zn<sup>2+</sup> Using a Dual-Emission Silica-Coated Quantum Dots Mixture. *Anal. Chem.* **2015**, *87*, 5318–5323.

- (48) Algar, W. R.; Krull, U. J. Developing Mixed Films of Immobilized Oligonucleotides and Quantum Dots for the Multiplexed Detection of Nucleic Acid Hybridization Using a Combination of Fluorescence Resonance Energy Transfer and Direct Excitation of Fluorescence. *Langmuir* **2010**, *26*, 6041–6047.
- (49) Massey, M.; Algar, W. R.; Krull, U. J. Fluorescence Resonance Energy Transfer (FRET) for DNA Biosensors: FRET Pairs and Förster Distances for Various Dye–DNA Conjugates. *Analytica Chimica Acta* **2006**, *568*, 181–189.
- (50) Jennings, T. L.; Becker-Catania, S. G.; Triulzi, R. C.; Tao, G.; Scott, B.; Sapsford, K. E.; Spindel, S.; Oh, E.; Jain, V.; Delehanty, J. B.; *et al.* Reactive Semiconductor Nanocrystals for Chemoselective Biolabeling and Multiplexed Analysis. *ACS Nano* **2011**, *5*, 5579–5593.
- (51) Wu, X.; Liu, H.; Liu, J.; Haley, K. N.; Treadway, J. A.; Larson, J. P.; Ge, N.; Peale, F.; Bruchez, M. P. Immunofluorescent Labeling of Cancer Marker Her2 and Other Cellular Targets with Semiconductor Quantum Dots. *Nature Biotechnology* **2003**, *21*, 41–46.
- (52) Prasuhn, D. E.; Blanco-Canosa, J. B.; Vora, G. J.; Delehanty, J. B.; Susumu, K.; Mei, B. C.; Dawson, P. E.; Medintz, I. L. Combining Chemoselective Ligation with Polyhistidine-Driven Self-Assembly for the Modular Display of Biomolecules on Quantum Dots. *ACS Nano* **2010**, *4*, 267–278.
- (53) Medintz, I. L.; Clapp, A. R.; Mattoussi, H.; Goldman, E. R.; Fisher, B.; Mauro, J. M. Self-Assembled Nanoscale Biosensors Based on Quantum Dot FRET Donors. *Nature Materials* **2003**, *2*, 630–638.
- (54) Yu, M.; Yang, Y.; Han, R.; Zheng, Q.; Wang, L.; Hong, Y.; Li, Z.; Sha, Y. Polyvalent Lactose–Quantum Dot Conjugate for Fluorescent Labeling of Live Leukocytes. *Langmuir* **2010**, *26*, 8534–8539.
- (55) Algar, W. R.; Prasuhn, D. E.; Stewart, M. H.; Jennings, T. L.; Blanco-Canosa, J. B.; Dawson, P. E.; Medintz, I. L. The Controlled Display of Biomolecules on Nanoparticles: A Challenge Suited to Bioorthogonal Chemistry. *Bioconjugate Chem.* **2011**, *22*, 825–858.
- (56) Rosenthal, S. J.; Chang, J. C.; Kovtun, O.; McBride, J. R.; Tomlinson, I. D. Biocompatible Quantum Dots for Biological Applications. *Chem Biol* **2011**, *18*, 10–24.
- (57) Optical and Photochemical Properties of Nonstoichiometric Cadmium Sulfide Nanoparticles: Surface Modification with Copper(II) Ions - *Langmuir* (ACS Publications) <https://pubs-acsc-org.ezproxy.library.ubc.ca/doi/abs/10.1021/la960985r> (accessed Apr 16, 2018).
- (58) Sletten, E. M.; Bertozzi, C. R. A Hydrophilic Azacyclooctyne for Cu-Free Click Chemistry. *Org. Lett.* **2008**, *10*, 3097–3099.
- (59) Bernardin, A.; Cazet, A.; Guyon, L.; Delannoy, P.; Vinet, F.; Bonnaffé, D.; Texier, I. Copper-Free Click Chemistry for Highly Luminescent Quantum Dot Conjugates: Application to in Vivo Metabolic Imaging. *Bioconjugate Chem.* **2010**, *21*, 583–588.
- (60) Schieber Christine; Bestetti Alessandra; Lim Jet Phey; Ryan Anneke D.; Nguyen Tich-Lam; Eldridge Robert; White Anthony R.; Gleeson Paul A.; Donnelly Paul S.; Williams Spencer J.; *et al.* Conjugation of Transferrin to Azide-Modified CdSe/ZnS Core–Shell Quantum Dots Using Cyclooctyne Click Chemistry. *Angewandte Chemie International Edition* **2012**, *51*, 10523–10527.

- (61) Han, H.-S.; Devaraj, N. K.; Lee, J.; Hilderbrand, S. A.; Weissleder, R.; Bawendi, M. G. Development of a Bioorthogonal and Highly Efficient Conjugation Method for Quantum Dots Using Tetrazine–Norbornene Cycloaddition. *J. Am. Chem. Soc.* **2010**, *132*, 7838–7839.
- (62) Han, H.-S.; Niemeyer, E.; Huang, Y.; Kamoun, W. S.; Martin, J. D.; Bhaumik, J.; Chen, Y.; Roberge, S.; Cui, J.; Martin, M. R.; *et al.* Quantum Dot/Antibody Conjugates for in Vivo Cytometric Imaging in Mice. *PNAS* **2015**, *112*, 1350–1355.
- (63) Savla, R.; Taratula, O.; Garbuzenko, O.; Minko, T. Tumor Targeted Quantum Dot-Mucin 1 Aptamer-Doxorubicin Conjugate for Imaging and Treatment of Cancer. *Journal of Controlled Release* **2011**, *153*, 16–22.
- (64) Delehanty, J. B.; Blanco-Canosa, J. B.; Bradburne, C. E.; Susumu, K.; Stewart, M. H.; Prasuhn, D. E.; Dawson, P. E.; Medintz, I. L. Site-Specific Cellular Delivery of Quantum Dots with Chemoselectively-Assembled Modular Peptides. *Chem. Commun.* **2013**, *49*, 7878–7880.
- (65) Liu, A.; Peng, S.; Soo, J. C.; Kuang, M.; Chen, P.; Duan, H. Quantum Dots with Phenylboronic Acid Tags for Specific Labeling of Sialic Acids on Living Cells. *Anal. Chem.* **2011**, *83*, 1124–1130.
- (66) Sang, L.-J.; Wang, H.-F. Aminophenylboronic-Acid-Conjugated Polyacrylic Acid–Mn-Doped ZnS Quantum Dot for Highly Sensitive Discrimination of Glycoproteins. *Anal. Chem.* **2014**, *86*, 5706–5712.
- (67) Freeman, R.; Finder, T.; Bahshi, L.; Willner, I.  $\beta$ -Cyclodextrin-Modified CdSe/ZnS Quantum Dots for Sensing and Chiroselective Analysis. *Nano Lett.* **2009**, *9*, 2073–2076.
- (68) Sapsford, K. E.; Pons, T.; Medintz, I. L.; Higashiya, S.; Brunel, F. M.; Dawson, P. E.; Mattoussi, H. Kinetics of Metal-Affinity Driven Self-Assembly between Proteins or Peptides and CdSe–ZnS Quantum Dots. *J. Phys. Chem. C* **2007**, *111*, 11528–11538.
- (69) Friguet, B.; Chaffotte, A. F.; Djavadi-Ohanian, L.; Goldberg, M. E. Measurements of the True Affinity Constant in Solution of Antigen-Antibody Complexes by Enzyme-Linked Immunosorbent Assay. *Journal of Immunological Methods* **1985**, *77*, 305–319.
- (70) Roullier, V.; Clarke, S.; You, C.; Pinaud, F.; Gouzer, G.; Schaible, D.; Marchi-Artzner, V.; Piehler, J.; Dahan, M. High-Affinity Labeling and Tracking of Individual Histidine-Tagged Proteins in Live Cells Using Ni<sup>2+</sup> Tris-Nitrilotriacetic Acid Quantum Dot Conjugates. *Nano Lett.* **2009**, *9*, 1228–1234.
- (71) Susumu, K.; Medintz, I. L.; Delehanty, J. B.; Boeneman, K.; Mattoussi, H. Modification of Poly(Ethylene Glycol)-Capped Quantum Dots with Nickel Nitrilotriacetic Acid and Self-Assembly with Histidine-Tagged Proteins. *J. Phys. Chem. C* **2010**, *114*, 13526–13531.
- (72) Yao Hequan; Zhang Yan; Xiao Fei; Xia Zuyong; Rao Jianghong. Quantum Dot/Bioluminescence Resonance Energy Transfer Based Highly Sensitive Detection of Proteases. *Angewandte Chemie International Edition* **2007**, *46*, 4346–4349.
- (73) Peng, H.; Zhang, L.; Kjällman, T. H. M.; Soeller, C. DNA Hybridization Detection with Blue Luminescent Quantum Dots and Dye-Labeled Single-Stranded DNA. *J. Am. Chem. Soc.* **2007**, *129*, 3048–3049.
- (74) Mattoussi, H.; Mauro, J. M.; Goldman, E. R.; Anderson, G. P.; Sundar, V. C.; Mikulec, F. V.; Bawendi, M. G. Self-Assembly of CdSe–ZnS Quantum Dot Bioconjugates Using an Engineered Recombinant Protein. *J. Am. Chem. Soc.* **2000**, *122*, 12142–12150.

- (75) Ji, X.; Zheng, J.; Xu, J.; Rastogi, V. K.; Cheng, T.-C.; DeFrank, J. J.; Leblanc, R. M. (CdSe)ZnS Quantum Dots and Organophosphorus Hydrolase Bioconjugate as Biosensors for Detection of Paraoxon. *J. Phys. Chem. B* **2005**, *109*, 3793–3799.
- (76) Walther, C.; Meyer, K.; Rennert, R.; Neundorff, I. Quantum Dot–Carrier Peptide Conjugates Suitable for Imaging and Delivery Applications. *Bioconjugate Chem.* **2008**, *19*, 2346–2356.
- (77) Green, N. M. Avidin. 1. The Use of [14C]Biotin for Kinetic Studies and for Assay. *Biochem J* **1963**, *89*, 585–591.
- (78) Jaiswal, J. K.; Mattoussi, H.; Mauro, J. M.; Simon, S. M. Long-Term Multiple Color Imaging of Live Cells Using Quantum Dot Bioconjugates. *Nature Biotechnology* **2003**, *21*, 47–51.
- (79) Goldman, E. R.; Balighian, E. D.; Mattoussi, H.; Kuno, M. K.; Mauro, J. M.; Tran, P. T.; Anderson, G. P. Avidin: A Natural Bridge for Quantum Dot–Antibody Conjugates. *J. Am. Chem. Soc.* **2002**, *124*, 6378–6382.
- (80) Han, M.; Gao, X.; Su, J. Z.; Nie, S. Quantum-Dot-Tagged Microbeads for Multiplexed Optical Coding of Biomolecules. *Nature Biotechnology* **2001**, *19*, 631–635.
- (81) Medintz, I. L.; Pons, T.; Delehanty, J. B.; Susumu, K.; Brunel, F. M.; Dawson, P. E.; Mattoussi, H. Intracellular Delivery of Quantum Dot–Protein Cargos Mediated by Cell Penetrating Peptides. *Bioconjugate Chem.* **2008**, *19*, 1785–1795.
- (82) Zhang Ming-Zhen; Yu Yong; Yu Rong-Na; Wan Min; Zhang Rong-Ying; Zhao Yuan-Di. Tracking the Down-Regulation of Folate Receptor- $\alpha$  in Cancer Cells through Target Specific Delivery of Quantum Dots Coupled with Antisense Oligonucleotide and Targeted Peptide. *Small* **2013**, *9*, 4183–4193.
- (83) Valeur, B.; Berberan-Santos, M. N. *Molecular Fluorescence: Principles and Applications*; John Wiley & Sons, 2012.
- (84) Kasha, M. Characterization of Electronic Transitions in Complex Molecules. *Discuss. Faraday Soc.* **1950**, *9*, 14–19.
- (85) Lakowicz, J. R. *Principles of Fluorescence Spectroscopy*; 3rd ed.; Springer US, 2006.
- (86) Skoog, D. A.; Crouch, S. R.; Holler, F. J. *Principles of Instrumental Analysis*; Thomson Brooks/Cole: Belmont, CA, 2007.
- (87) Maeda, H.; Matsuno, H.; Ushida, M.; Katayama, K.; Saeki, K.; Itoh, N. 2,4-Dinitrobenzenesulfonyl Fluoresceins as Fluorescent Alternatives to Ellman’s Reagent in Thiol-Quantification Enzyme Assays. *Angewandte Chemie International Edition* **2005**, *44*, 2922–2925.
- (88) Karousos, N. G.; Aouabdi, S.; Way, A. S.; Reddy, S. M. Quartz Crystal Microbalance Determination of Organophosphorus and Carbamate Pesticides. *Analytica Chimica Acta* **2002**, *469*, 189–196.
- (89) Shan, C.; Yang, H.; Song, J.; Han, D.; Ivaska, A.; Niu, L. Direct Electrochemistry of Glucose Oxidase and Biosensing for Glucose Based on Graphene. *Anal. Chem.* **2009**, *81*, 2378–2382.
- (90) Qhobosheane, M.; Santra, S.; Zhang, P.; Tan, W. Biochemically Functionalized Silica Nanoparticles. *Analyst* **2001**, *126*, 1274–1278.
- (91) Glickman, J. F. Assay Development for Protein Kinase Enzymes. In *Assay Guidance Manual*; Sittampalam, G. S.; Coussens, N. P.; Brimacombe, K.; Grossman, A.; Arkin, M.; Auld, D.;

- Austin, C.; Baell, J.; Bejcek, B.; Chung, T. D. Y.; *et al.*, Eds.; Eli Lilly & Company and the National Center for Advancing Translational Sciences: Bethesda (MD), 2004.
- (92) Veeramani, S.; Yuan, T.-C.; Chen, S.-J.; Lin, F.-F.; Petersen, J. E.; Shaheduzzaman, S.; Srivastava, S.; MacDonald, R. G.; Lin, M.-F. Cellular Prostatic Acid Phosphatase: A Protein Tyrosine Phosphatase Involved in Androgen-Independent Proliferation of Prostate Cancer. *Endocr Relat Cancer* **2005**, *12*, 805–822.
- (93) Wada, N.; Fujisaki, M.; Ishii, S.; Ikeda, T.; Kitajima, M. Evaluation of Bone Metabolic Markers in Breast Cancer with Bone Metastasis. *Breast Cancer* **2001**, *8*, 131–137.
- (94) Kato, G. J.; McGowan, V.; Machado, R. F.; Little, J. A.; Taylor, J.; Morris, C. R.; Nichols, J. S.; Wang, X.; Poljakovic, M.; Morris, S. M.; *et al.* Lactate Dehydrogenase as a Biomarker of Hemolysis-Associated Nitric Oxide Resistance, Priapism, Leg Ulceration, Pulmonary Hypertension, and Death in Patients with Sickle Cell Disease. *Blood* **2006**, *107*, 2279–2285.
- (95) Schomburg, I.; Chang, A.; Schomburg, D. Standardization in Enzymology—Data Integration in the World’s Enzyme Information System BRENDA. *Perspectives in Science* **2014**, *1*, 15–23.
- (96) Goll, D. E.; Thompson, V. F.; Li, H.; Wei, W.; Cong, J. The Calpain System. *Physiological Reviews* **2003**, *83*, 731–801.
- (97) Elmore, S. Apoptosis: A Review of Programmed Cell Death. *Toxicol Pathol* **2007**, *35*, 495–516.
- (98) Nakagawa, T.; Zhu, H.; Morishima, N.; Li, E.; *al, et.* Caspase-12 Mediates Endoplasmic-Reticulum-Specific Apoptosis and Cytotoxicity by Amyloid-Beta. *Nature; London* **2000**, *403*, 98–103.
- (99) Arora, P.; Ricks, T. K.; Trejo, J. Protease-Activated Receptor Signalling, Endocytic Sorting and Dysregulation in Cancer. *Journal of Cell Science* **2007**, *120*, 921–928.
- (100) Briggs, G. E.; Haldane, J. B. S. A Note on the Kinetics of Enzyme Action. *Biochem J* **1925**, *19*, 338–339.
- (101) Díaz, S. A.; Malonoski, A. P.; Susumu, K.; Hofele, R. V.; Oh, E.; Medintz, I. L. Probing the Kinetics of Quantum Dot-Based Proteolytic Sensors. *Anal Bioanal Chem* **2015**, *407*, 7307–7318.
- (102) Medintz, I. L.; Clapp, A. R.; Brunel, F. M.; Tiefenbrunn, T.; Tetsuo Uyeda, H.; Chang, E. L.; Deschamps, J. R.; Dawson, P. E.; Mattoussi, H. Proteolytic Activity Monitored by Fluorescence Resonance Energy Transfer through Quantum-Dot–Peptide Conjugates. *Nature Materials* **2006**, *5*, 581–589.
- (103) Algar, W. R.; Malonoski, A.; Deschamps, J. R.; Blanco-Canosa, J. B.; Susumu, K.; Stewart, M. H.; Johnson, B. J.; Dawson, P. E.; Medintz, I. L. Proteolytic Activity at Quantum Dot-Conjugates: Kinetic Analysis Reveals Enhanced Enzyme Activity and Localized Interfacial “Hopping.” *Nano Lett.* **2012**, *12*, 3793–3802.
- (104) Petryayeva, E.; Jeen, T.; Algar, W. R. Optimization and Changes in the Mode of Proteolytic Turnover of Quantum Dot–Peptide Substrate Conjugates through Moderation of Interfacial Adsorption. *ACS Appl Mater Interfaces* **2017**, *9*, 30359–30372.
- (105) Wu, M.; Petryayeva, E.; Algar, W. R. Quantum Dot-Based Concentric FRET Configuration for the Parallel Detection of Protease Activity and Concentration. *Anal. Chem.* **2014**, *86*, 11181–11188.

- (106) Wu, M.; Algar, W. R. Acceleration of Proteolytic Activity Associated with Selection of Thiol Ligand Coatings on Quantum Dots. *ACS Appl. Mater. Interfaces* **2015**, *7*, 2535–2545.
- (107) Li, J. J.; Wang, Y. A.; Guo, W.; Keay, J. C.; Mishima, T. D.; Johnson, M. B.; Peng, X. Large-Scale Synthesis of Nearly Monodisperse CdSe/CdS Core/Shell Nanocrystals Using Air-Stable Reagents via Successive Ion Layer Adsorption and Reaction. *J. Am. Chem. Soc.* **2003**, *125*, 12567–12575.
- (108) Yu, W. W.; Peng, X. Formation of High-Quality CdS and Other II–VI Semiconductor Nanocrystals in Noncoordinating Solvents: Tunable Reactivity of Monomers. *Angewandte Chemie International Edition* **41**, 2368–2371.
- (109) Pons, T.; Uyeda, H. T.; Medintz, I. L.; Mattoussi, H. Hydrodynamic Dimensions, Electrophoretic Mobility, and Stability of Hydrophilic Quantum Dots. *J. Phys. Chem. B* **2006**, *110*, 20308–20316.
- (110) Park, S.; Sinha, N.; Hamad-Schifferli, K. Effective Size and Zeta Potential of Nanorods by Ferguson Analysis. *Langmuir* **2010**, *26*, 13071–13075.
- (111) Sjöback, R.; Nygren, J.; Kubista, M. Absorption and Fluorescence Properties of Fluorescein. *Spectrochimica Acta Part A: Molecular and Biomolecular Spectroscopy* **1995**, *51*, L7–L21.
- (112) Weers, J. G.; Rathman, J. F.; Axe, F. U.; Crichlow, C. A.; Foland, L. D.; Scheuing, D. R.; Wiersema, R. J.; Zielske, A. G. Effect of the Intramolecular Charge Separation Distance on the Solution Properties of Betaines and Sulfobetaines. *Langmuir* **1991**, *7*, 854–867.
- (113) Petryayeva, E.; Jeen, T.; Algar, W. R. Optimization and Changes in the Mode of Proteolytic Turnover of Quantum Dot–Peptide Substrate Conjugates through Moderation of Interfacial Adsorption. *ACS Appl. Mater. Interfaces* **2017**, *9*, 30359–30372.
- (114) Benito-Alifonso, D.; Tremel, S.; Hou, B.; Lockyear, H.; Mantell, J.; Fermin, D. J.; Verkade, P.; Berry, M.; Galan, M. C. Lactose as a “Trojan Horse” for Quantum Dot Cell Transport. *Angew Chem Int Ed Engl* **2014**, *53*, 810–814.
- (115) Song, C. K.; Jung, S. H.; Kim, D.-D.; Jeong, K.-S.; Shin, B. C.; Seong, H. Disaccharide-Modified Liposomes and Their in Vitro Intracellular Uptake. *International Journal of Pharmaceutics* **2009**, *380*, 161–169.
- (116) Jiang, J.; Oberdörster, G.; Biswas, P. Characterization of Size, Surface Charge, and Agglomeration State of Nanoparticle Dispersions for Toxicological Studies. *J Nanopart Res* **2009**, *11*, 77–89.
- (117) Linder, D. P.; Rodgers, K. R. A Theoretical Study of Imidazole- and Thiol-Based Zinc Binding Groups Relevant to Inhibition of Metzincins. *J. Phys. Chem. B* **2004**, *108*, 13839–13849.
- (118) Coughlin, S. R. Protease-Activated Receptors in Hemostasis, Thrombosis and Vascular Biology. *Journal of Thrombosis and Haemostasis* **2005**, *3*, 1800–1814.
- (119) Davie, E. W.; Kulman, J. D. An Overview of the Structure and Function of Thrombin. *Semin Thromb Hemost* **2006**, *32*, 003–015.
- (120) Rydel, T. J.; Ravichandran, K. G.; Tulinsky, A.; Bode, W.; Huber, R.; Roitsch, C.; Fenton, J. W. The Structure of a Complex of Recombinant Heparin and Human  $\alpha$ -Thrombin. *Science* **1990**, *249*, 277–280.
- (121) Gandhi, P. S.; Chen, Z.; Mathews, F. S.; Cera, E. D. Structural Identification of the Pathway of Long-Range Communication in an Allosteric Enzyme. *PNAS* **2008**, *105*, 1832–1837.
- (122) Wheaton, V. I.; Hung, D. T.; al, et. Domains Specifying Thrombin-Receptor Interaction. *Nature; London* **1991**, *353*, 674–677.

- (123) Jacques, S. L.; LeMasurier, M.; Sheridan, P. J.; Seeley, S. K.; Kuliopulos, A. Substrate-Assisted Catalysis of the PAR1 Thrombin Receptor ENHANCEMENT OF MACROMOLECULAR ASSOCIATION AND CLEAVAGE. *J. Biol. Chem.* **2000**, *275*, 40671–40678.
- (124) Jabaiah, A. M.; Getz, J. A.; Witkowski, W. A.; Hardy, J. A.; Daugherty, P. S. Identifi Cation of Protease Exosite-Interacting Peptides That Enhance Substrate Cleavage Kinetics. *bchm* **2012**, *393*, 933–941.
- (125) Liu, L. W.; Vu, T. K.; Esmon, C. T.; Coughlin, S. R. The Region of the Thrombin Receptor Resembling Hirudin Binds to Thrombin and Alters Enzyme Specificity. *J. Biol. Chem.* **1991**, *266*, 16977–16980.
- (126) Waugh, D. S. An Overview of Enzymatic Reagents for the Removal of Affinity Tags. *Protein Expression and Purification* **2011**, *80*, 283–293.
- (127) Algar, W. R.; Blanco-Canosa, J. B.; Manthe, R. L.; Susumu, K.; Stewart, M. H.; Dawson, P. E.; Medintz, I. L. Synthesizing and Modifying Peptides for Chemoselective Ligation and Assembly into Quantum Dot-Peptide Bioconjugates. *Methods Mol. Biol.* **2013**, *1025*, 47–73.
- (128) Artimo, P.; Jonnalagedda, M.; Arnold, K.; Baratin, D.; Csardi, G.; de Castro, E.; Duvaud, S.; Flegel, V.; Fortier, A.; Gasteiger, E.; *et al.* ExpASY: SIB Bioinformatics Resource Portal. *Nucleic Acids Res* **2012**, *40*, W597–W603.
- (129) Pons, T.; Medintz, I. L.; Wang, X.; English, D. S.; Mattoussi, H. Solution-Phase Single Quantum Dot Fluorescence Resonance Energy Transfer. *J. Am. Chem. Soc.* **2006**, *128*, 15324–15331.
- (130) Vu, T.-K. H.; Hung, D. T.; Wheaton, V. I.; Coughlin, S. R. Molecular Cloning of a Functional Thrombin Receptor Reveals a Novel Proteolytic Mechanism of Receptor Activation. *Cell* **1991**, *64*, 1057–1068.
- (131) Wu, M.; Algar, W. R. Acceleration of Proteolytic Activity Associated with Selection of Thiol Ligand Coatings on Quantum Dots <https://pubs.acs.org/doi/suppl/10.1021/am507466b> (accessed May 16, 2018).
- (132) Holmlin, R. E.; Chen, X.; Chapman, R. G.; Takayama, S.; Whitesides, G. M. Zwitterionic SAMs That Resist Nonspecific Adsorption of Protein from Aqueous Buffer. *Langmuir* **2001**, *17*, 2841–2850.
- (133) Chen, S.; Li, L.; Zhao, C.; Zheng, J. Surface Hydration: Principles and Applications toward Low-Fouling/Nonfouling Biomaterials. *Polymer* **2010**, *51*, 5283–5293.
- (134) Hower, J. C.; Bernardis, M. T.; Chen, S.; Tsao, H.-K.; Sheng, Y.-J.; Jiang, S. Hydration of “Nonfouling” Functional Groups. *J. Phys. Chem. B* **2009**, *113*, 197–201.
- (135) Schlenoff, J. B. Zwitteration: Coating Surfaces with Zwitterionic Functionality to Reduce Nonspecific Adsorption. *Langmuir* **2014**, *30*, 9625–9636.
- (136) Lira, L. M.; Vasilev, D.; Pilli, R. A.; Wessjohann, L. A. One-Pot Synthesis of Organophosphate Monoesters from Alcohols. *Tetrahedron Letters* **2013**, *54*, 1690–1692.
- (137) Mauldin, R. V.; Sauer, R. T. Allosteric Regulation of DegS Protease Subunits Though a Shared Energy Landscape. *Nat Chem Biol* **2013**, *9*, 90–96.

# Appendix

## 1. NMR Spectra

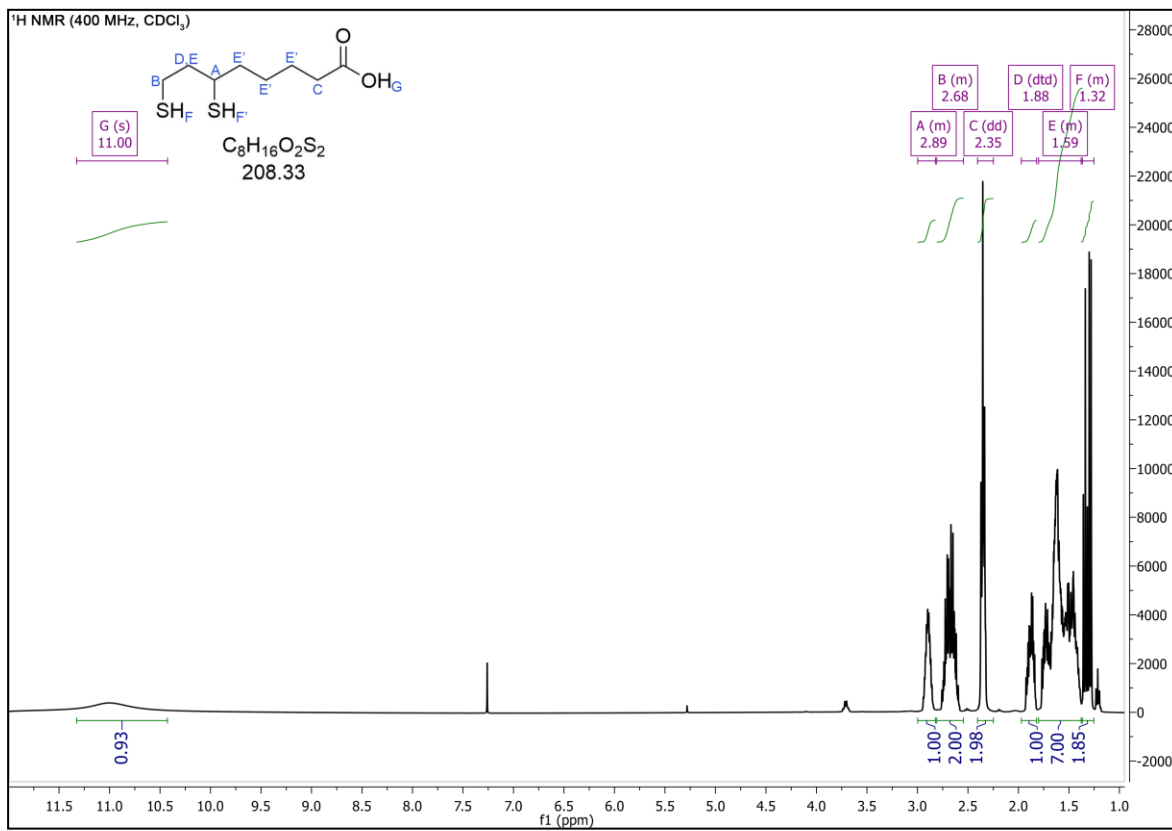
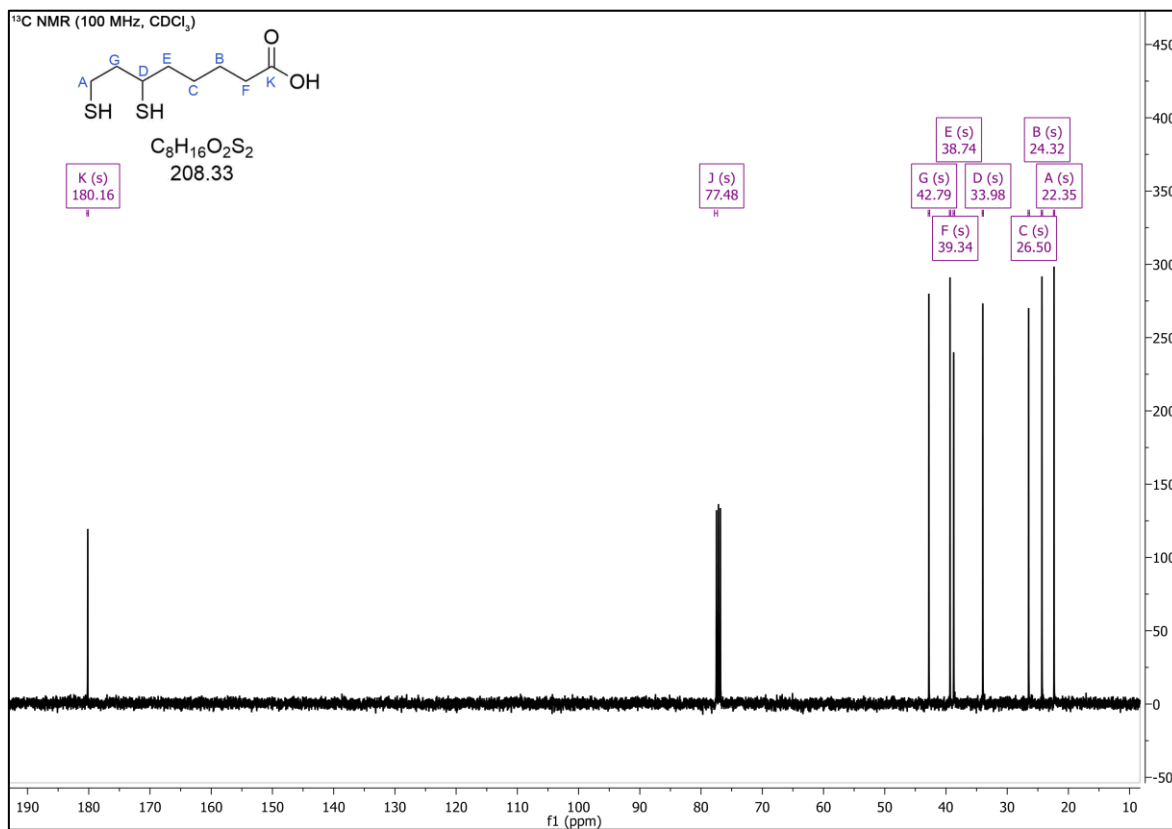
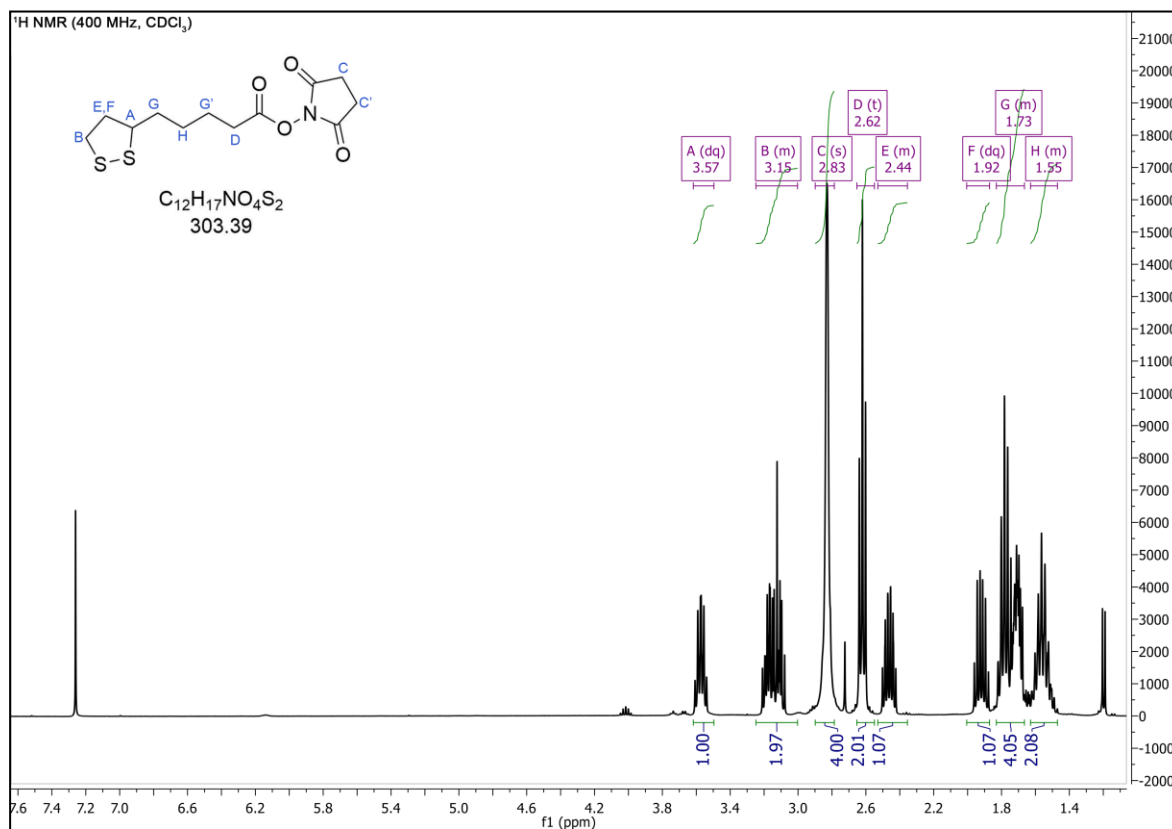


Figure A1. <sup>1</sup>H NMR spectrum of DHLA.



**Figure A2.** <sup>13</sup>C NMR spectrum of DHLA.



**Figure A3.** <sup>1</sup>H NMR spectrum of LA-NHS.

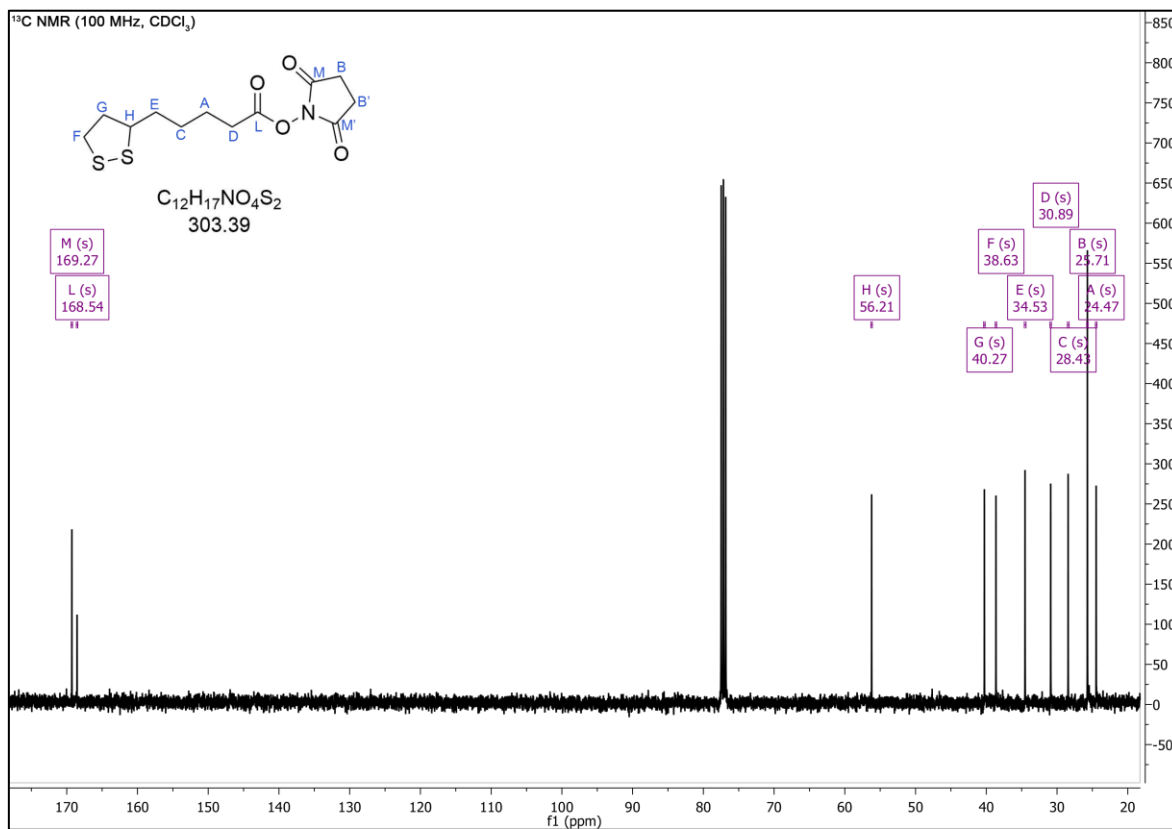


**Figure A4.** <sup>13</sup>C NMR spectrum of LA-NHS.

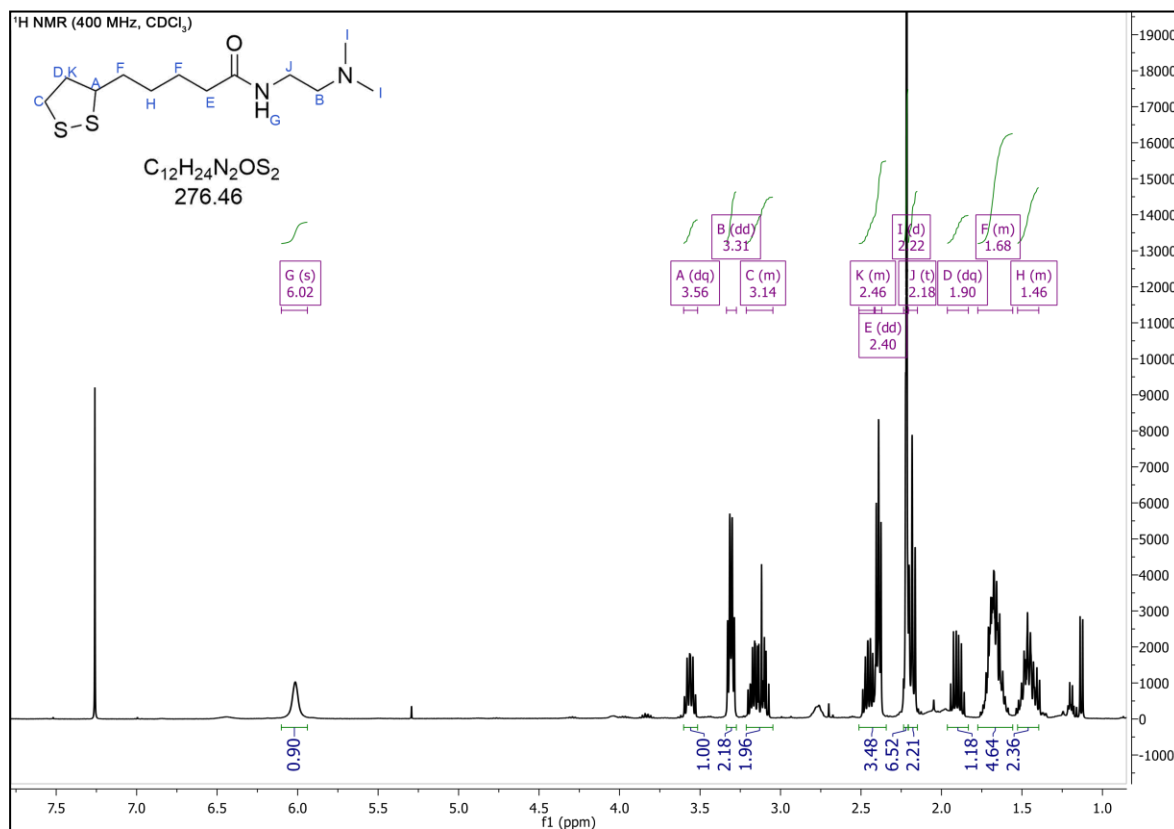


Figure A5. <sup>1</sup>H NMR spectrum of 2.

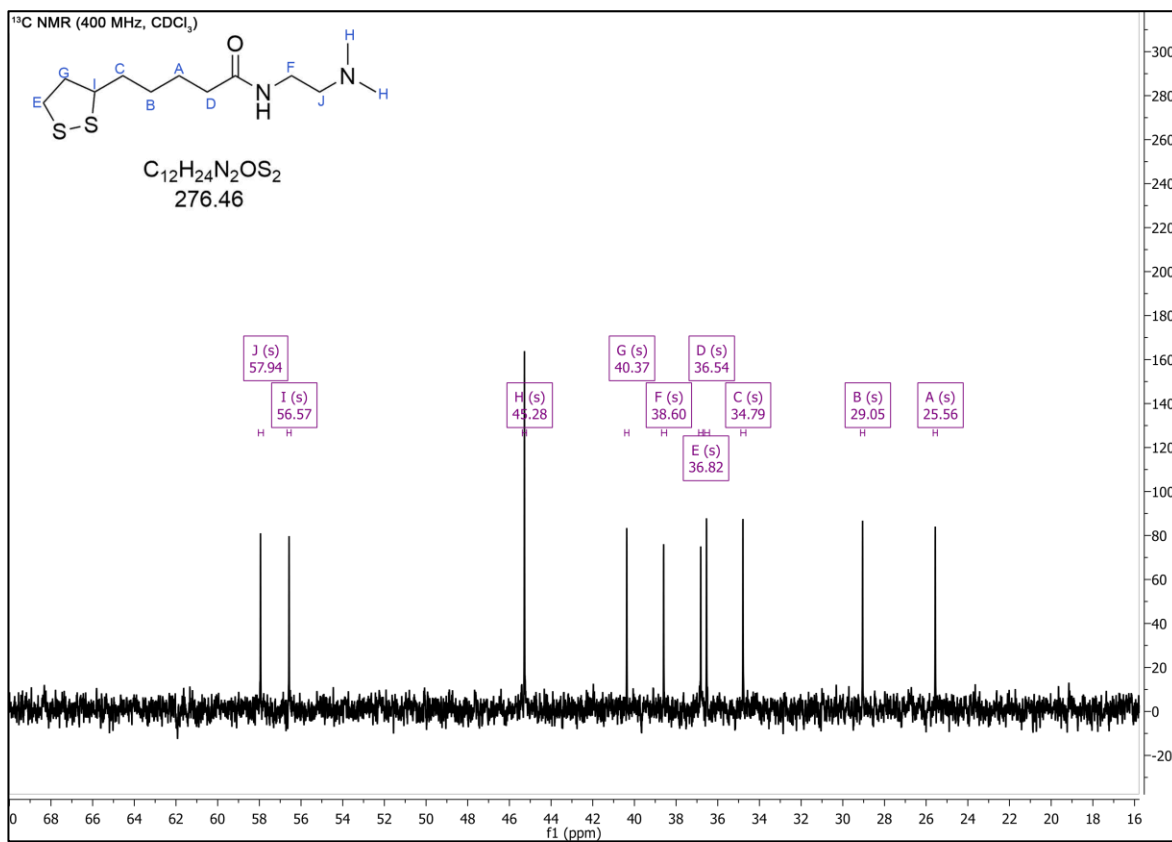


Figure A6. <sup>13</sup>C NMR spectrum of 2.

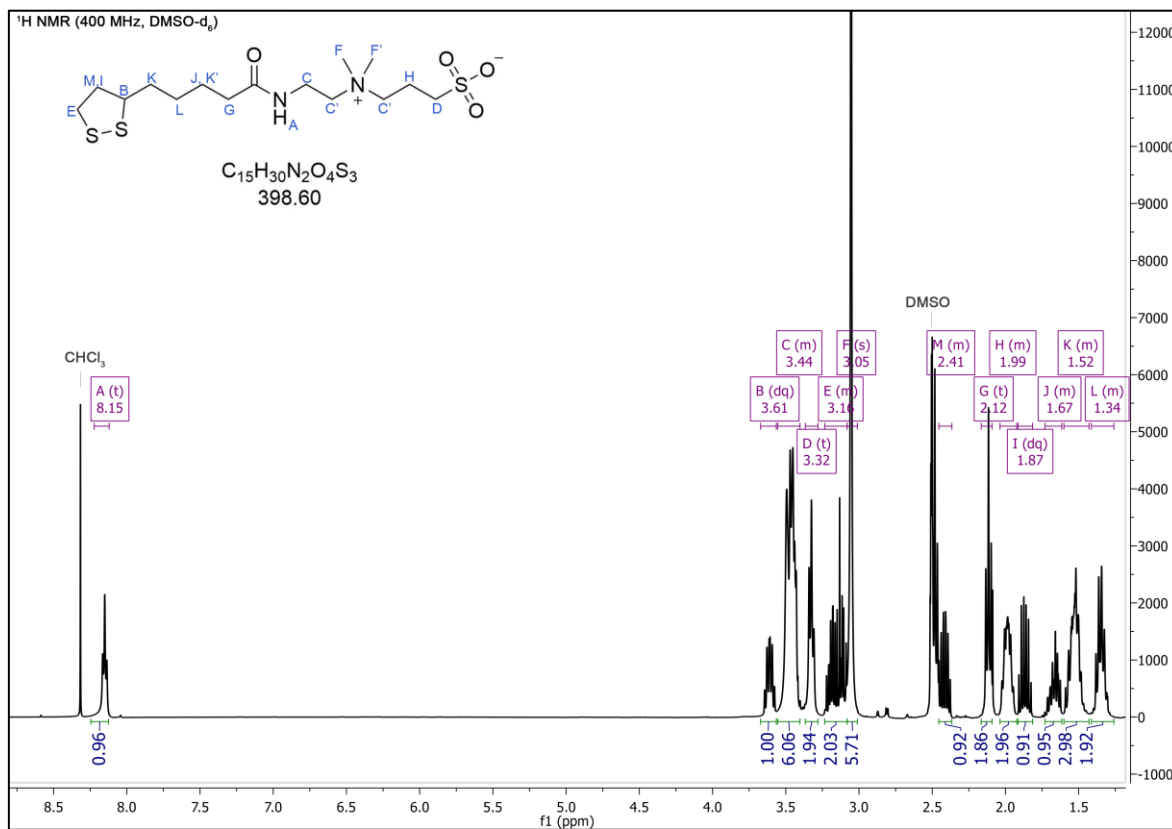
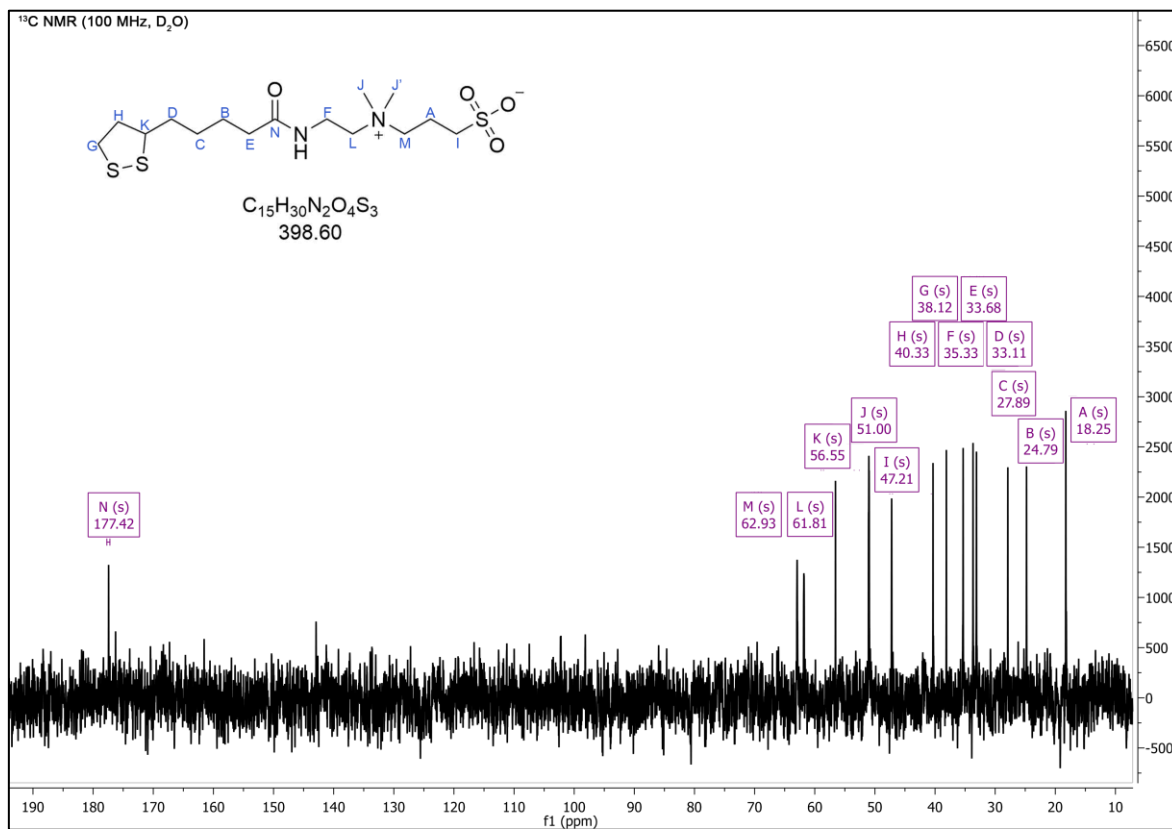


Figure A7. <sup>1</sup>H NMR spectrum of SB.



**Figure A8.** <sup>13</sup>C NMR spectrum of SB.

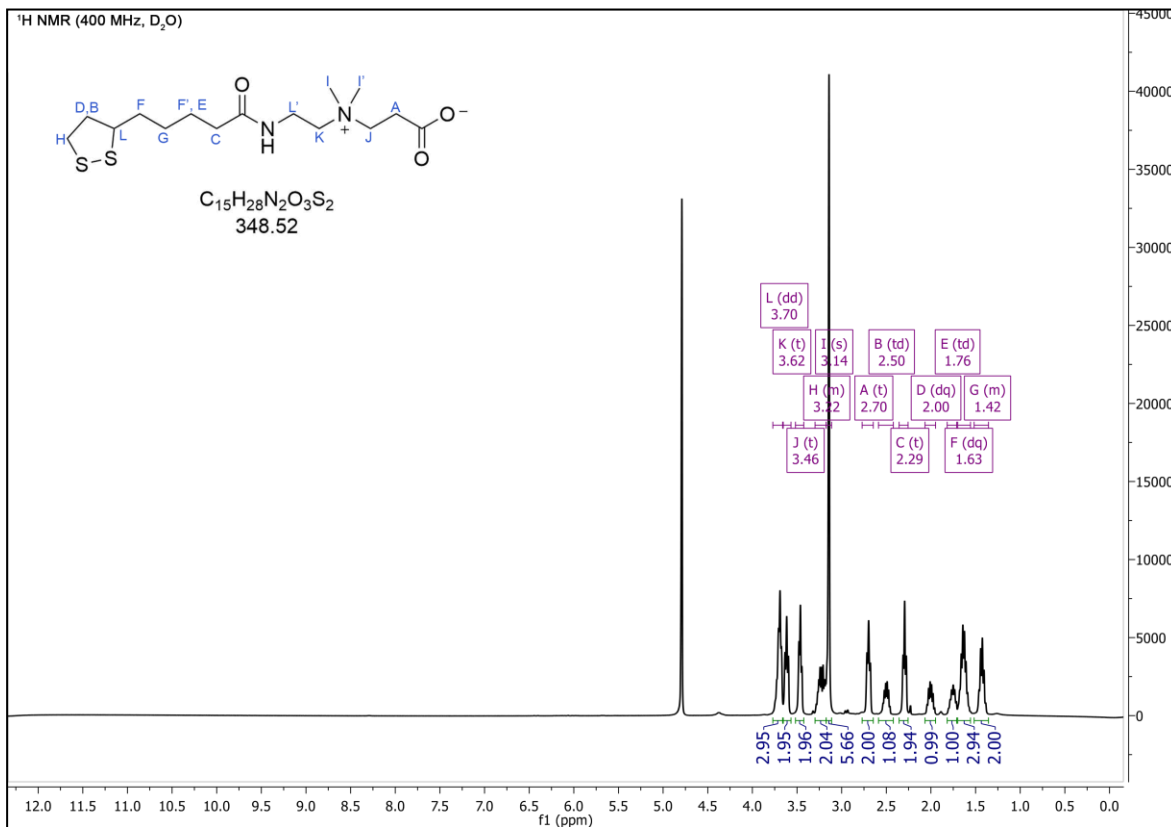


Figure A9. <sup>1</sup>H NMR spectrum of 4.

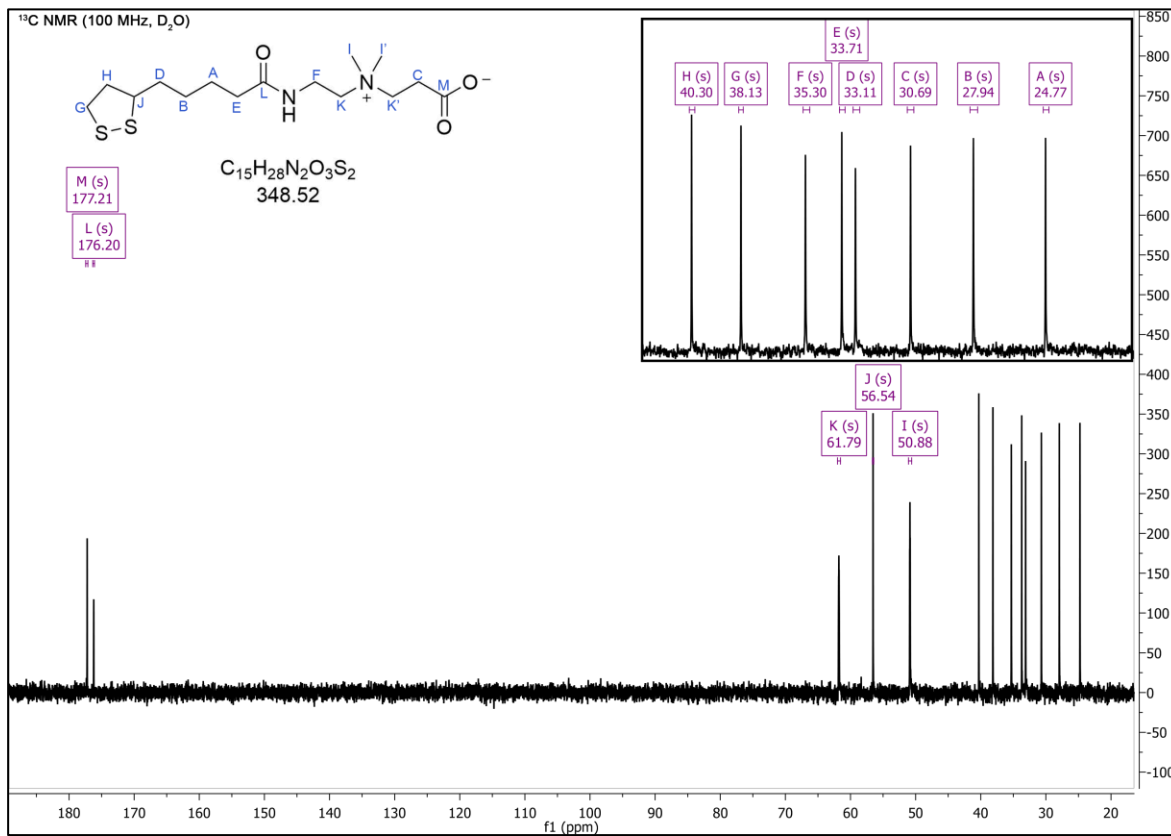


Figure A10. <sup>13</sup>C NMR spectrum of 4.

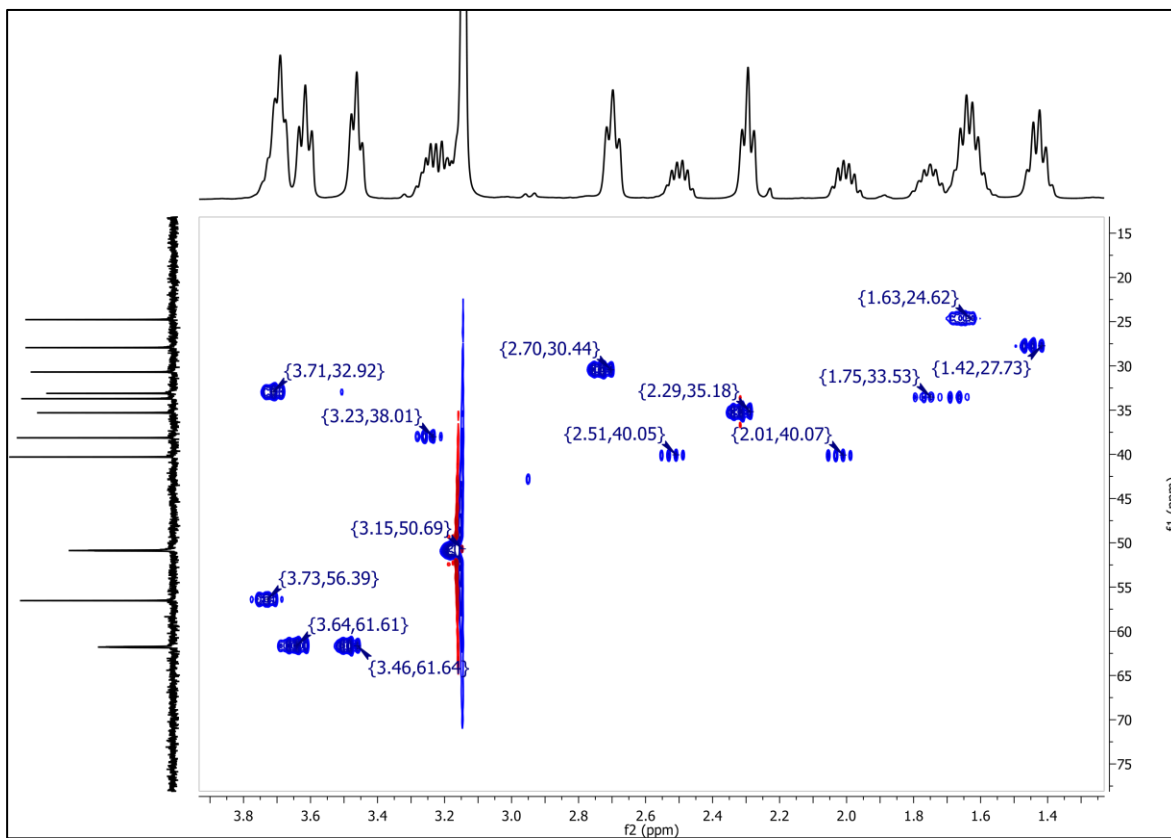


Figure A 11. HSQC spectrum of 4 in D<sub>2</sub>O.

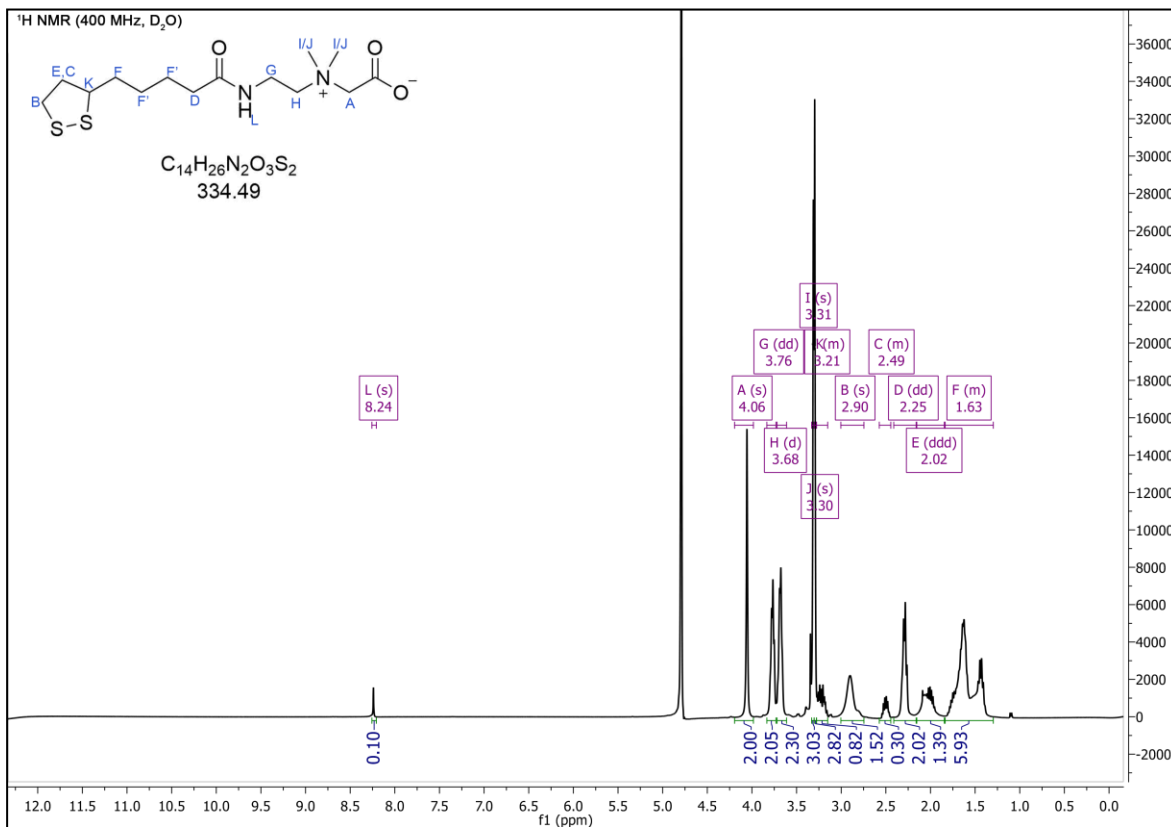


Figure A12. <sup>1</sup>H NMR spectrum of CB.

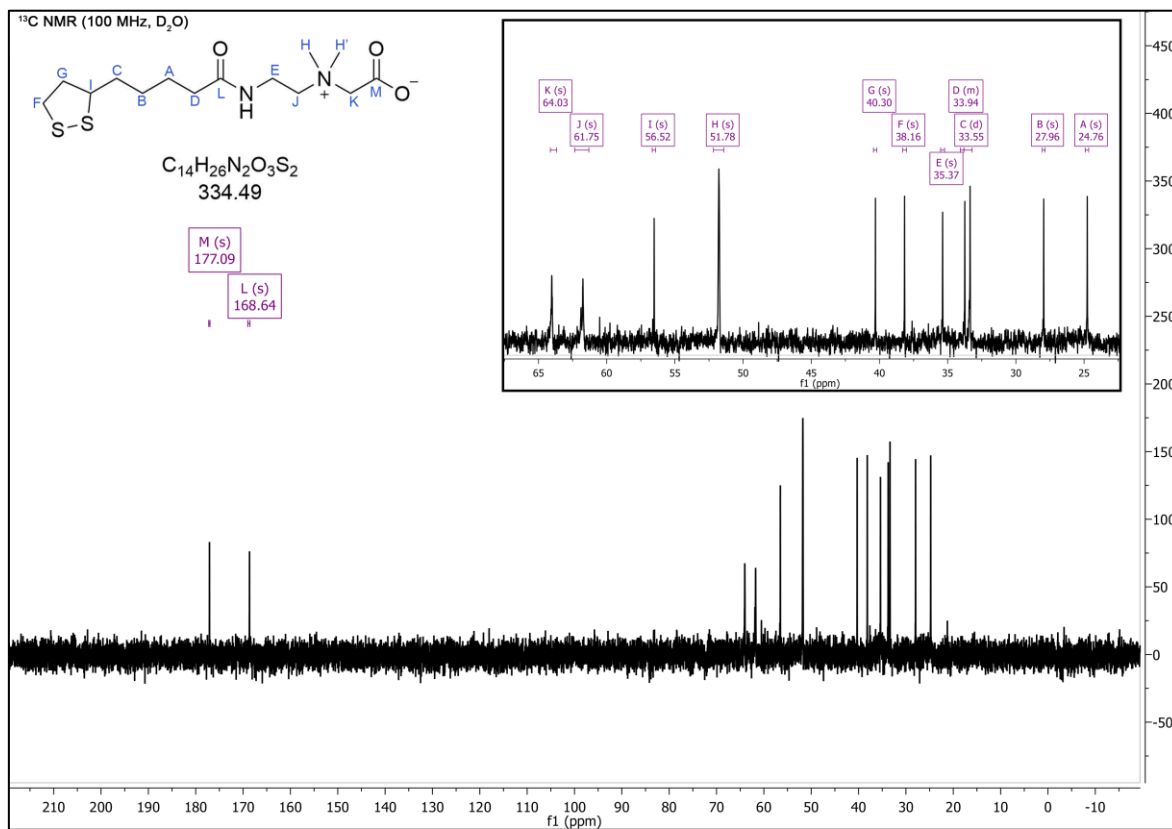


Figure A13. <sup>13</sup>C NMR spectrum of CB.

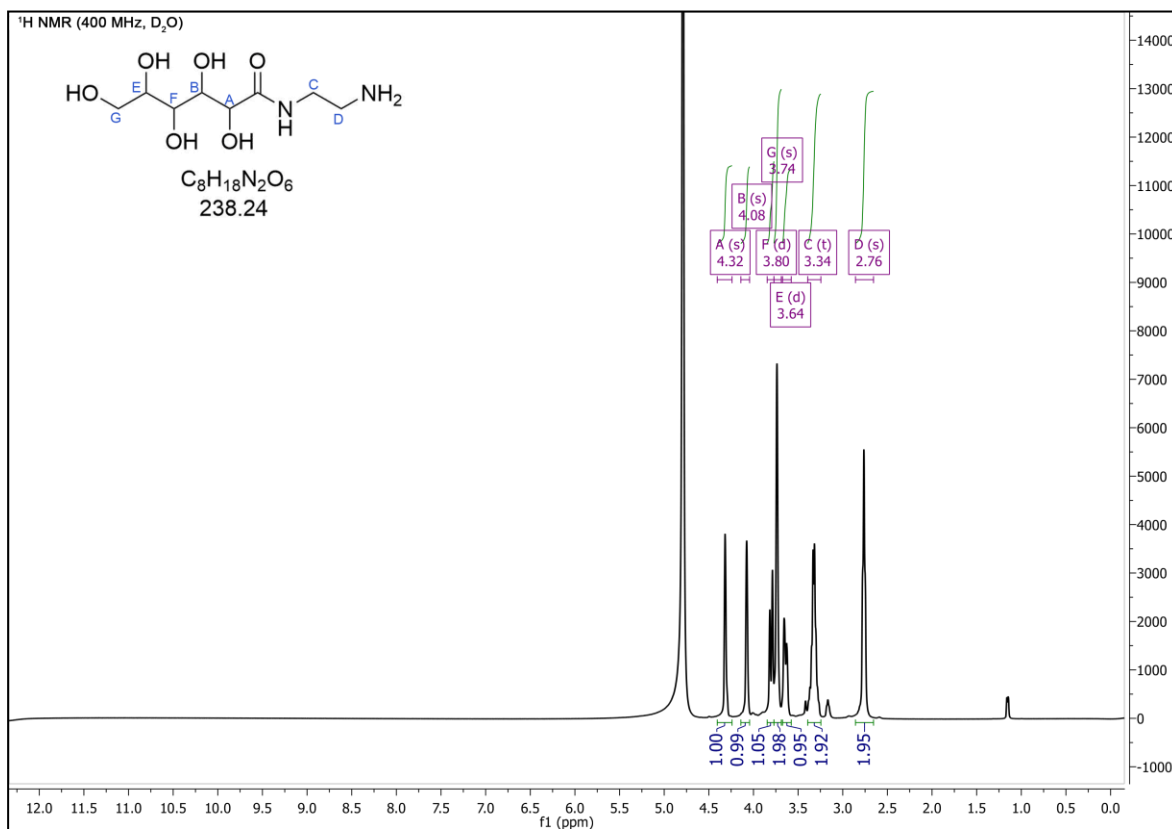


Figure A14. <sup>1</sup>H NMR spectrum of 6.

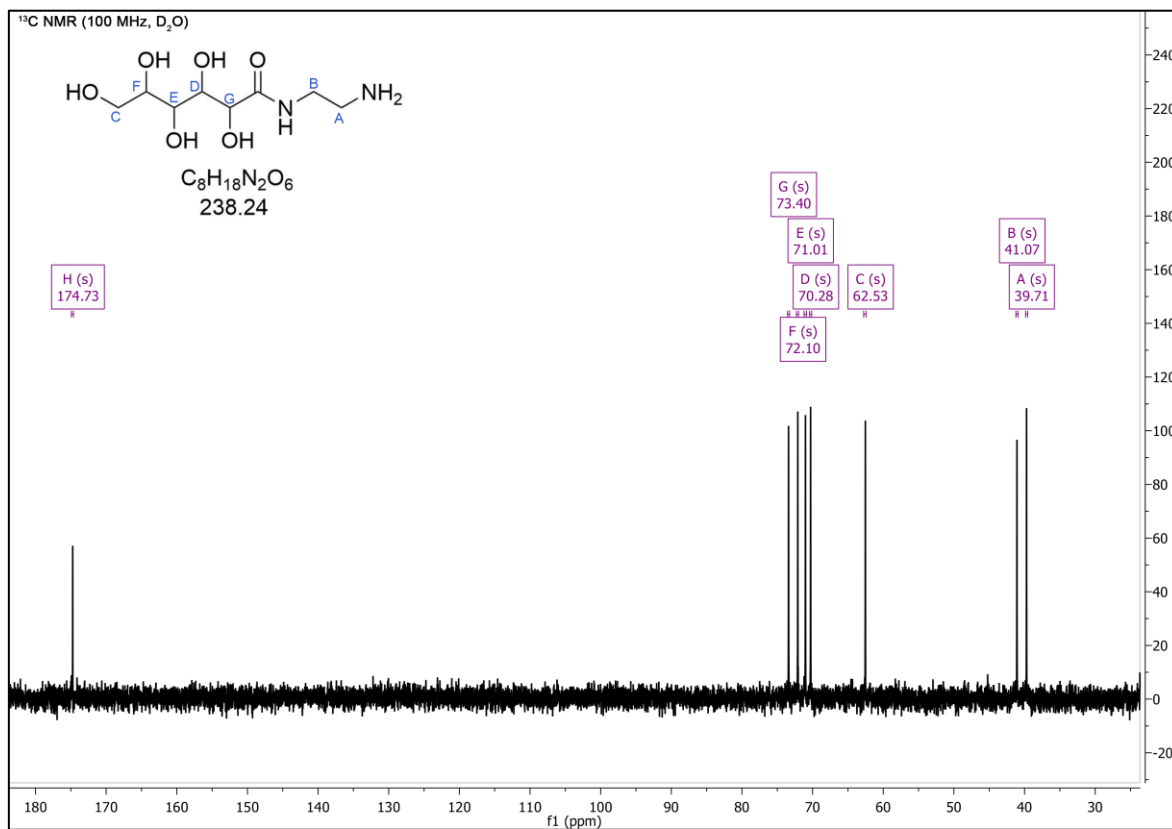


Figure A15. <sup>13</sup>C NMR spectrum of 6.

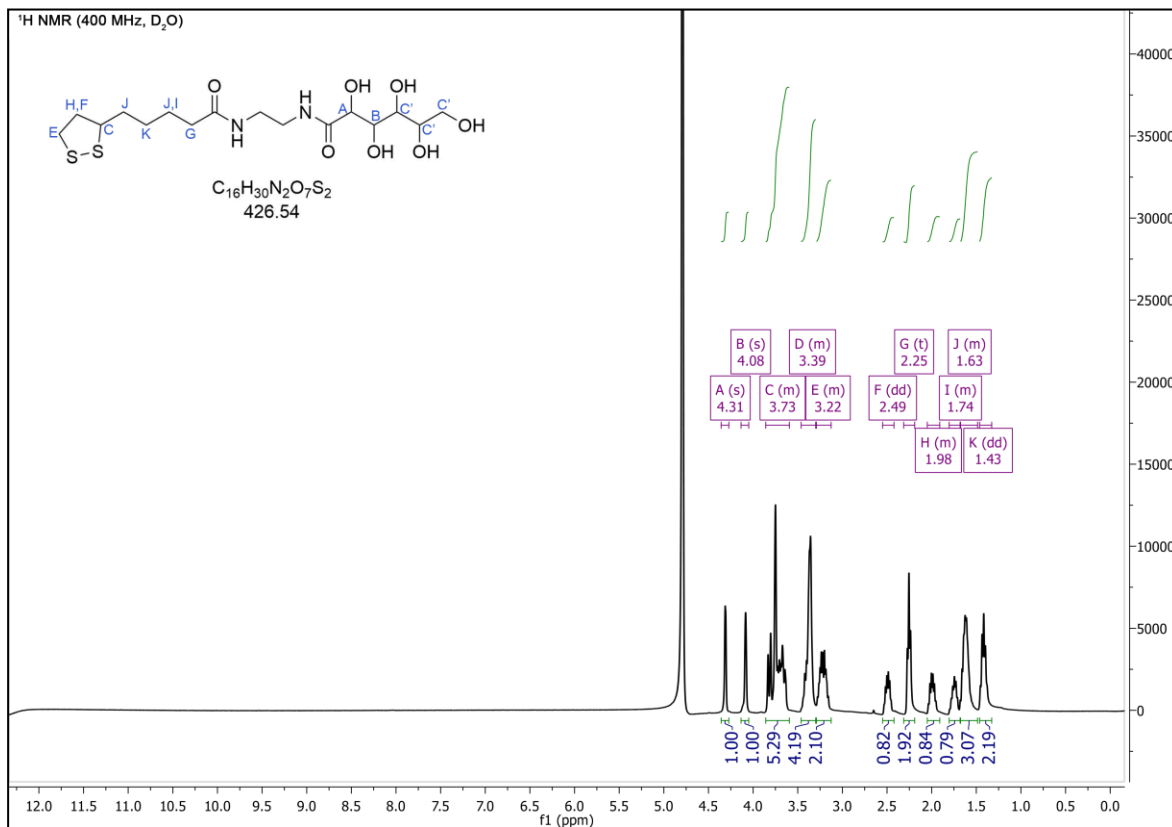


Figure A16. <sup>1</sup>H NMR spectrum of Glc.

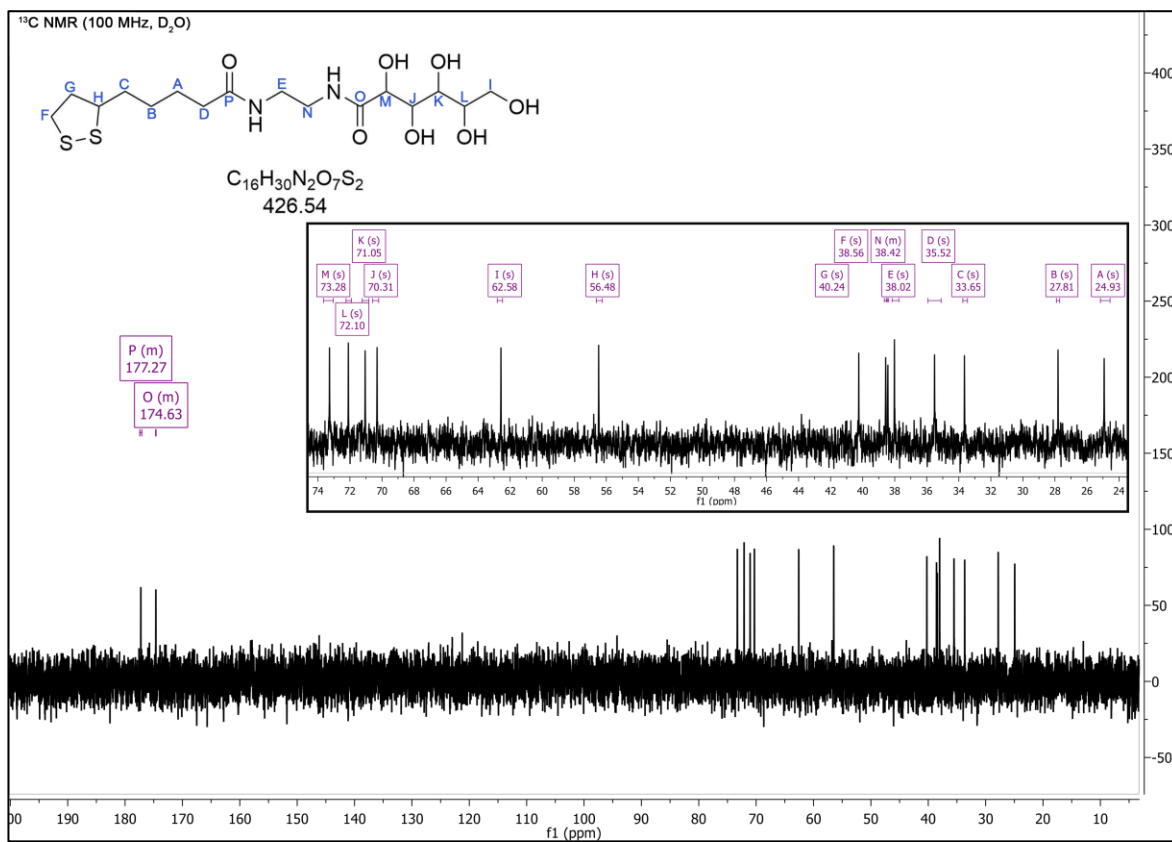


Figure A 17. <sup>13</sup>C NMR spectrum of Glc.

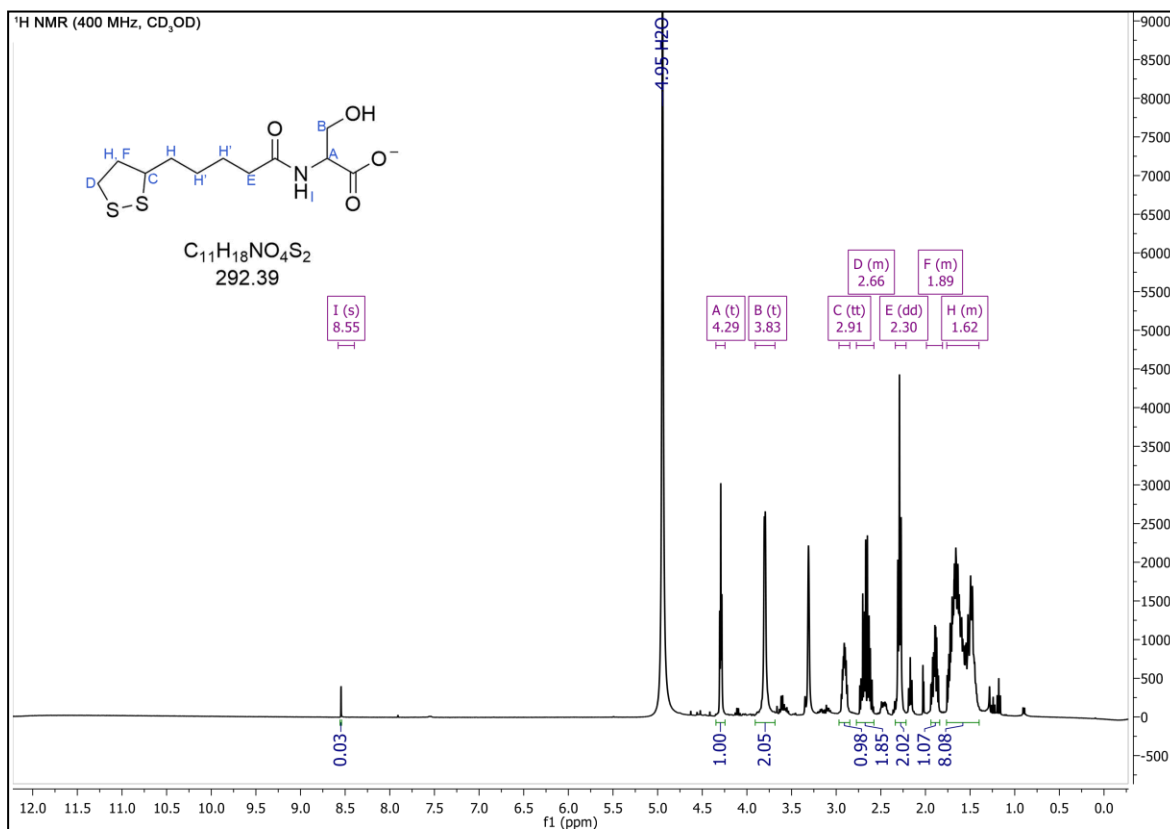
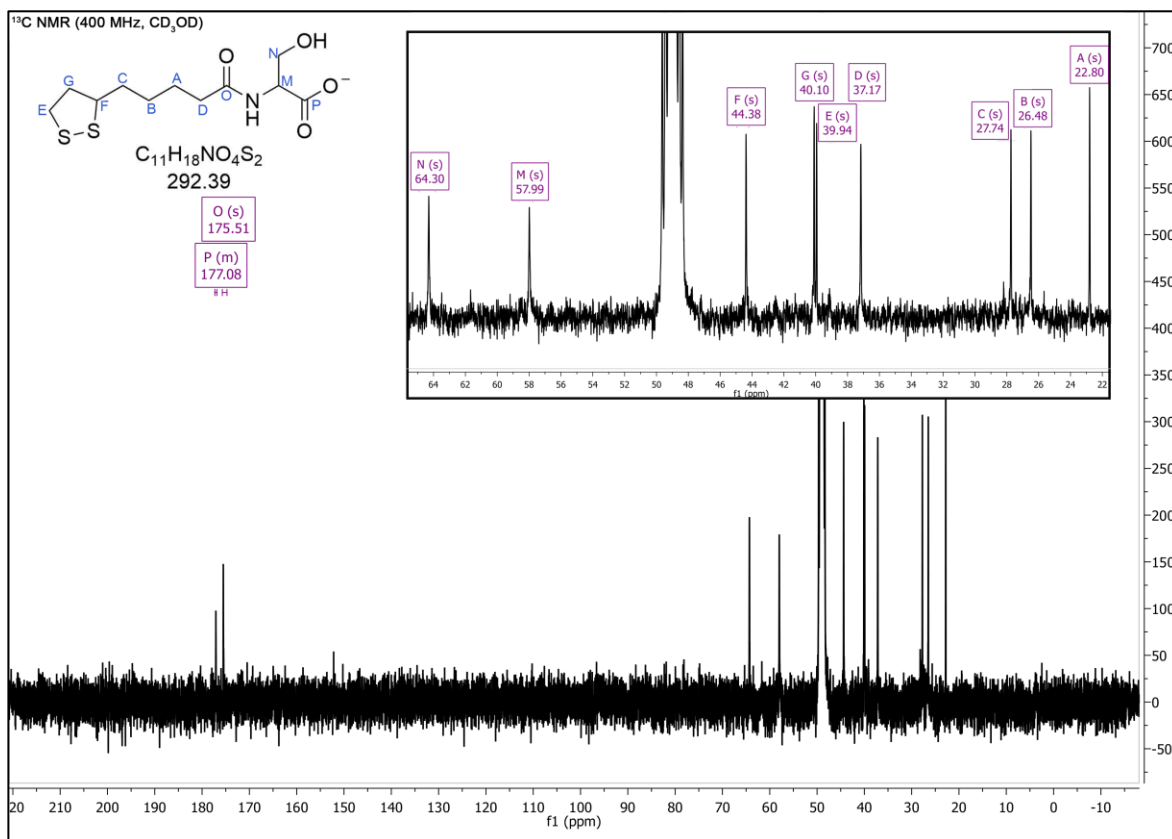


Figure A18. <sup>1</sup>H NMR spectrum of Ser.



**Figure A19.** <sup>13</sup>C NMR spectrum of Ser.

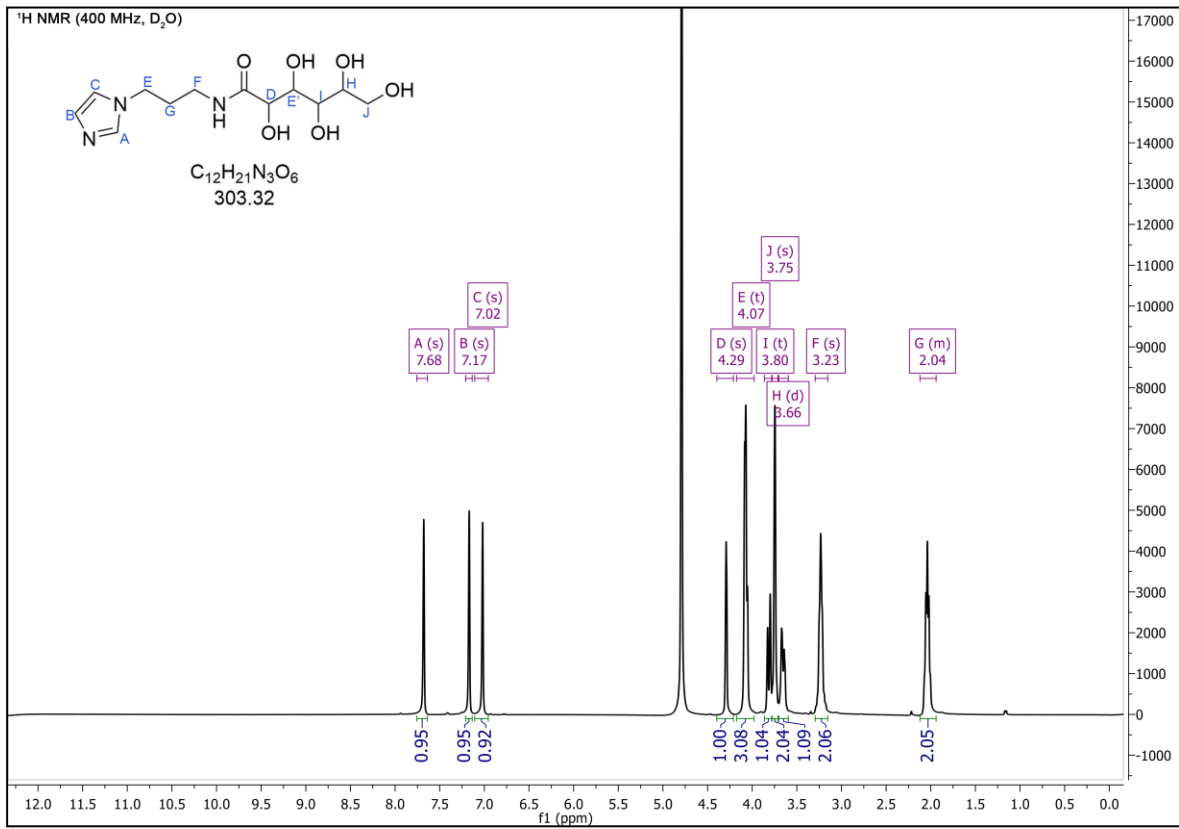


Figure A 20. <sup>1</sup>H NMR spectrum of API-Glc.

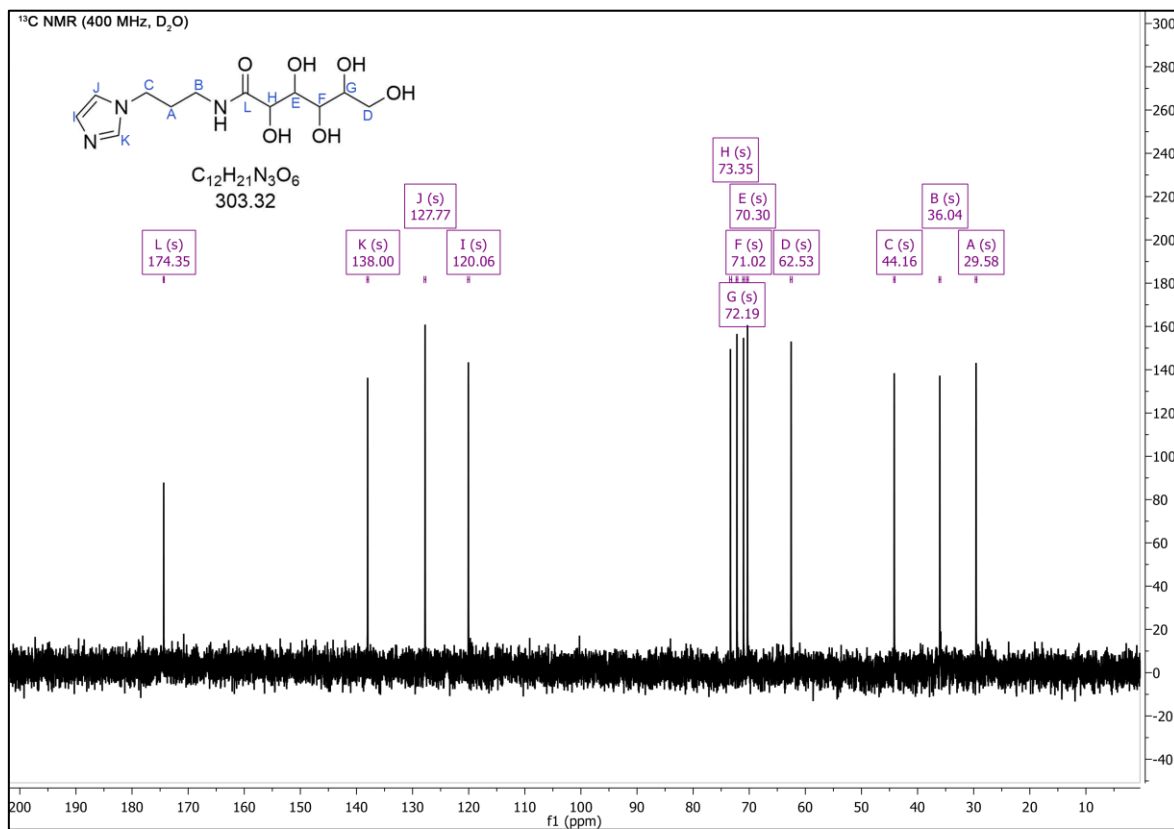


Figure A21. <sup>13</sup>C NMR spectrum of API-Glc.

## 2. ESI-MS Spectra

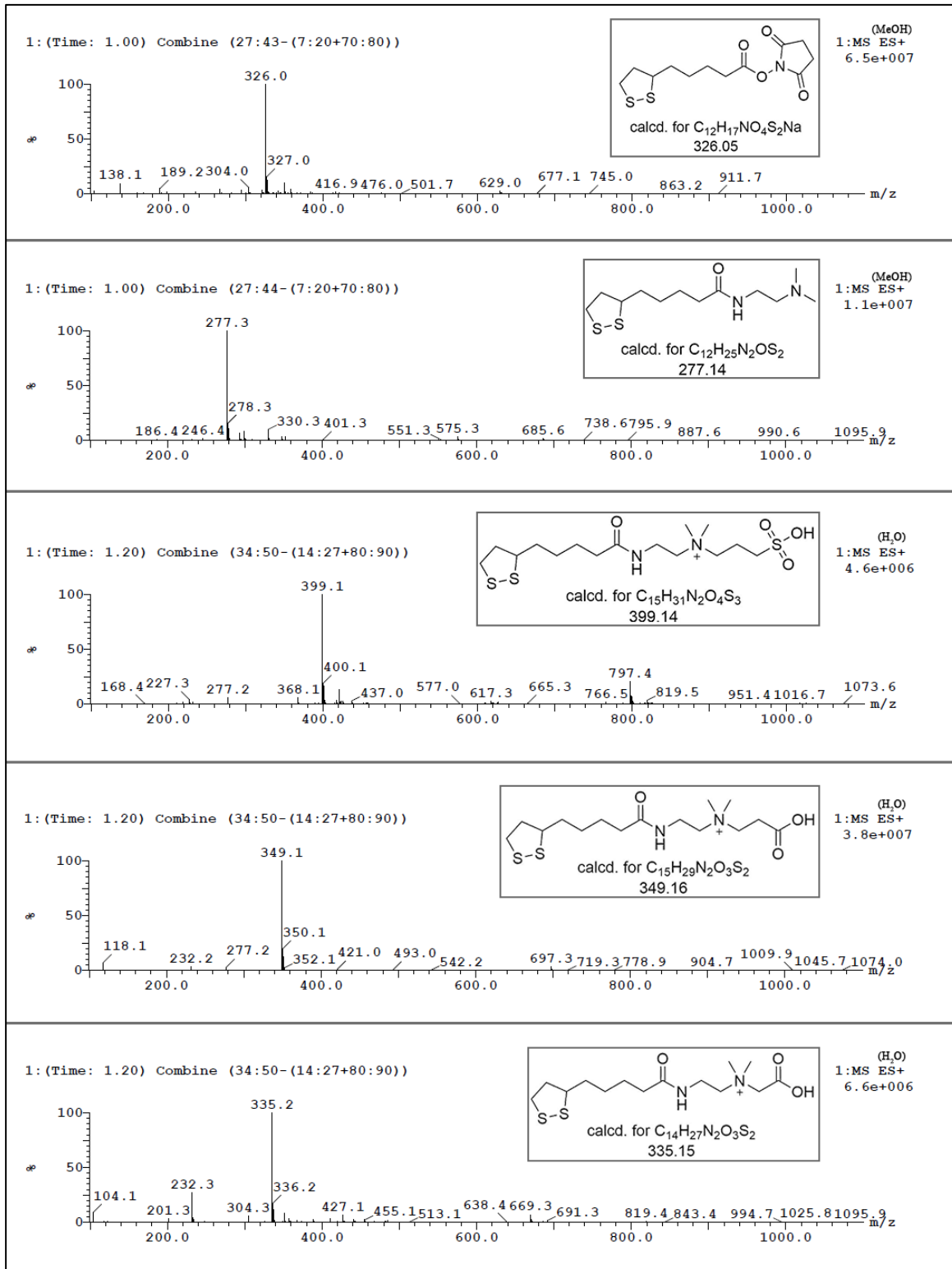


Figure A22. ESI-MS spectra of LA-NHS, 2, SB, 4, and CB.

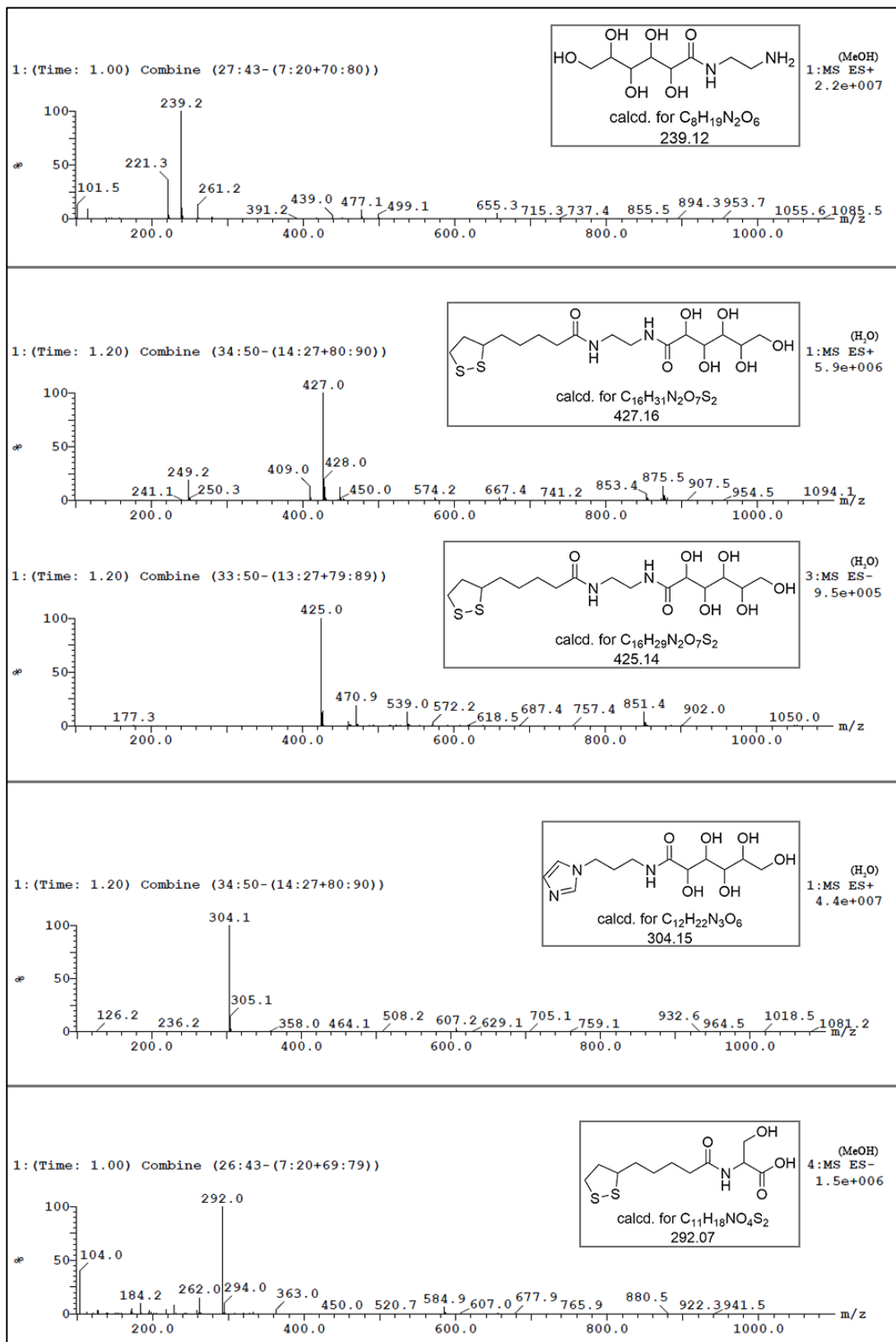
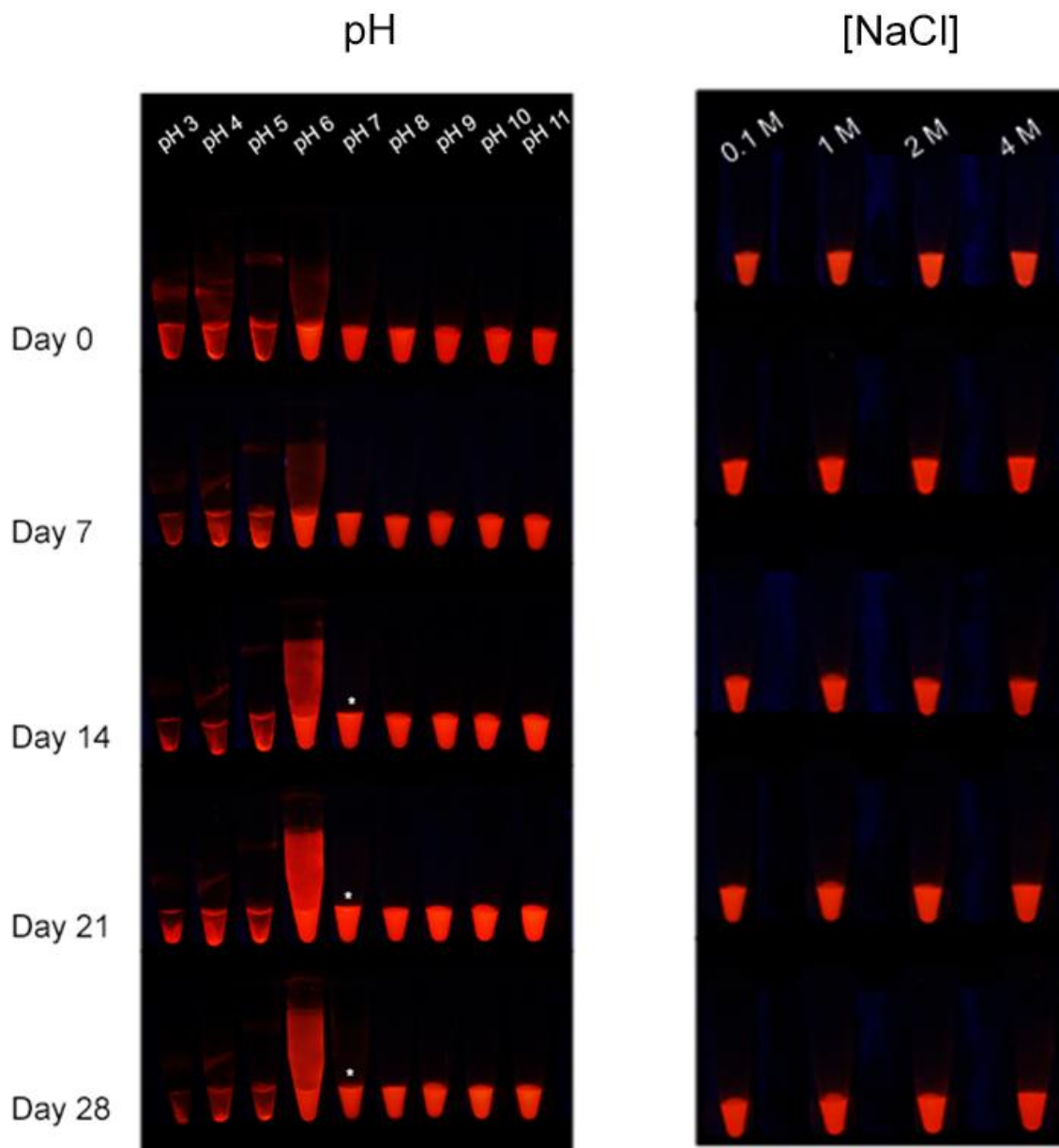
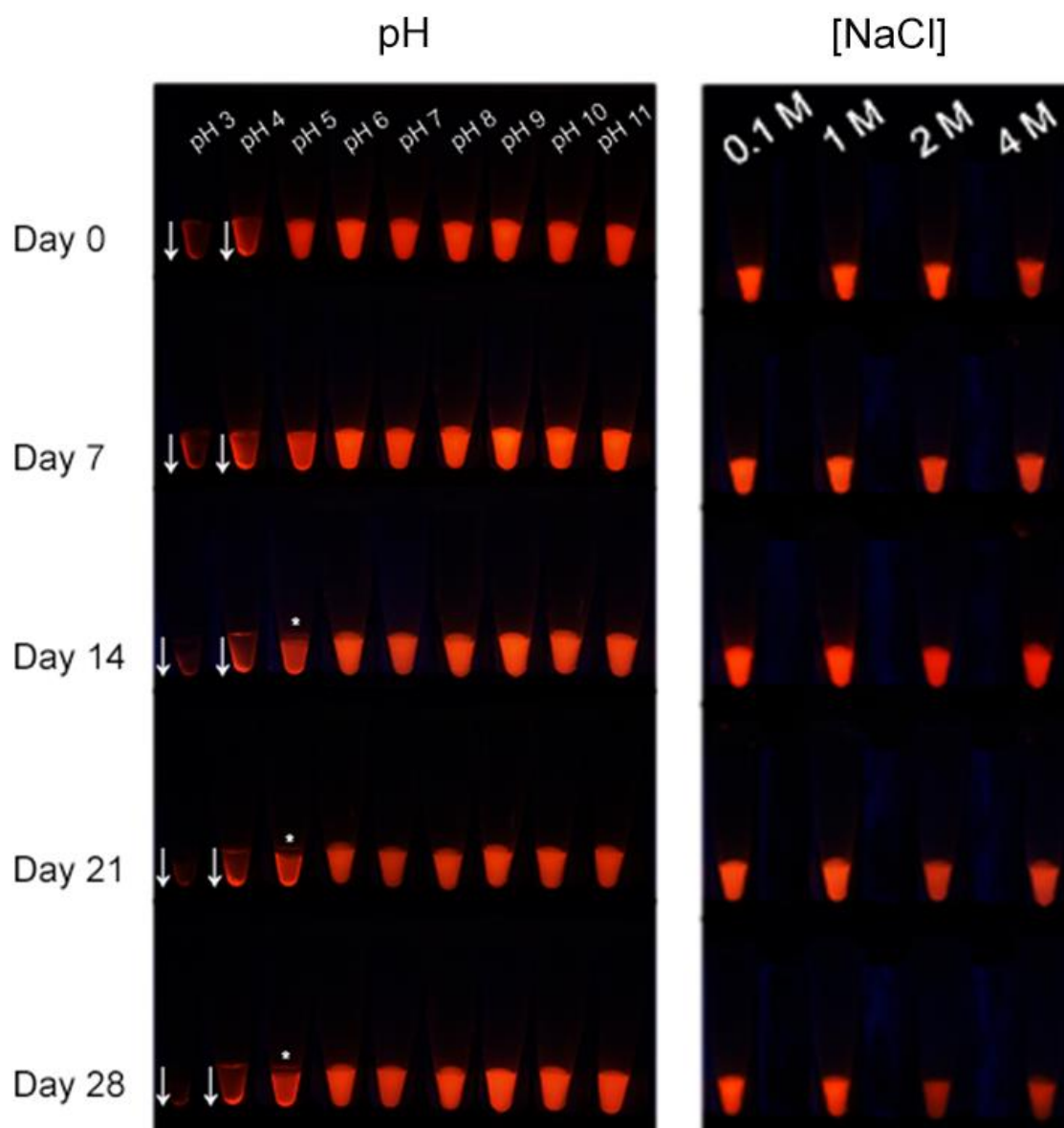


Figure A 23. ESI-MS spectra of 6, Glc, API-Glc, and Ser.

### 3. Stability Tests (pH and Ionic Strength)



**Figure A24.** Images of pH and ionic strength stability tests for QD<sub>DHLA</sub>.



**Figure A25.** Images of pH and ionic strength stability tests for QD<sub>GSH</sub>.

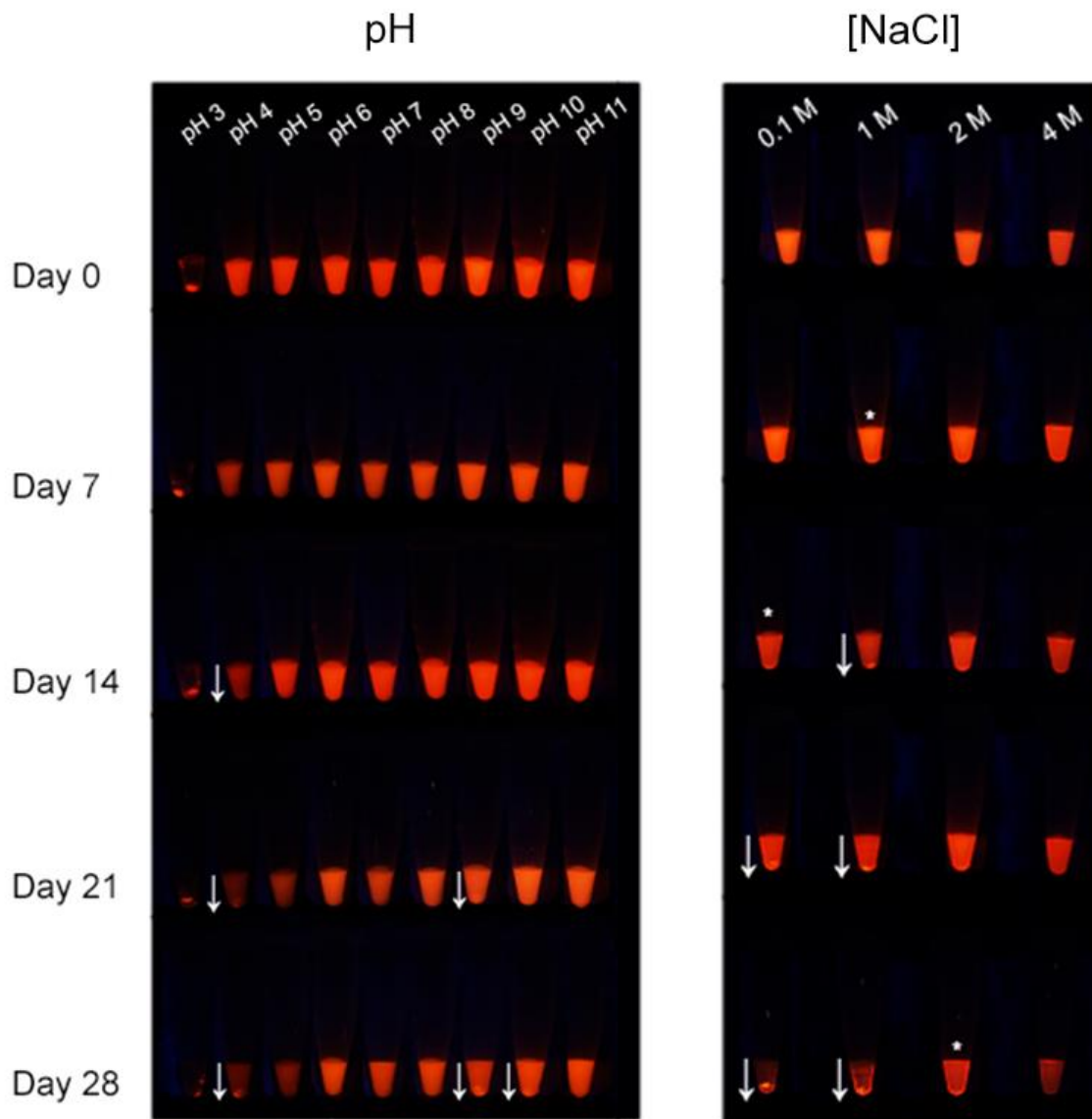


**Figure A26.** Images of pH and ionic strength stability tests for QD<sub>SB</sub>.

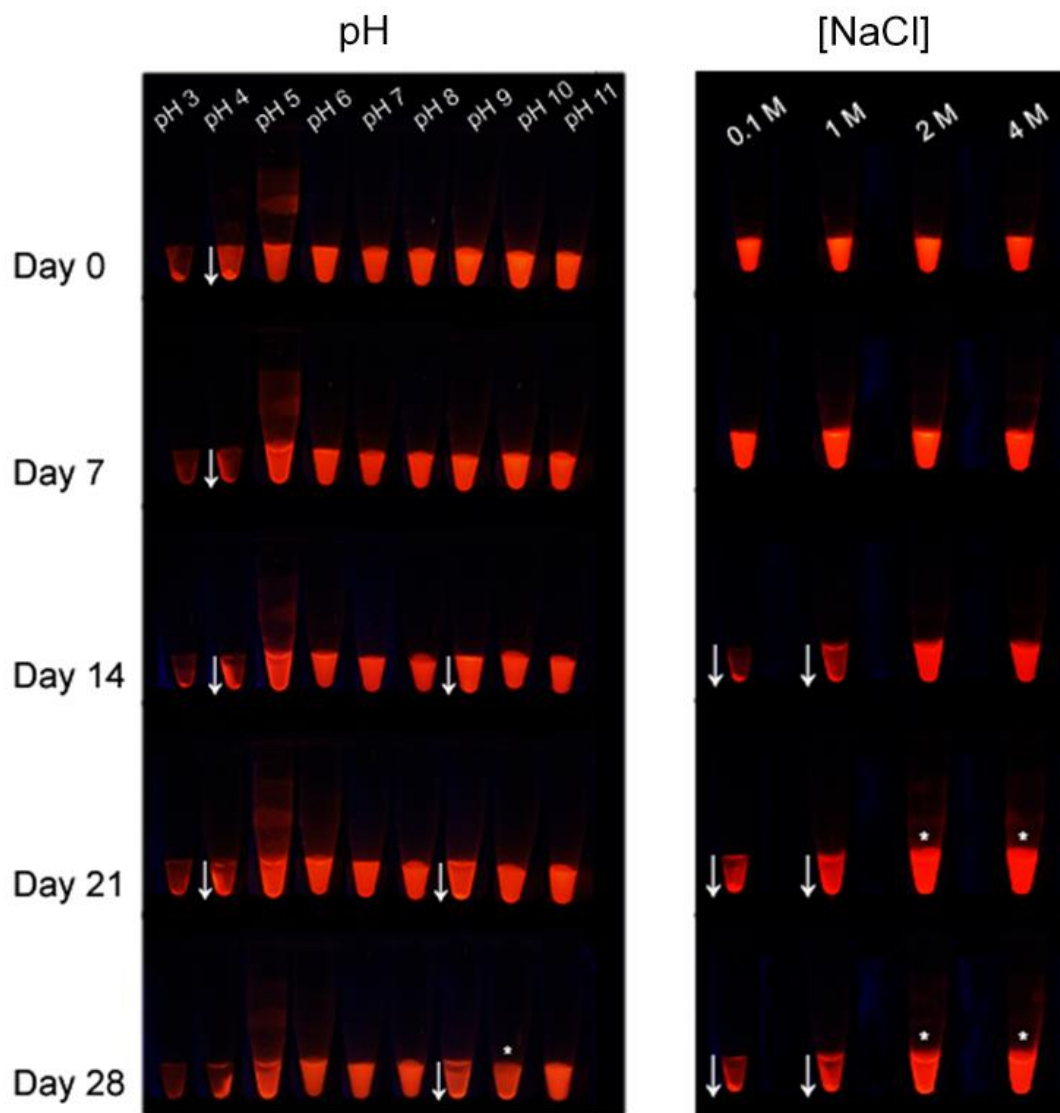


**Figure A27.** Images of pH and ionic strength stability tests for QDCB.

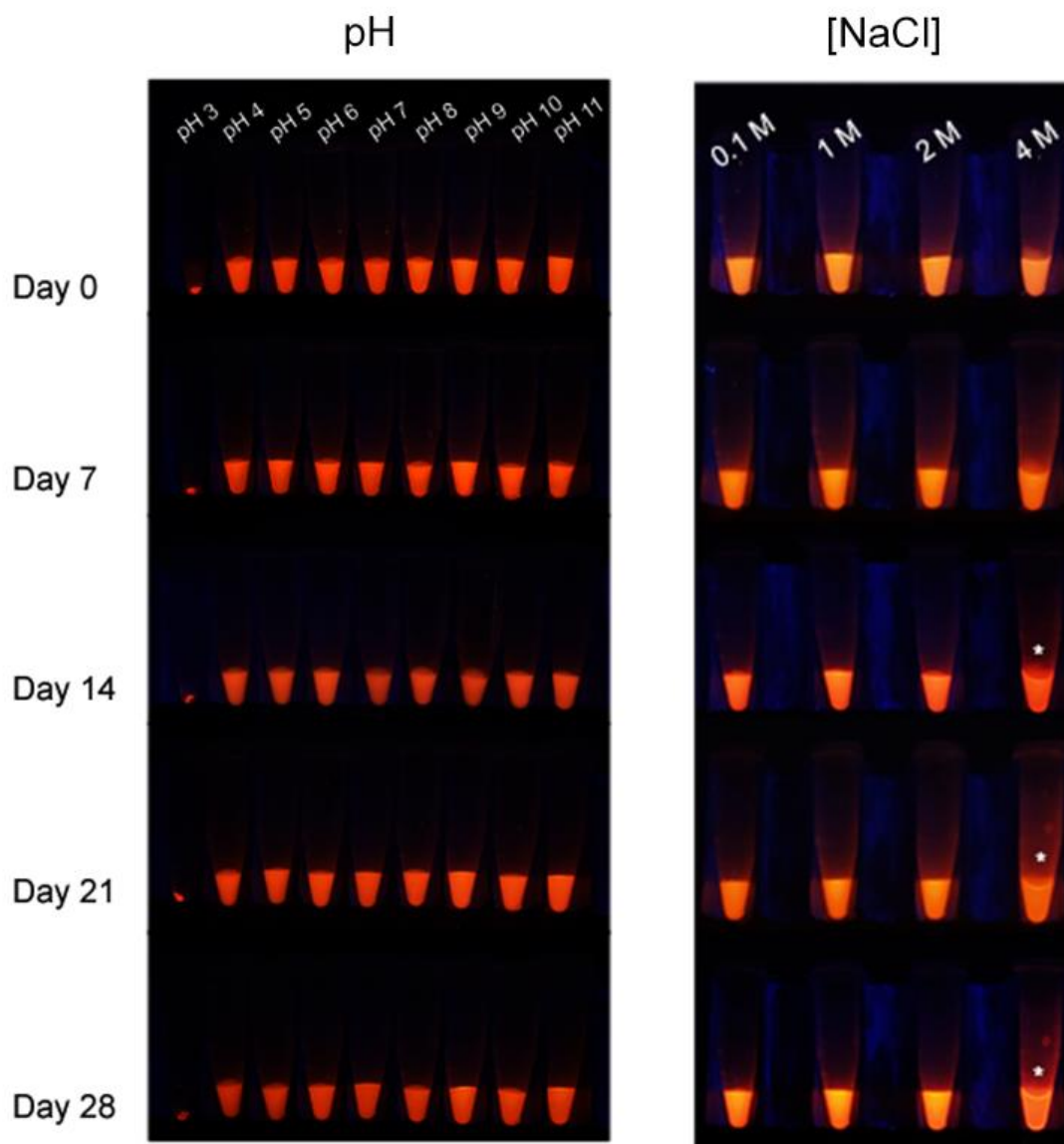


**Figure A28.** Images of pH and ionic strength stability tests for QD<sub>Glc</sub>.

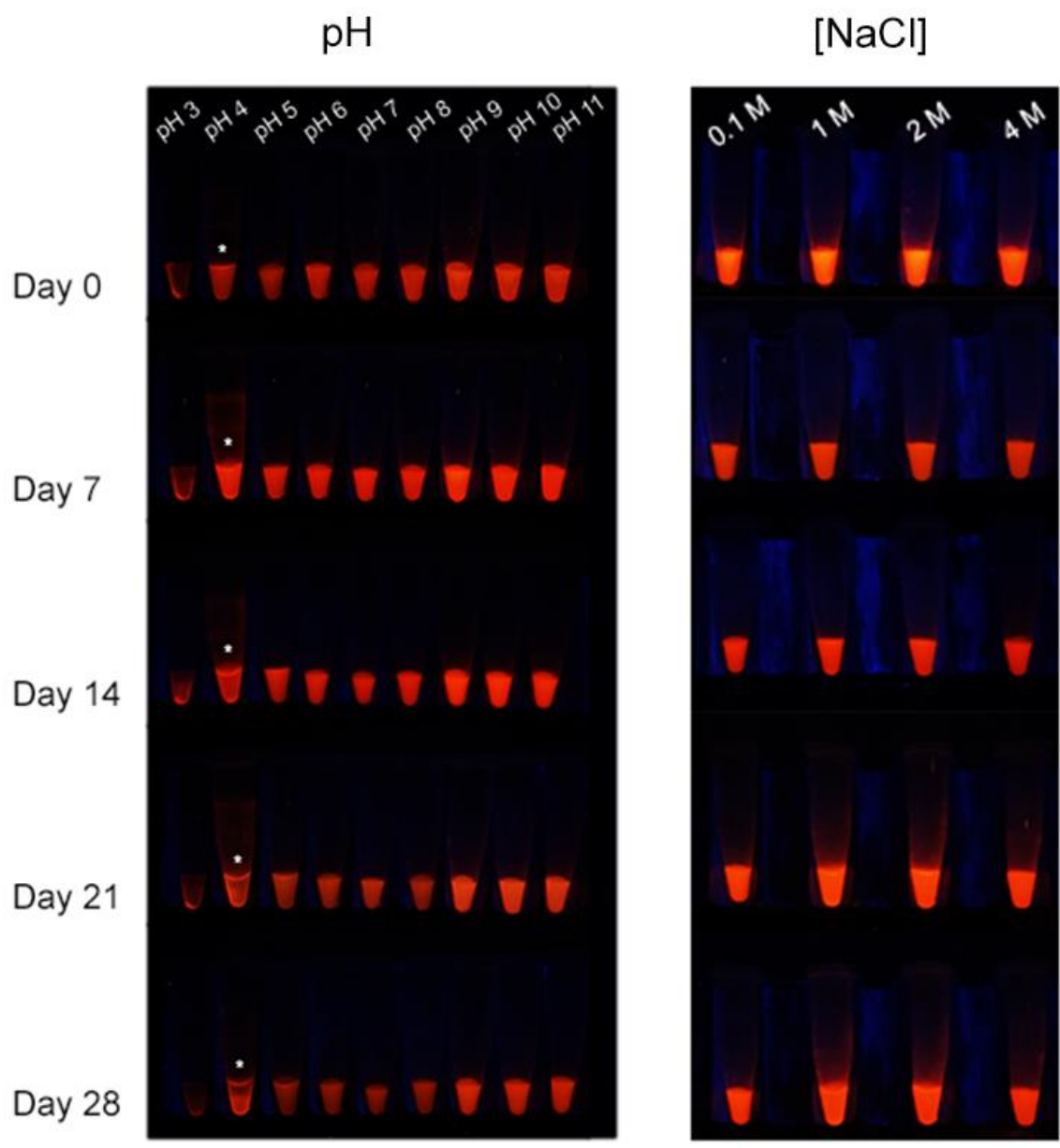


**Figure A29.** Images of pH and ionic strength stability tests for QD<sub>Ser</sub>.

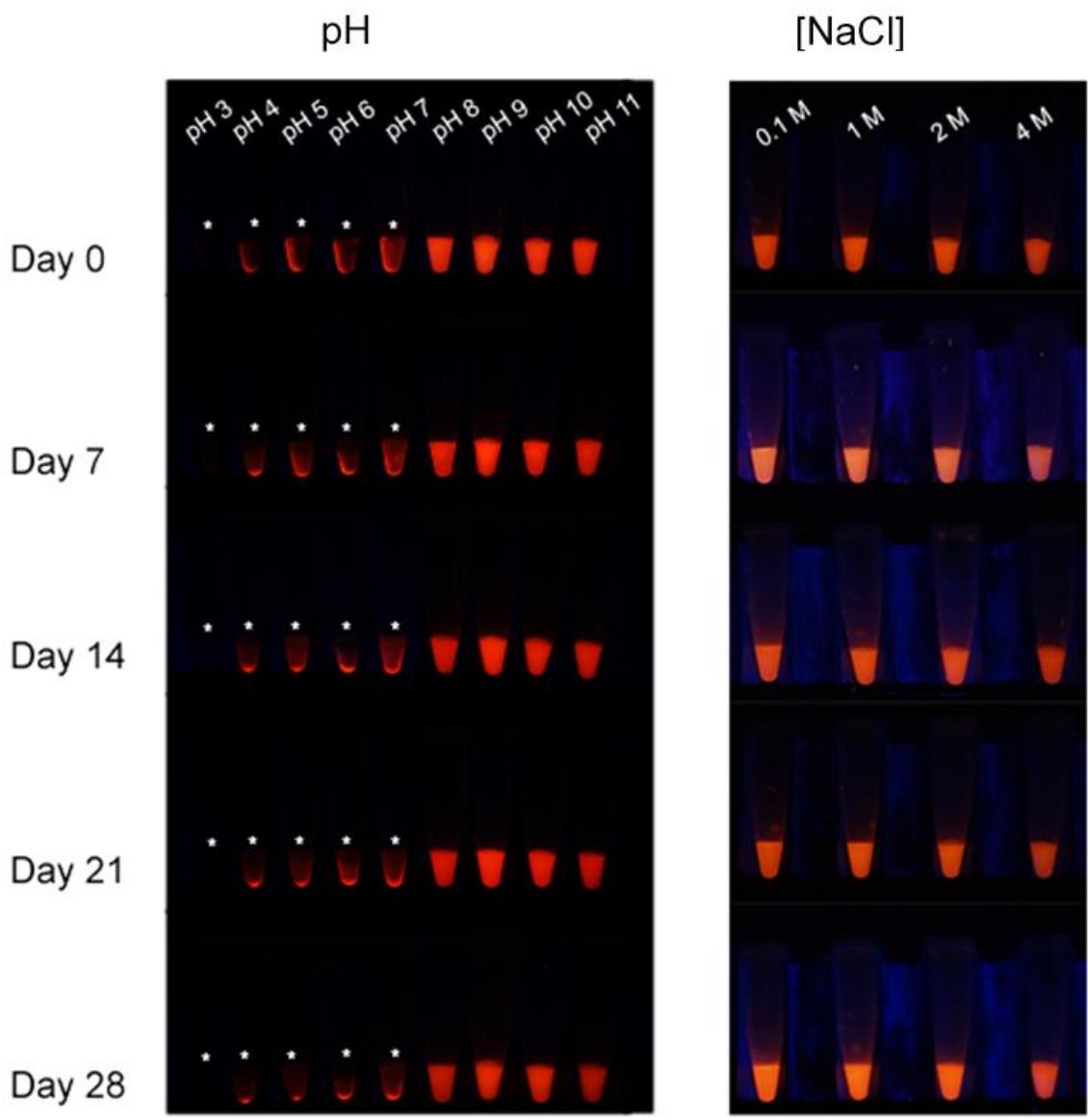


**Figure A30.** Images of pH and ionic strength stability tests for QD<sub>API</sub>-Glc.

## 4. Enzyme Assay Progress Curves

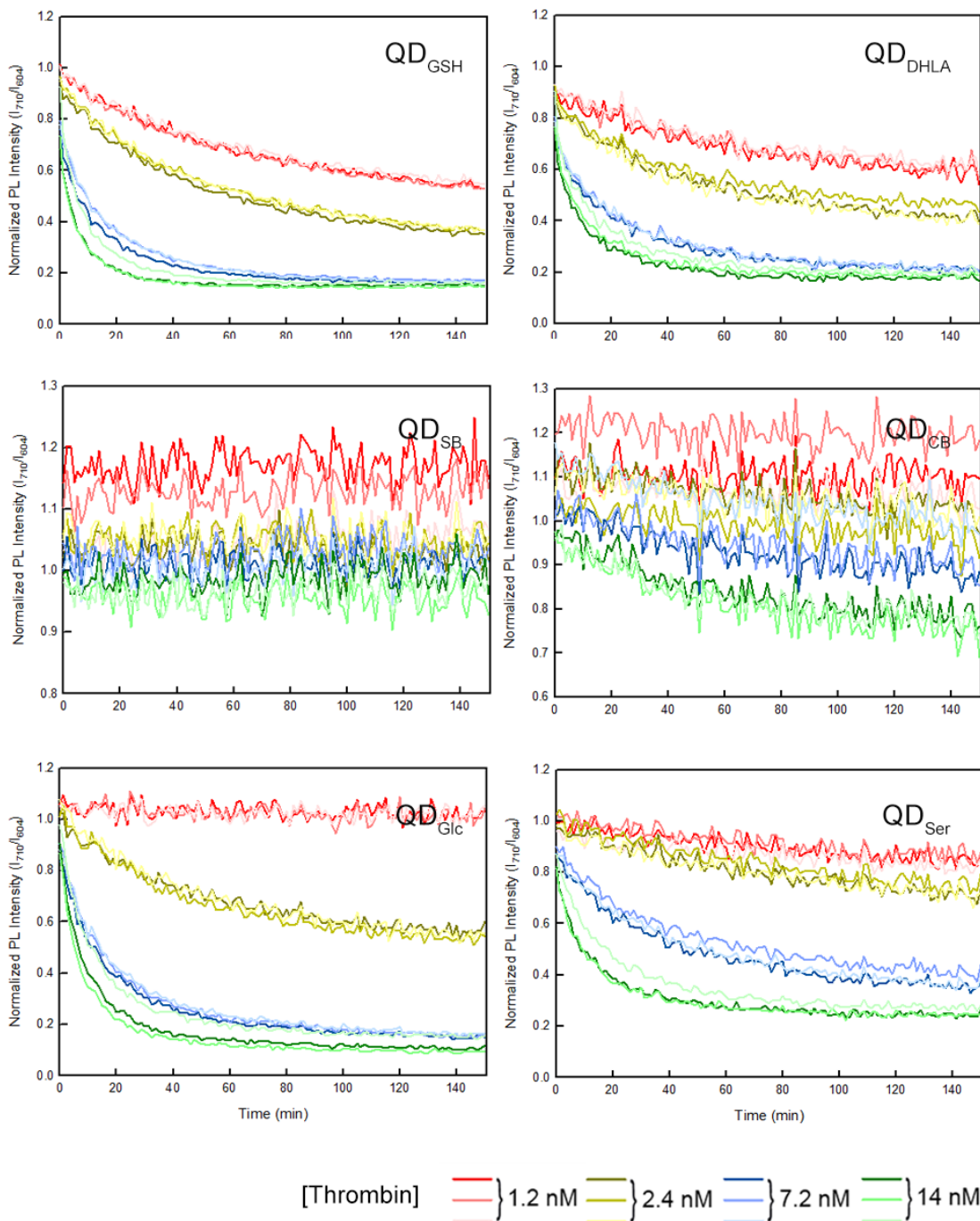


**Figure A31.** Progress curves of QD<sub>X</sub>-Sub(A680)<sub>8</sub> with various concentrations of thrombin.

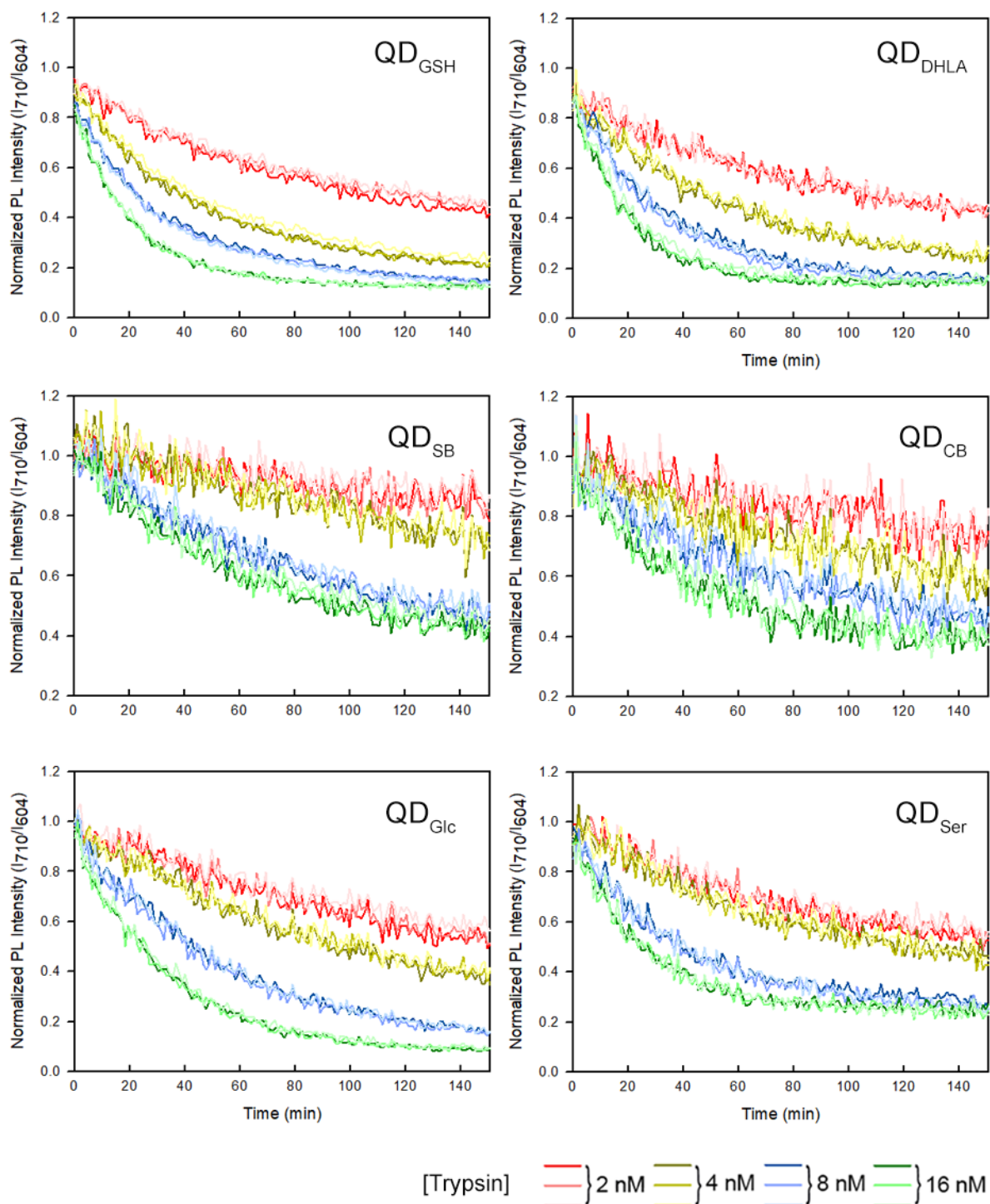


**Figure A32.** Progress curves of QD<sub>X</sub>-Sub(A680)<sub>8</sub> with various concentrations of trypsin.

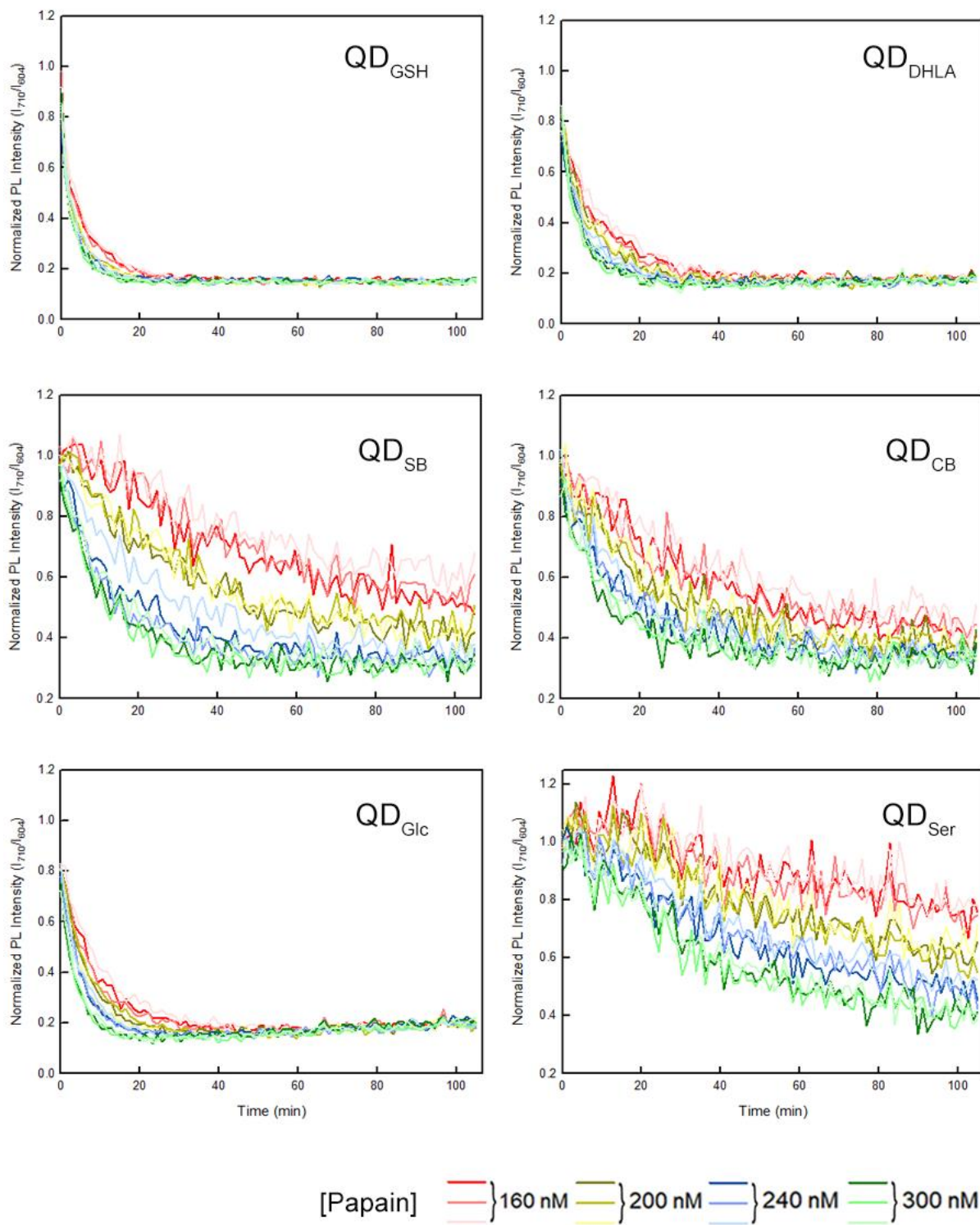


**Figure A33.** Progress curves of QD<sub>x</sub>-Sub(A680)<sub>8</sub> with various concentrations of papain.

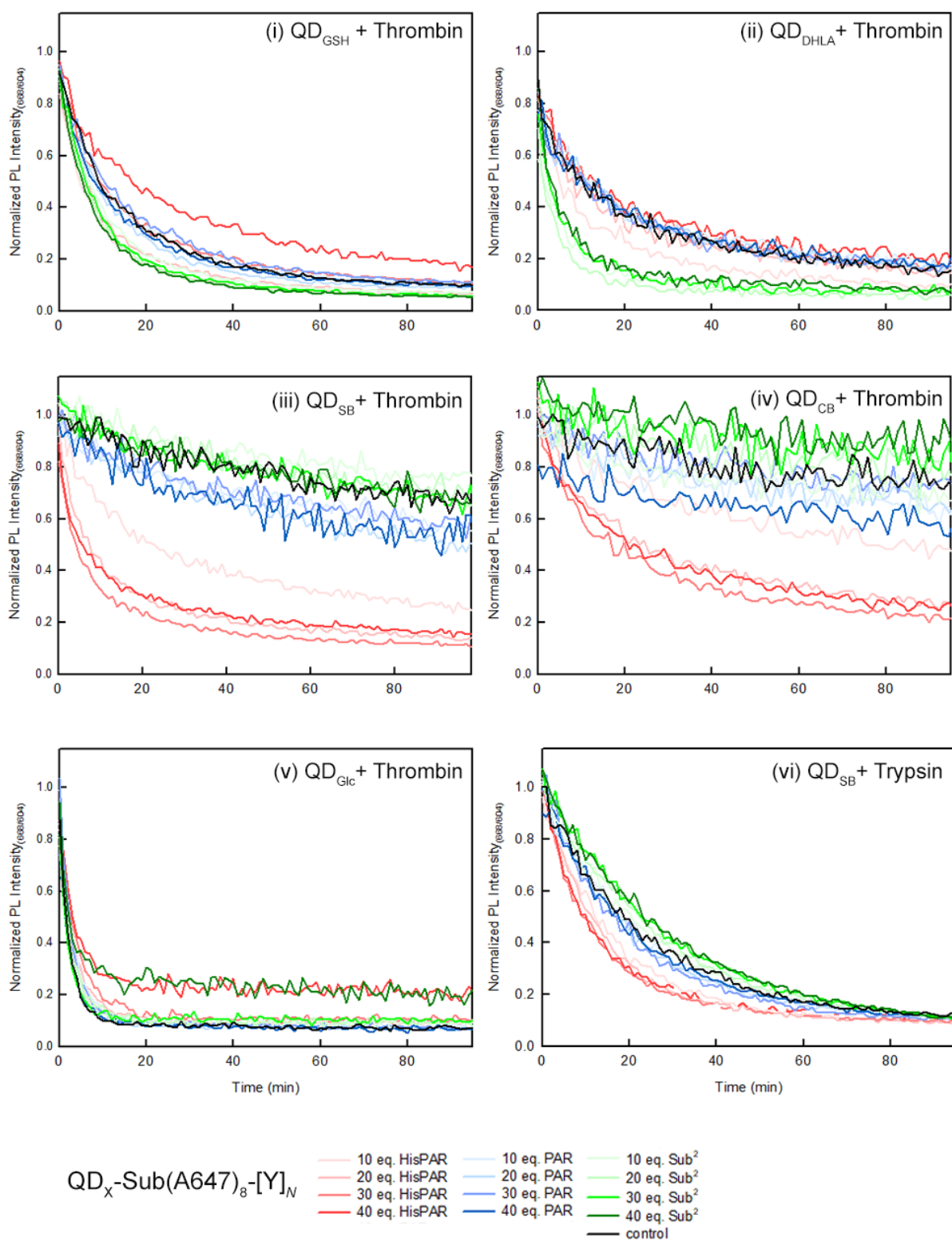


**Figure A34.** Progress curves of  $QD_X\text{-Sub(A647)}_8\text{-[Y]}_N$  with thrombin (i–v) and trypsin (vi).  $Y$  = HisPAR, PAR, or  $Sub^2$ , and  $n = 1\text{--}40$ .